UNIVERSITAT POLITÈCNICA DE CATALUNYA BARCELONATECH

Hybrid cell-centred/vertex model for multicellular systems

Payman Mosaffa

Universitat Politècnica de Catalunya

Laboratori de Càlcul Numèric

Doctor of Philosophy in Applied Mathematics

Hybrid Cell-centred/Vertex Model for Multicellular Systems

Author

Payman Mosaffa

Supervisor

Jose Javier Muñoz Romero

Barcelona, September 2017

UNIVERSITAT POLITÈCNICA DE CATALUNYA
BARCELONATECH
Escola de Doctorat

Acta de calificación de tesis doctoral

Curso académico:

Nombre y apellidos

Programa de doctorado

Unidad estructural responsable del programa

Resolución del Tribunal

Reunido el Tribunal designado a tal efecto, el doctorando / la doctoranda expone el tema de la su tesis doctoral titulada _____

_____.

Acabada la lectura y después de dar respuesta a las cuestiones formuladas por los miembros titulares del tribunal, éste otorga la calificación:

☐ NO APTO ☐ APROBADO ☐ NOTABLE ☐ SOBRESALIENTE

(Nombre, apellidos y firma)	(Nombre, apellidos y firma)	
Presidente/a	Secretario/a	
(Nombre, apellidos y firma)	(Nombre, apellidos y firma)	(Nombre, apellidos y firma)
Vocal	Vocal	Vocal

_____, _____ de _____ de _____

El resultado del escrutinio de los votos emitidos por los miembros titulares del tribunal, efectuado por la Escuela de Doctorado, a instancia de la Comisión de Doctorado de la UPC, otorga la MENCIÓN CUM LAUDE:

☐ SÍ ☐ NO

(Nombre, apellidos y firma)	(Nombre, apellidos y firma)
Presidente de la Comisión Permanente de la Escuela de Doctorado	Secretario de la Comisión Permanente de la Escuela de Doctorado

Barcelona a _____ de _____ de _____

Abstract

This thesis presents a hybrid vertex/cell-centred approach to mechanically simulate planar cellular monolayers undergoing cell reorganisation. Cell centres are represented by a triangular nodal network, while the cell boundaries are formed by an associated vertex network. The two networks are coupled through a kinematic constraint which we allow to relax progressively. Cell-cell connectivity changes due to cell reorganisation or remodelling events, are accentuated. These situations are handled by using a variable resting length and applying an Equilibrium-Preserving Mapping (EPM) on the new connectivity, which computes a new set of resting lengths that preserve nodal and vertex equilibrium. As a by-product, the proposed technique enables to recover fully vertex or fully cell-centred models in a seamless manner by modifying a numerical parameter of the model. The properties of the model are illustrated by simulating monolayers subjected to imposed extension and during a wound healing process. The evolution of forces and the EPM are analysed during the remodelling events.

Resumen

Esta tesis presenta un modelo híbrido para la simulación mecánica de monocapas celulares. Este modelo combina métodos de vértices y centrados en la célula, y está orientado al análisis de deformaciones con reorganización celular. Los núcleos vienen representados por nodos que forman una malla triangular, mientras que las contornos (membranas y córtex) forman una malla poligonal de vértices. Las dos mallas se acoplan a través de una restricción cinemática que puede ser relajada de forma controlada. El estudio hace especial hincapié en los cambios de conectividad, tanto debidos a la reorganización celular como el remodelado del citoesqueleto. Estas situaciones se abordan a través de una longitud de referencia variable y aplicando un Mapeo con Conservación de Equilibrio (EPM) que minimiza el error en el equilibrio nodal y en los vértices. La técnica resultante puede ser adaptada progresivamente a través de un parámetro, dando lugar a un modelo exclusivamente de vértices o a uno de centros. Sus propiedades se ilustran en simulaciones de monocapas sujetas a una extensión impuesta y durante el proceso de cicatrizado de heridas. La evolución de las fuerzas y los efectos del EPM durante el remodelado se analizan en estos ejemplos.

Acknowledgements

First and foremost, I would like to express my sincere gratitude to my advisor Prof. Jose Javier Muñoz for the continuous support of my Ph.D study and related research, for his patience, motivation, immense knowledge, and wonderful mentorship.

I also appreciate Prof. Yanlan Mao and Prof. Antonio Rodríguez-Ferran for their fruitful advices and great guidance. Besides, I would like to thank Dr. Daniel Millán and Dr. Rob Tetly for their collaboration and helpful comments.

I would like to express my thanks to all my colleagues at LaCàN, UPC, whom I am sincerely feel grateful to, especially Dr. Nina Asadipour.

During my two two-month visits at Laboratory for Molecular Cell Biology (LMCB) at University College London, I had the chance to collaborate and discuss related topics with wonderful people. Among them I feel especially fortunate to know Dr. Melda Tozluoglu and Dr. Nargess Khalilgharibi.

I acknowledge the partial financial support of the Spanish Ministry of Economy, Science and Competitiveness (MINECO) under grants DPI2013-32727-R and DPI2016-74929-R, Generalitat de Catalunya under grant 2014-SGR-1471, European Molecular Biology Organisation (EMBO) under grant ASTF 351-2016, and foundation Ferran Sunyer i Balaguer under grant FSB 2015.

Last but not the least, I would like to thank my family. Words cannot express how grateful I am to my parents for all of the sacrifices that you have made on my behalf.

Contents

List of Figures

List of Tables

Chapter 1

State of the art

1.1 Biological background

In the last two decades, there has been a shift in the understanding of cell function and disease within the other contexts than biochemistry and genetics. In particular, it has become well established that critical insights into diverse cellular processes and pathologies can be gained by understanding the role of mechanical force (Munjal et al., 2015; Fernández-Sánchez et al., 2015). A rapidly growing body of science indicates that mechanical phenomena are critical to the proper functioning of several basic cell processes and that mechanical loads can serve as extracellular signals that regulate cell function (Jacobs et al., 2012).

In many aspects of biological development, what matters is how mechanical aspects of cells behaviours, entailed by sub-cellular phenomena such as genetic regulation and protein activity, act a significant role in many morphogenic and physiologic phenomena at tissue level. This point of view considers the cell as the fundamental module of development (Roland & Glazier, 2005). Holding this attitude, questions like *Where and when do cells move?*, *Which cells generate force and which cells are passively moulded by forces generated elsewhere?* or *What are the mechanical properties of cells and tissues that determine the effect of these forces?*, can shape a new point of view towards many unsolved problems in tissue biology.

Some phenomena during embryonic development such as gastrulation, in which single-layered blastula reorganised into a trilaminar, has been well explained in terms of mechanical perspective (Keller et al., 2003)(see Figure 1.1). The biomechanics of the relation of the cell shape change to the tissue bending has been established by physical (Lewis, 1947) and mathematical modelling. For instance, a mechanical model for the morphogenetic folding of embryonic epithelia based on hypothesised mechanical properties of the cellular cytoskeleton has been described in Odell et al. (1981). Also, animal-vegetal apical contraction of bottle cells forming *in vivo*,

during *Xenopus laevis* gastrulation was studied by a mechanical approach (Hardin & Keller, 1988). Moreover, there have been also reports on other mechanical cellular behaviours such as cell intercalations during convergent extension, within which a number of theoretical models have been proposed to describe such morphogenic phenomena (Davidson et al., 2010) (see Figure 1.1).

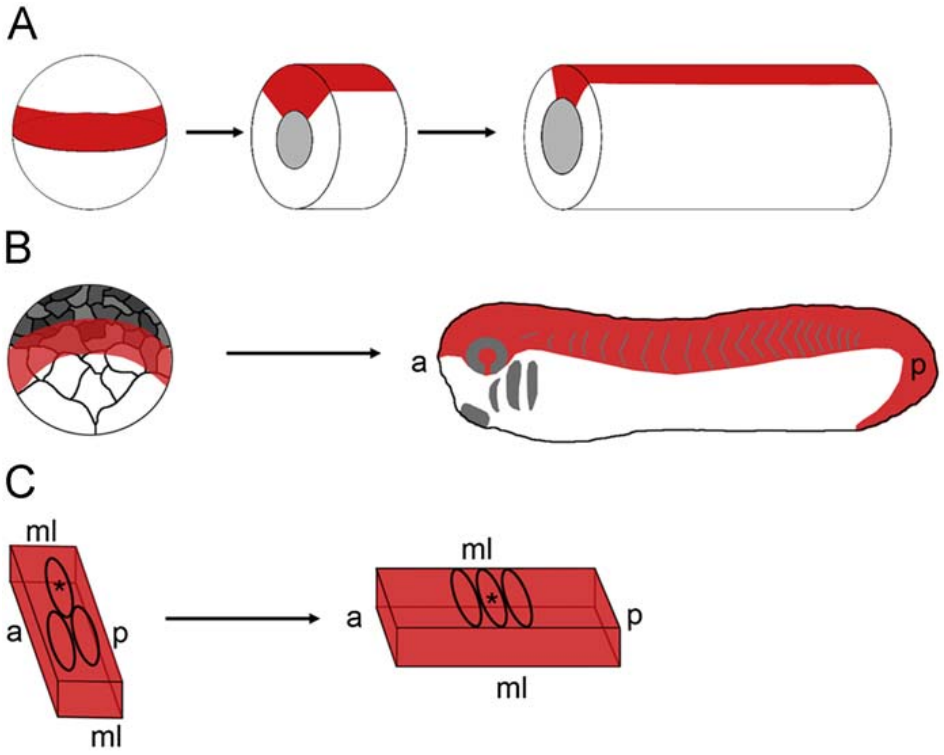

Figure 1.1: Gastrulation, elongation, convergent extension, and mediolateral cell intercalation. (A) Gastrulation is shown as a topological process that converts a ball into a toroid and then elongates the toroid into a tube. (B) Gastrulation and elongation produce a tadpole, analogous to a tube, from a ball of cells.(C) Convergent extension (CE) of dorsal tissues (red) in the embryo is the result of cell rearrangement in the tissue. Cells (drawn as ellipses) intercalate between their mediolaterally (ml) adjacent neighbours driving them apart along the anterior-(a)-posterior-(p) axis. Several rounds of mediolateral cell intercalation drive convergent extension and elongate the embryo (Davidson et al., 2010).

1.2 Modelling in tissue biology

1.2.1 Modelling scale and predictability

Although a simulation can never prove sufficiency, and the mechanism may not be completely correct due to missing components, they can prove their utility by predicting, rather than *"post-dicting"* experimental observations, and testing hypothesis that may be notable to biologists (Roland & Glazier, 2005). A computational treatment of a particular problem must begin by choosing an appropriate scale or level of detail, which the inclusion of additional scales can later refine.

Most of computational-biology studies of development focus on tissue level phenomena, modelling tissues as continuous elastic solids or viscous fluids. Others aim to generalise from an understanding of single-cell behaviours and dynamics, building microscopic models of intracellular dynamics (e.g. electro-physiological models or single-cell models of filopodial extension) (Roland & Glazier, 2005). Indeed, some authors aim to couple many detailed single-cell models in order to model multicellular phenomena (Krul et al., 2003).

Instead, molecular and sub-cellular models like *Virtual Cell* (Slepchenko et al., 2003), *Silicon Cell* or E-cell (Tomita et al., 1999) provide great detail on aspects of sub-cellular processes. However, working at the scale of the cell provides a natural level of abstraction for mathematical and computational modelling of embryo development. The study of cells from the mathematical standpoint, immediately reduces the interactions of roughly ~ 100 gene products to 10 or so behaviours: cells can move, divide, die, differentiate, change shape, exert forces, secrete and absorb chemicals and electrical charges, and change their distribution of surface properties (Roland & Glazier, 2005). Some cell-based models, that make use of the genes products, are *Compucell3D* (Roland & Glazier, 2005) and Chaste (Cancer, Heart and Soft-Tissue Environment) (Pitt-Francis et al., 2009).

1.2.2 Major modelling approaches

Mechanical analysis of embryonic tissues has gained attention in recent years. Biologists and experimentalists have been able to accurately track the kinematic information of tissues and organs, but the mechanical forces that drive these shape changes have resulted far more elusive, despite evidence that genetic expression and mechanics are tightly coupled in phenomena such as cell migration (Sunyer et al., 2016), wound healing (Brugués et al., 2014) or embryo development (Fernández-Sánchez et al., 2015).

The quantification of the mechanical forces in morphogenesis has given rise to numerous and diverse numerical approaches. In the context of tissue modelling at

the cell scale, there are two major frameworks implemented so far: *continuum* and *cell-based* (or *discrete*) approaches. Here we provide a brief description of either of these procedures.

Continuum models

In this approach the tissue is assumed to be uniform in terms of cell density, and without gaps. In fact the effect of individual cells are averaged out (Osborne et al., 2010) and there is a tendency to lump multiple physical properties into one or two phenomenological parameters (Macklin et al., 2010). For example the models by Frieboes et al. (2007); Macklin & Lowengrub (2007) lump cell–cell, cell-BM (bone marrow), and cell-ECM (extracellular matrix) adhesion, motility, and ECM rigidity into a single *mobility* parameter, as well as forces on the tumour boundary. One of the main advantages of these models is that they allow to use well-known discretisation methods such as the Finite Element Method or derived approaches (Arroyo & DeSimone, 2014; Muñoz et al., 2007; Lin & Taber, 1994). However, one reason why continuum models that are able to recover detailed morphological features are scarce, is that some cellular interactions are difficult to simulate at the macroscopic scale. One basic problem is the representation of cell–cell adhesion. In cell-based models, cell–cell adhesion can conveniently be expressed in the shape of an inter-cell attraction. In meso-scale continuum models, the notion of a single cell does not exist, and we have to model the macroscopic effect of cell–cell adhesion (Bergdorf et al., 2010).

Cell-based (discrete) models

Under the title of cell-based modelling, the behaviour of one or more individual cells is addressed as they interact with one another and the micro-environment.

These models treat material as discontinuous matter *ab initio*. This approach has enjoyed a long history in applied mathematics and biology, dating as far back as the 1940s when John von Neumann applied lattice crystal models to study the necessary rulesets for self-replicating robots (Neumann & Burks, 1966). Today, discrete cell modelling has advances to study a broad swath of cancer biology, spanning carcinogenesis, tumour growth, invasion, and angiogenesis (Macklin et al., 2010).

Discrete, or individual-based models are generally divided into two categories: *lattice-based* (inluding cellular automata) and *lattice-free* (agent-based) models.

(I) Lattice-based models: In lattice-based modelling, the cells are confined to a regular two- or three-dimensional lattice. Each computational mesh point is updated in time according to deterministic or stocastic rules derived from physical conservation laws and biological constraints. Some models use a high resolution

mesh to discretise the cells and the surrounding micro-environment with sub-cellular resolution, allowing a description of the cells finite sizes, morphologies, and biomechanical interactions. Cellular automata (CA) models, which describe each cell with a single computational mesh point, can be viewed as a specific case of this approach (Macklin et al., 2010).

(II) Lattice-free models: Lattice-free models, frequently referred to as agent-based models, do not restrict the cells positions and orientations in space. This allows a more complex and accurate coupling between the cells and their micro-environment, and imposes fewer artificial constraints on the behaviour of multi-cellular systems. The cells are treated as distinct objects or agents and are allowed to move, divide, and die individually according to biophysically-based rules. This framework is usually defined under two approaches: *cell-vertex* and *cell-centred* models (Macklin et al., 2010).
***(i) Vertex models*:** Cells are treated as polygons in 2-D (Spahn & Reuter, 2013) or polyhedra in 3-D (Okuda et al., 2013; Honda et al., 2004) and a multicellular aggregate is represented by a single network comprising vertices and edges (Okuda et al., 2013). In vertex models, size, shape, and the dynamics of each cell is governed by the movement of its vertices, these being determined by explicitly calculating the resultant forces or minimising a global energy function (Osborne et al., 2010). Vertex models are particularly suitable for modelling differential cell–cell adhesion, an important feature of cell dynamics in the crypt, as common mutation in colorectal epithelial cells are thought to affect cell–cell adhesion. However, the inclusion of differential cell-substrate adhesion is not so straightforward, as the drag terms include contributions from cells surrounding a given vertex (Fletcher et al., 2010; Osborne et al., 2010).
***(ii) Cell-centred models*:** In this approach, each cell is treated as a discrete entity and adjacent cells are connected by bar elements between their geometrical centres, while evolving through a specific rheological law. Neighbouring cells are determined by a Delaunay triangulation while cell shapes are generally determined by a Voronoi tessellation. The equations of motion are developed by neglecting inertial effects and balancing elastic force and viscous drag on cell centres with cell–cell interaction forces associated with the compression and extension of the connecting bar elements (Mosaffa et al., 2015; Osborne et al., 2010).

Cell-centred models can efficiently simulate cell proliferation, growth, and migration in the crypt (Fletcher et al., 2010). Moreover, it is straight forward to incorporate differential cell–cell adhesion (Galle et al., 2005; Walker et al., 2004; Ramis-Conde et al., 2008; Schaller & Meyer-Hermann, 2005) and to vary cell-substrate adhesion by varying the cellular drag coefficients. However, a disadvantage of such cell-centred models is their reliance on the Delaunay triangulation, meaning that the number of vertices and the shapes of the cells do nat change smoothly (Broadland,

2004).

1.3 Objectives and proposed model

The aim of this thesis is to present an approach to model multicellular systems, with hundreds of cells. Therefore, it is appropriate to focus the procedure at the cell rather than the sub-cellular scale. Other methods for modelling cell mechanics such as the Sub-cellular Element Model (Sandersius & Newman, 2008; Sandersius et al., 2011) or the Immersed Boundary method (Rejniak, 2007) are more suitable at smaller scales and therefore can simulate cell–cell interaction more accurately.

In the previous section, we addressed a set of characteristics provided by vertex and cell-centred models. The model proposed in this thesis aims to gather the advantages of the two approaches: define cell–cell interactions between centres and at the cell–cell junctions, but include the cell as an essential unit in order to ease the transitions in the cell–cell contacts. We resort to Delaunay triangulation of the cell-centres, and a barycentric interpolation of the vertices on the cell boundaries. Both nodes (cell centres) and vertices are kinematically coupled by this interpolation, which has effects on the resulting equilibrium equations.

The proposed model is an extension of an initially developed cell-centred model (Mosaffa et al., 2015) with a hybrid approach that incorporates mechanics at the cell boundaries in order to model morphogenetic events driven by contractile forces (Salbreux et al., 2012), like for instance germ band extension (Munjal et al., 2015) or wound healing (Antunes et al., 2013). Hybrid approaches are scarce and have been so far employed to model glass and jamming transitions in tissues (Bi et al., 2016) as well as in topological characterisation of developing epithelial tissues (González-Valverde & García-Aznar, 2017).

Since topological changes are commonly observed during embryo development, and may determine the global tissue deformation (Lecuit & Lenne, 2007), the model aims to handle these changes in a robust manner, by introducing a method to compute resting length of remodelled elements based on the element direction in space. Remodelling of cell–cell connectivities is controlled by resorting to Delaunay triangulation of the set of cell centres.

The use of Voronoi tessellation has been well studied for domain decomposition (Fu et al., 2017) or for discretising partial differential equations in elasticity, diffusion, fluid dynamics or electrostatics. Some examples are the Natural Element Method (Cueto et al., 2002; González et al., 2007; Sibson, 1980; Sukumar, 2003), the Voronoi Cell Finite Element Method (Ghosh & Moorthy, 2004; Moorthy & Ghosh, 1996), the Voronoi Interface Element (Guittet et al., 2015) or the particle-in-cell

methodology (Gatsonis & Spirkin, 2009). In these methods, the tessellation is used for either constructing the interpolation functions, or describing the heterogeneities of interfaces.

At a first stage, we resort to Voronoi tessellation of the cell centres in order to obtain the cells boundary. Constructing cells boundary is included as a post-processing event in the model, since cells vertices are assigned with no mechanical role.

At a later stage, we introduce a hybrid approach where we include a second type of bar elements connecting cell vertices to involve interactions at the cells boundary. This approach allows considering different mechanical interactions, governed by different rheological laws, at the cells boundary rather than at the cells cytoskeleton. Furthermore, we will limit our focus on two-dimensional flat monolayers thereupon.

To define the cells boundary we resort to a related barycentric tessellation, where the vertices of the network are built from the barycentres of each triangle instead of the bisectors, as it is the case in the Voronoi diagram. We choose this alternative tessellation to guarantee that the vertices are inside each triangle, even when the Delaunay triangulation is deformed, and thus may potentially violate the Delaunay condition. The use of automatic tessellation is also motivated in our case by the need to handle cell–cell connectivity changes in a robust and accurate manner, and thus avoid the design of specific algorithms during remodelling events, as it is customary in vertex models in two (Fletcher et al., 2013; Honda et al., 1983) and three dimensions (Honda et al., 2008; Okuda et al., 2015).

The position of cells in the hybrid approach is obtained by acquiring mechanical equilibrium at the cell centres. The forces at the boundary of each cell take part in the equilibrium equation of the cell centre by translation of the residual forces at the vertices, into the cell centres, through the barycentric interpolation mentioned before. This clearly does not guarantee mechanical equilibrium at the vertices. However, we introduce a method in which the vertices are allowed to relax by slightly taking some distance from the triangles barycentres.

Handling cells equilibrium after reorganisation is performed by introducing an Equilibrium Preserving Mapping (EPM), by which resting lengths of the elements are defined in such way that preserves mechanical equilibrium at the cell centres for the current topology.

1.4 Outline

Chapter 2 begins by providing a description of a purely cell-centred approach, where each cell is represented by a particle, and each cell–cell interaction is modelled through a bar element connecting two particles. This element carries all the interactions at the junctions between the cells, and also the internal active and passive forces produced by the cytoskeleton. The position of cell centres then, is defined by resorting to mechanical equilibrium of the network of the bar elements. Delaunay triangulation of the set of cell centres is presented as a robust algorithm to define the network of cell–cell connections, later called *nodal* network. We also present a L-tensor method to preserve mechanical equilibrium at cell centres for networks of cell centres with variable topology.

Cells boundary is defined by a modified Voronoi tessellation of the cell centres, providing a *vertex* network with closed regions at the bounds of the tissue. Later, we introduce a hybrid approach where mechanical interaction featured also along the cells boundary, is coupled with that of along the bar elements between the cell centres. At this stage, barycentric tessellation of the Delaunay network substitutes Voronoi tessellation to define cells boundary. To preserve mechanical equilibrium in tissues with variable topology we present EPM as a method to recompute appropriate resting lengths for nodal and vertex elements in such a way that mechanical equilibrium is preserved at cell centres.

Chapter 3 is dedicated to implementation of some appropriate constitutive laws applied on the bar elements, that mimic the non-linear mechanical response of multicellular systems. This is the result of multiple local phenomena acting at different scales. At the micro-scale the cytoskeleton can undergo (de)polymerisation process (Ma et al., 2009), cross-link reorganisation (Chaudhuri et al., 2007), or affect the cytoplasm flow (Moeendarbary et al., 2013). At the macro-scale, cell motility is driven by cell–cell and cell–extracellular matrix adhesive forces, lamellipodia activity or other intercalation forces. The combination of these multi-scale forces into global changes during embryogenesis such as convergent extension (Beret et al., 2004; Pare et al., 2014), or anisotropic tissue growth (Bittig et al., 2008).

We do not intend to include all this range of multi-scale forces in the bar elements of our model, but just a subject of the observed mechanisms that may be sufficient to reproduce some of the observed morphogenetic movements. In our model we implement a strain-dependent evolution of the resting length, at cell–cell connections as well as cells boundary, in a similar manner to a time-varying reference configuration in continuum models (Muñoz et al., 2007; Rodriguez et al., 1994).

In Chapter 4 we provide a set of numerical results obtained by the application

of the model, including tissue extension and wound healing incorporating different features in the model such as reorganisation of the cells and contractility at the cells junctions.

Chapter 2

Tissue discretisation

2.1 Cell-centred model

We will henceforth focus our study to cellular systems forming either a monolayer (planar or curved) and a three-dimensional aggregate. We will consider the following assumptions:

(a) Cells are packed with no extracellular space in between.

(b) Cell centres are considered as dimensionless points (later mentioned as *nodes*) by which the location of each cell is defined in space.

(c) Contact between two cells i and j is defined by the presence of a one-dimensional bar element connecting the two cell centres, providing a connected graph as a whole. This graph consists in triangulation of the domain into N_{tri} triangles $\mathcal{T}^I$, $I = 1, \ldots, N_{tri}$ and N_D edges.

(d) Inertial forces can be neglected.

In most of our examples, we will simulate cell monolayers. Indeed, during the early stages of embryogenesis, prior to any mesenchymal transformations, cells tend to form a monolayer (Costa et al., 1993). This may be eventually internalised and cells may turn into a cell aggregate. We will discuss tissues with either architecture separately, but will ignore transitional states. Assumption (a-c) are considered to simplify the computations. In most cases, we will also assume that the number of cells (nodes), N_{nodes} is constant. This is consistent with the fact that when cells undergo drastic deformations, no proliferation takes place, that is, the number of cells remains approximately constant (Leptin & Grunewald, 1990). In the simulations that involve wounding, this assumption will be relaxed, and the number of nodes may diminish. Assumption (d) is based on the fact that in cellular systems, inertial forces are negligible compared to elastic and viscous forces.

The configuration of the model at each time-step t_n, denoted by $\boldsymbol{C}_n$, is defined by the nodal position of the N_{nodes} nodes, $\boldsymbol{X}_n = \left\{\boldsymbol{x}_n^1, \boldsymbol{x}_n^2, \ldots, \boldsymbol{x}_n^{N_{nodes}}\right\}$, the connectivity between nodes, indicated by a connectivity matrix, $\boldsymbol{T}_n$. The two sets of variables $\boldsymbol{X}_n$ and $\boldsymbol{T}_n$ may vary between time-steps, and are computed from the previous variables $\boldsymbol{C}_n$ according to the following scheme:

1. Compute nodal coordinates $\boldsymbol{X}_{n+1}$ by finding *mechanical equilibrium* between the particles, while keeping the connectivity $\boldsymbol{T}_n$ constant.

2. *Update connectivities* $\boldsymbol{T}_{n+1}$ resorting to a Delaunay triangulation of the new positions $\boldsymbol{X}_{n+1}$

Figure 2.1 shows the two-step update process. Note that according to the scheme above, equilibrium at time t_{n+1} is computed for the connectivity at time t_n. The connectivity $\boldsymbol{T}_n$ may not be suitable for the new positions $\boldsymbol{X}_{n+1}$, and for this reason the cell-cell contacts are updated, yielding a new connectivity $\boldsymbol{T}_{n+1}$. Steps 1-2, mechanical equilibrium and connectivity definition, will be discussed in the next paragraphs.

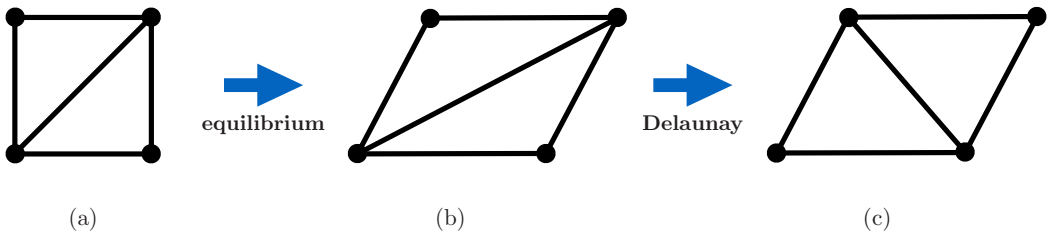

Figure 2.1: Two-step update process of nodal configuration. (a) Configuration $\boldsymbol{C}_n = \{\boldsymbol{X}_n, \boldsymbol{T}_n\}$ at time t_n, (b) Nodal configuration $\boldsymbol{C}^*_{n+1} = \{\boldsymbol{X}_{n+1}, \boldsymbol{T}_n\}$ after obtaining mechanical equilibrium, and (c) configuration $\boldsymbol{C}_{n+1} = \{\boldsymbol{X}_{n+1}, \boldsymbol{T}_{n+1}\}$ at time t_{n+1}.

2.1.1 Cell-centred mechanical equilibrium

The cell-cell connectivity defined by $\boldsymbol{T}$ includes information on the set of N_D pairs ij of bar elements between the N_{nodes} nodes. Each pair of connected nodes are joined with a bar element that represents the forces between the two cells. This force is derived here from an elastic strain function,

$$\begin{aligned} W_D^{ij}(\boldsymbol{x}) &= \frac{1}{2} k_D (\varepsilon^{ij})^2, \\ W_D(\boldsymbol{x}) &= \sum_{ij}^{N_D} W_D^{ij}(\boldsymbol{x}), \end{aligned} \tag{2.1}$$

where k_D is the material inter-cellular stiffness, $\varepsilon^{ij} = \frac{l^{ij} - L^{ij}}{L^{ij}}$ is the scalar elastic strain, and $l^{ij} = \left\|\boldsymbol{x}^i - \boldsymbol{x}^j\right\|$ and L^{ij} are the *current* and *reference* lengths, respectively. In Section 3.3 we will introduce a rheological law where the reference length

L^{ij} (stress-free length of the element) is allowed to vary along time, and thus we may have that $L^{ij} \neq L_0^{ij} := \left\| \boldsymbol{x}_0^i - \boldsymbol{x}_0^j \right\|$. W_D is the total strain function of the network of nodes.

We remark that the elastic strain function in equation (2.1) is quadratic with respect to the strain, but that our strain measure depends non-linearly on the position $\boldsymbol{x}^i$. This makes the forces to vary non-linearly when the bars turn and the displacements are large, which is the general case considered here. This geometrical non-linearity may be complemented with other material non-linearities, and in fact, viscous effects will be considered when the resting length L is allowed to change in Section 3.3. Other alternative non-linear strain functions have been considered in similar bar systems when simulating tissue fluidisation (Asadipour et al., 2016), relaxation (Khalilgharibi et al., 2017) or embryogenesis (Doubrovinski et al., 2017).

In the absence of any other strain function, the minimisation of W_D leads to the equations

$$\boldsymbol{g}_D^i := \sum_{j \in S^i} \boldsymbol{t}_D^{ij} = \boldsymbol{0}, \ i = 1, \dots, N_{nodes}, \tag{2.2}$$

where S^i denotes the set of nodes connected to node i and $\boldsymbol{t}_D^{ij}$ is the nodal traction at node i due to bar ij, which is derived from the elastic strain function W_D^{ij} as (no summation on i)

$$\begin{aligned} \boldsymbol{t}_D^{ij} &= \frac{\partial W_D^{ij}}{\partial \boldsymbol{x}^i} = k_D \varepsilon^{ij} \frac{1}{L^{ij} l^{ij}} (\boldsymbol{x}^i - \boldsymbol{x}^j), \\ \boldsymbol{t}_D^{ji} &= \frac{\partial W_D^{ij}}{\partial \boldsymbol{x}^j} = k_D \varepsilon^{ij} \frac{1}{L^{ij} l^{ij}} (\boldsymbol{x}^j - \boldsymbol{x}^i). \end{aligned} \tag{2.3}$$

Therefore,

$$\boldsymbol{t}_D^{ij} = \frac{\partial W_D^{ij}}{\partial \boldsymbol{x}^i} = -\boldsymbol{t}_D^{ji} = -\frac{\partial W_D^{ij}}{\partial \boldsymbol{x}^j}. \tag{2.4}$$

Figure 2.2 shows the traction vectors between two nodes $\boldsymbol{x}^i$ and $\boldsymbol{x}^j$. Since the system of equations (2.2) is non-linear with respect to the nodal positions $\boldsymbol{x}^i$, we resort to a full Newton-Raphson method, which requires linearisation of the set of equations. The expression of the resulting Jacobian can be obtained by using the expression in Appendix E.2 and using $L = const.$, that is $\frac{\partial L}{\partial l} = 0$.

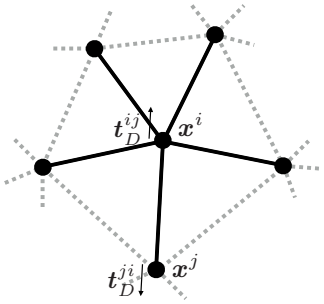

Figure 2.2: Schematic view of node i connectivity (continuous lines), within the rest of the network (dashed lines) and traction vector $\boldsymbol{t}_D^{ij}$.

2.1.2 Cell-cell connectivity: modified Delaunay triangulation

Triangulation of planar monolayers

Definition For a set $\boldsymbol{P}$ of points in the plane, *Delaunay triangulation* is a triangulation $DT(\boldsymbol{P})$ such that no point in $\boldsymbol{P}$ is inside the circumcircle of any triangle in $DT(\boldsymbol{P})$ (Barber et al., 1996; Okabe et al., 1992).

Delaunay triangulation of a set of points $\boldsymbol{P}$ in three-dimensional domain, leads to a network with tetrahedrons as building blocks of the network. In such a network, Delaunay triangulation also guarantees no point in $\boldsymbol{P}$ is inside the circumsphere of any tetrahedron in $DT(\boldsymbol{P})$.

According to the definition above, following properties of DT can be deduced:

- Delaunay triangulation maximise the mean in-radius of the set of triangles in the domain (Lambert, 1994). This property ensures triangles–and tetrahedrons in 3-D–with optimal aspect ratio which can improve numerical precision in finite element problems (Babuska & Aziz, 1976).

- Delaunay triangulation guarantees first-neighbour connection, i.e. any point at each triangle is as close as possible to a node. When defining cell boundaries, this property will help obtaining cell shapes with maximum aspect ratio. The idea of plump cells is supported by the fact that epithelial cells tend to minimise their contact length with the surrounding cells (Honda et al., 1982).

- Delaunay triangulation of a set of points results in the convex hull of that set of points. This property does not preserve concave boundaries of the triangulated domain.

Figure 2.3 shows three different types of triangulation of set of points $\boldsymbol{P}$ while the condition of Delaunay triangulation being evaluated.

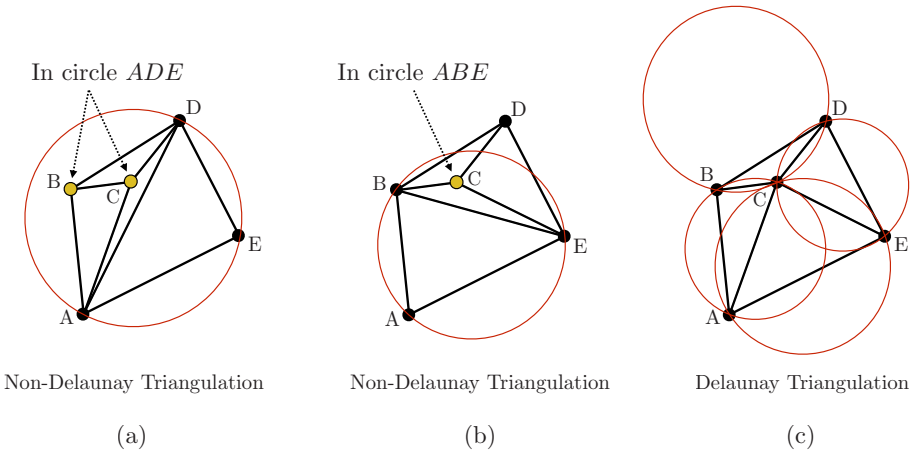

Figure 2.3: Triangulation of set of points $\boldsymbol{P} = \{A, B, C, D, E\}$. (a) non-Delaunay triangulation as points B and C are inside the circumcircle of $\triangle ADE$. (b) non-Delaunay triangulation as point C is inside the circumcircle of $\triangle ABE$. (c) Delaunay triangulation as there is no point inside the circumcircle of either of triangles.

Modification of Delaunay triangulation

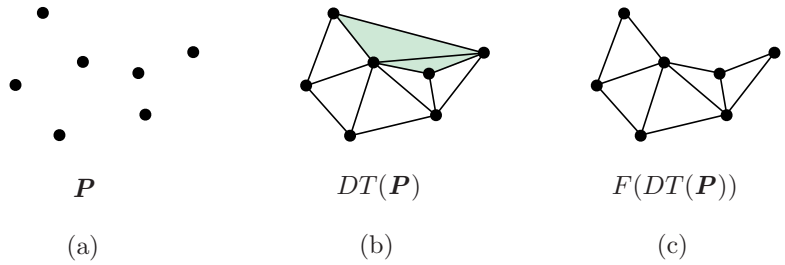

Figure 2.4: Modified Delaunay triangulation of set of points $\boldsymbol{P}$. (a) Distribution of set of points $\boldsymbol{P}$ in the plane. (b) Standard Delaunay triangulation of set of points $\boldsymbol{P}$; skinny triangles covering the concave edge of the network are marked in green. (c) Modified Delaunay triangulation of set of points $\boldsymbol{P}$ by the application of the filtering process on $DT(\boldsymbol{P})$.

Since Delaunay's algorithm yields the convex hull of all the points, a basic Delaunay triangulation $DT(\boldsymbol{P})$ may invariably lead to distant boundary nodes being unrealistically connected, i.e. covering non-convex boundaries. In order to overcome this problem, those elements with very high aspect ratio were eliminated by defining a filtering process (see Figure 2.4). The ratio $\frac{r}{R}$ where r is the inradius and R is the circumradius of each triangle (tetrahedron in 3-D), has been considered as an appropriate criterion to filter undesirable simplexes,

$$\frac{r}{R} < tol_R. \tag{2.5}$$

Equation (2.5) shows the condition under which an external element is removed. tol_R is the tolerance defined with respect to the range of aspect ratio in external triangles and tetrahedrons in two- and three-dimensional domains, respectively, which we take equal to 0.54. We note that other more sophisticated approaches such as alpha shapes (Edelsbrunner & Mücke, 1994) could have been considered. Howsoever, the simpler equation (2.5) has been shown to be sufficient in our examples.

In Appendix B, the ratio $\frac{r}{R}$ is calculated in terms of the position of the vertices for an arbitrary triangle in 2-D as well as an arbitrary tetrahedron in 3-D. Figure 2.5 shows inradius and circumradius of $\triangle ABC$.

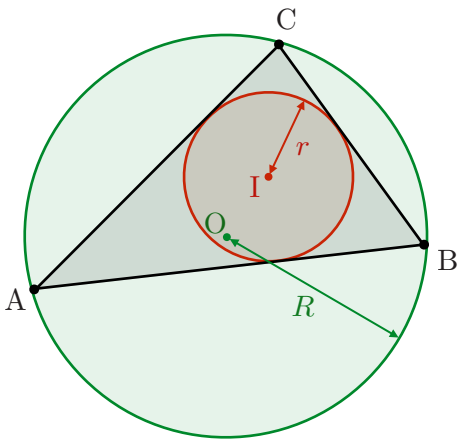

Figure 2.5: Incircle I and circumcircle O of $\triangle ABC$. r and R are inradius and circumradius of $\triangle ABC$ respectively.

Application of Delaunay triangulation on the model

To obtain cell-cell connectivity, we resort to Delaunay Triangulation (DT) (Barber et al., 1996) of the set of nodes $\boldsymbol{X}_{n+1}$, yielding $\tilde{\boldsymbol{T}}_{n+1} = DT(\boldsymbol{X}_{n+1})$, which may contain skinny triangles covering non-convex boundary of the tissue. By applying filtering process, denoted by $\boldsymbol{F}$, a new connectivity $\boldsymbol{T}_{n+1} = \boldsymbol{F}(DT(\boldsymbol{X}_{n+1}))$ is obtained, which does not include the unrealistic elements on the boundary. Figure 2.6 shows schematically the sequence of the whole process in Section 2.1.1 and the planar triangulation described here for a set of nine nodes. Configuration in Figure 2.6b is computed after imposing mechanical equilibrium on the triangulation in Figure 2.6a. The connectivity in Figure 2.6c is obtained by basic Delaunay triangulation, while the one in Figure 2.6d is the result of applying the filtering process.

Between consecutive time-steps or loading steps, the changes in the connectivity may induce drastic changes in the nodal forces if the resting length L is set to the new current length of newly created elements. In order to alleviate these discontinuities,

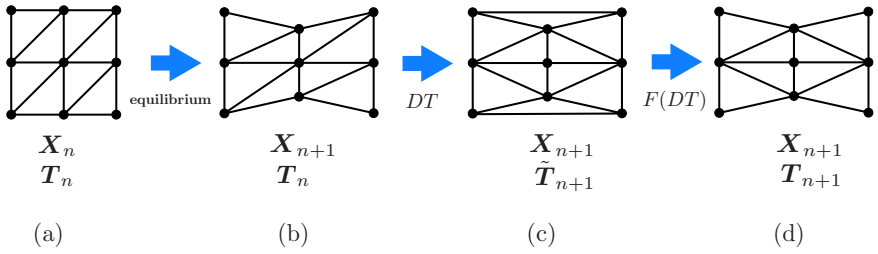

Figure 2.6: Schematic of computational process for retrieving nodal positions an connectivity $\{\boldsymbol{X}_{n+1}, \boldsymbol{T}_{n+1}\}$ from the same quantities at time t_n. (a)→(b): computation of new positions $\boldsymbol{X}_{n+1}$ from mechanical equilibrium. (b)→(c): computation of new connectivity $\tilde{\boldsymbol{T}}_{n+1}$ from Delaunay triangulation. (c)→(d): trimming of Delaunay connectivity $\tilde{\boldsymbol{T}}_{n+1}$, resulting in a not necessarily convex boundary of the cell-centred network $\boldsymbol{T}_{n+1}$.

a specific remodelling algorithm that defines a nodal based resting length tensor is presented next.

2.1.3 Remodelling of cell-centred model: L-tensor method

The nodal forces are based on the elastic strain function defined in Section 2.1.1, which depends on the current l and reference length L, which so far has been considered constant. However, due to the redefinition of the cell-cell connectivity, detailed in Section 2.1.2, it may well be that the element ij exists at time t_{n+1} but not at time t_n. For this reason, we compute a nodal *active length tensor*, $\mathbf{L}^i$, which will allow us to compute the resting length along an arbitrary direction $\boldsymbol{n}^j$ as

$$L^{ij} = \boldsymbol{n}^j \cdot \mathbf{L}^i \boldsymbol{n}^j. \tag{2.6}$$

This relation reveals that $\mathbf{L}^i$ may be interpreted as a strain tensor, where the quantity $\boldsymbol{n}^j \cdot \mathbf{L}^i \boldsymbol{n}^j$ corresponds to the stretching along $\boldsymbol{n}^j$. Since the skew part of $\mathbf{L}^i$ does not affect the value of L^{ij} in equation (2.6), and in order to keep similarity between $\mathbf{L}^i$ and a deformation tensor, we will assume that $\mathbf{L}^i$ is symmetric.

It is clear that for a given node i, the existance of an active length tensor $\mathbf{L}^i$ satisfying exactly relationship in equation (2.6) for all current cell–cell connections ij may not be possible. Therefore, the tensor $\mathbf{L}^i$ is computed by minimising the following quadratic error function:

$$E^i_{\mathbf{L}} = \frac{1}{2} \sum_{j=1}^{S^i} \left\| \mathbf{L}^i \boldsymbol{n}^j - L^{ij} \boldsymbol{n}^j \right\|^2. \tag{2.7}$$

We note that, in view of equation (2.6), we could alternatively aim to minimise the error function $\tilde{E}^i_{\mathbf{L}} = \frac{1}{2} \sum_{j=1}^{S^i} \left\| \boldsymbol{n}^{jT} \mathbf{L}^i \boldsymbol{n}^j - L^{ij} \right\|^2$. We have not done so for reasons that will be explained below, when commenting the uniqueness of the minimiser.

Due to the symmetry of tensor $\mathbf{L}^i$, we will right this tensor in the forms

$$\bar{\mathbf{L}}^i_{2D} = \{L_{xx}, L_{yy}, L_{zz}\}^T,$$
$$\bar{\mathbf{L}}^i_{3D} = \{L_{xx}, L_{yy}, L_{zz}, L_{xy}, L_{xz}, L_{yz}\}^T,$$

so that $\mathbf{L}^i \boldsymbol{n}^j = \mathbf{N}^j \bar{\mathbf{L}}^i$, with $\mathbf{N}^j$ a matrix that contains the components of the unit vector $\boldsymbol{n}^j$. Then, the error $E^i_{\mathbf{L}}$ reads

$$E^i_{\mathbf{L}} = \frac{1}{2} \sum_{j=1}^{S^i} \left\| \mathbf{N}^j \bar{\mathbf{L}}^i - L^{ij} \boldsymbol{n}^j \right\|^2,$$

and its derivative with respect to each one of the components of $\mathbf{L}^i$ gives rise to the system of equations

$$\mathbf{A} \bar{\mathbf{L}}^i = \mathbf{b} \tag{2.8}$$

with

$$\mathbf{A} = \sum_{j=1}^{S^i} \mathbf{N}^{jT} \mathbf{N}^j \quad , \quad \mathbf{b} = \sum_{j=1}^{S^i} L^{ij} \mathbf{N}^{jT} \boldsymbol{n}^j.$$

The error measure $E^i_{\mathbf{L}}$ in equation (2.7) is a quadratic function that has a unique minimiser as far as the vectors $\boldsymbol{n}^j$ span $\mathbb{R}^{n_{sd}}$, with n_{sd} the number of space dimensions. Appendix C gives a proof of this fact. The symmetry of $\mathbf{L}^i$ is not required in the proof of uniqueness, which opens the possibility for considering a non-symmetric tensor $\mathbf{L}^i$. However, in this case, the system of equations in (2.8) contains more unknowns, wihtout any qualitative improvement in the retrieved active lengthening $L^{ij} = \boldsymbol{n}^j \cdot \mathbf{L}^i \boldsymbol{n}^j$. Furthermore, and although we do not prove it here, we point out that other alternative error measures as the function $\tilde{E}^i_{\mathbf{L}}$ mentioned above would not guarantee a unique minimiser, even if the vectors $\boldsymbol{n}^j$ span $\mathbb{R}^{n_{sd}}$.

The computation of the nodal strain tensor through equation (2.8) allows us to compute the resting lengths along the directions of the new elements when connectivity changes occur. We emphasise that this system of equations is solved during the remodelling process after each time-step, while keeping the nodal positions fixed.

2.1.4 Cell-centred model for curved monolayers

Triangulation of curved manifolds

To obtain the new triangulation at step (c) in Figure 2.6 for a curved tissue, including the filtering process of Delaunay triangulation, we resort to a non-linear dimensionality reduction method (NLDR) to embed the three-dimensional scattered

set of points describing the cell centres in a two-dimensional embedding. In general, NLDR techniques suppose that the input high-dimensional point-set either lies on or is close enough to a low dimensional manifold (in our case a two-dimensional manifold) that also is an open set (see for instance Carreira-Perpiñán (1997), Lee & Verleysen (2007), and Maaten et al. (2009)).

Here we use a robust and efficient variation of the well known local linear embedding (LLE) technique (Roweis & Saul, 2000), that is the modified local linear embedding (MLLE) (Zhang & Wang, 2007)). LLE-based methods assume that each point of the manifold can be locally approximated by a linear combination of its k-nearest neighbours ($k-nn$). LLE ignores metric information producing low-dimensional embedding of unit covariance through a minimisation process that involves eigenvalue decomposition of sparse matrices. The reader is referred to Roweis & Saul (2003), Roweis & Saul (2000) and Zhang & Wang (2007) for full details, and to Millán et al. (2013) for a concise description and performance comparison with other NLDR methods in the manipulation of point-set surfaces.

As we have mentioned, a remarkable feature of LLE-based methods is the lack of a clear metric relationship between the low-dimensional embedding and the original data (see Figure 2.7b). In the problems tackled in this work this is not problematic as can be noticed in Figure 2.7c, even when the input point-set describes an elongated surface as that shown in Figure 2.7a. Finally, the resulting Delaunay triangulation from the filtering process is attached to the input point-set surface as depicted in Figure 2.7d.

Mechanical equilibrium in curved manifolds

Mechanical equilibrium in a monolayer of cell centres, on a curved manifold and connected by bar elements is obtained by minimisation of the elastic strain function in equation (2.1), which is written in terms of its spatial coordinates (not the two-dimensional embedding).

Depending on the boundary condition applied on a curved network, and due to the absence of bending elasticity in the network, minimisation of the global elastic strain in equation (2.1) may lead to multiple solutions, i.e. the equilibrium equations in (2.2) yield multiple solutions for $\boldsymbol{X}_{n+1} = \{\boldsymbol{x}_{n+1}^1, \boldsymbol{x}_{n+1}^2, \ldots, \boldsymbol{x}_{n+1}^{N_{nodes}}\}$.

From mechanical point of view, this situation corresponds to the existence of *rigid-body modes* in the network, when multiple positions of nodes correspond to the same set of strain values along the bar elements. Figure 2.8 shows multiple rigid modes of a curved monolayer with the indicated boundary conditions.

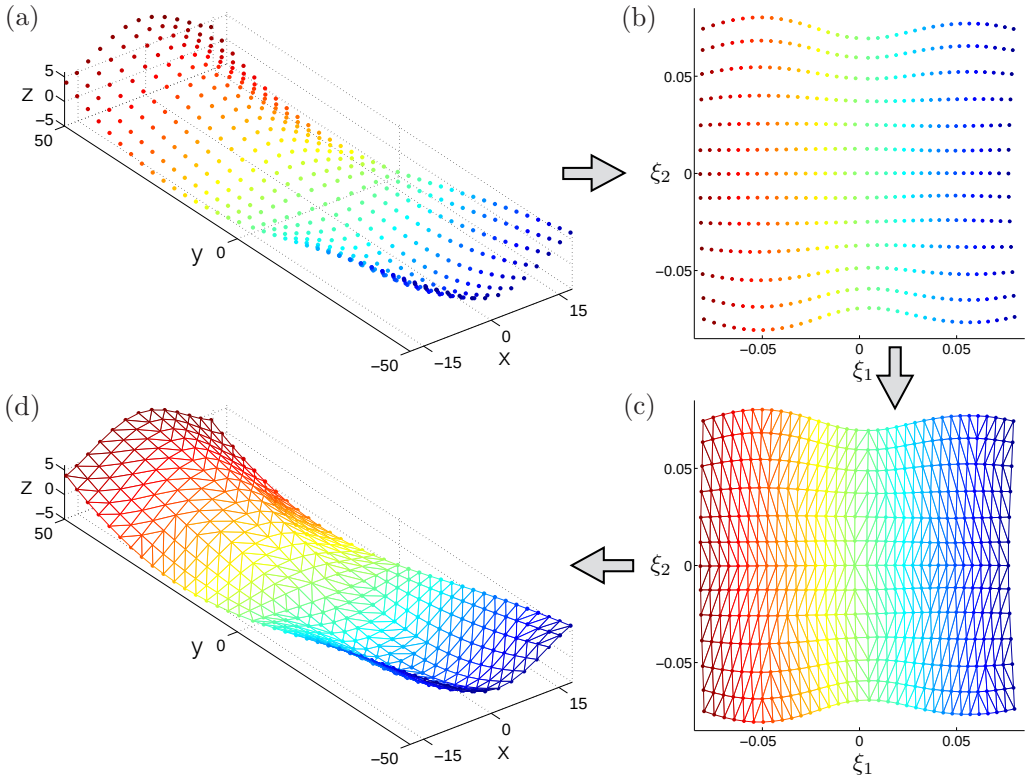

Figure 2.7: (a) Arbitrary point set configuration from a proof of concept example in 3-D. (b) Two-dimensional embedding obtained by using MLLE (Zhang & Wang, 2007)(k-nn=8). The lack of metric related to the input data, that is, different distances between points in the real and mapped domain, and its unit covariance (*mapped* points are distributed on a *squared region*) are apparent from the picture. (c) Two-dimensional embedding nodes and connectivity after applying the filtering described in Section 2.1.2. (d) Three-dimensional initial point set configuration with resulting connectivity. The *colour-map*, which indicates the identifier of each sample of the point set, is provided for visual inspection.

In mathematical terms, this situation occurs when the determinant of the Jacobian of the system (see Appendix E) is close to zero

$$|\mathbf{K}| \simeq 0. \tag{2.9}$$

Therefore, $\mathbf{K}$ has at least one eigenvector $\boldsymbol{\kappa}$ with eigenvalue close to 0 (which we call 0-eigenmodes) and is thus semi-positive-definite.

In order to obtain a positive-definite Jacobian matrix, and thus a system of equations with a unique solution, we here propose a method to penalise solutions $\boldsymbol{u}$ which include eigenvectors $\boldsymbol{\kappa}$, so that the elastic strain function in equation (2.1) will be minimised by a unique $\boldsymbol{u}$. In order to penalise 0-eigenmodes of $\mathbf{K}$, we resort

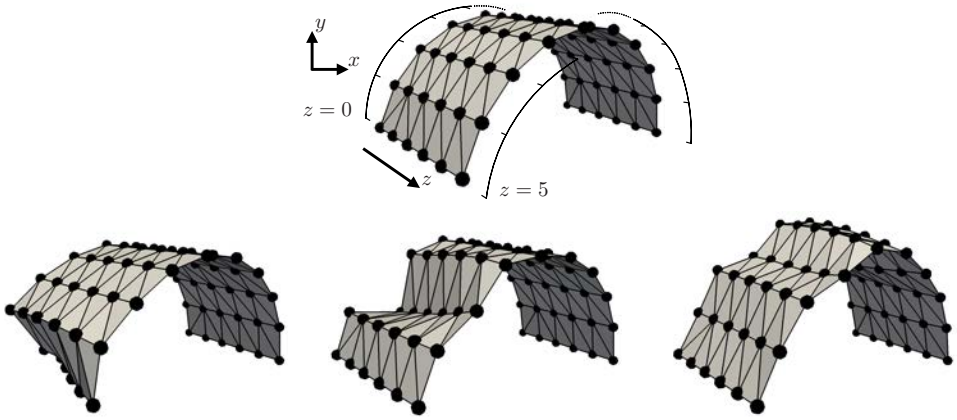

Figure 2.8: Top: monolayer with half-cylinder geometry. The nodes at the plane $z = 0$ are constrained to remain in the plane, while the nodes at the other base of the half-cylinder are constrained to remain in plane $z = 5$. Bottom: multiple rigid modes of the monolayer with half-cylinder geometry.

to minimise the function $W_c(\boldsymbol{x})$ where

$$W_c(\boldsymbol{x}) = W_D(\boldsymbol{x}) + \frac{p_r}{2} \sum_{l=1}^{n_{eig}} \left({\boldsymbol{\kappa}^l}^T \boldsymbol{u}(\boldsymbol{x}) \right)^2, \tag{2.10}$$

where n_{eig} is the number of eigenvectors $\boldsymbol{\kappa}$ whose eigenvalue is smaller than numerical precision δ which can be chosen sufficiently close to 0, and p_r is a penalisation factor.

Minimisation of the strain energy in equation (2.10) will lead to

$$\mathbf{K}_c \boldsymbol{u} = \boldsymbol{g}_c,$$

where

$$\begin{aligned} \mathbf{K}_c &= \mathbf{K} + p_r \sum_{l=1}^{n_{eig}} \boldsymbol{\kappa}^l \otimes {\boldsymbol{\kappa}^l}^T, \\ \boldsymbol{g}_c &= \boldsymbol{g} + p_r \sum_{l=1}^{n_{eig}} \left({\boldsymbol{\kappa}^l}^T \boldsymbol{u} \right) \boldsymbol{\kappa}^l. \end{aligned} \tag{2.11}$$

Clearly, $\mathbf{K}_c$ is positive-definite, and thus the use of the residual in equation (2.11) will have unique solution for $\boldsymbol{g}_c = \mathbf{0}$. Eigenvectors $\boldsymbol{\kappa}$ are obtained by MATLAB function *eig*, which is able to compute the eigenvectors as well as the corresponding eigenvalues of arbitrary square matrices (in our case stiffness matrix $\mathbf{K}$).

2.1.5 Cells boundary

Voronoi diagram

By definition, a Voronoi diagram is a partitioning of the domain into regions based on distance to a predefined set of nodes, and for each node there is a corresponding region consisting of all points closer to that node than to any other. The Voronoi diagram of a set of points is dual to its Delaunay triangulation: each Voronoi face is perpendicular to the connecting line of the Delaunay triangulation, and splits it in half (Barber et al., 1996). In Appendix D the tessellation of the Voronoi diagram from the Delaunay triangulation of the set of points is calculated.

In two-dimensional Euclidean space each Voronoi region forms a convex polygon and in three-dimensional Euclidean space each Vornoi region forms a convex polytop resulting from intersection of planes of perpendicular bisectors.

Application of Voronoi diagram to construct cells boundary

In this section, we resort to standard Voronoi tessellation algorithm of nodes $\boldsymbol{X}_{n+1}$ to represent the cells boundaries. However, the use of standard Voronoi algorithm yields regions with unbounded subdomains closing at infinity. To resolve this issue, a set of off-set nodes were added to the original set of nodes at the boundary of the filtered Delaunay triangulation. In the next points (a), (b) and (c) we will explain how off-set nodes are defined for the two- and three-dimensional nodal configurations.

(a) In two-dimensional nodal configurations, each boundary node $\boldsymbol{x}^i$ is connected to two boundary elements, let us say ij and ik. We define the position of two off-set nodes $\boldsymbol{x}^{i,ij}_{off-set}$ and $\boldsymbol{x}^{i,ik}_{off-set}$ at a constant distance ϵ from node $\boldsymbol{x}^i$ and along the external normal to each element, represented by $\boldsymbol{n}^{ij}$ and $\boldsymbol{n}^{ik}$ (see Figure 2.10c).

$$\begin{aligned} \boldsymbol{x}^{i,ij}_{off-set} &= \boldsymbol{x}^i + \epsilon \boldsymbol{n}^{ij}, \\ \boldsymbol{x}^{i,ik}_{off-set} &= \boldsymbol{x}^i + \epsilon \boldsymbol{n}^{ik}. \end{aligned} \tag{2.12}$$

(b) In three-dimensional nodal configurations representing *cellular aggregates*, each node $\boldsymbol{x}^i$ at the boundary belongs to $n_{\boldsymbol{\mathcal{T}}^i}$ boundary triangles representing $n_{\boldsymbol{\mathcal{T}}^i}$ planes in space. We add $n_{\boldsymbol{\mathcal{T}}^i}$ off-set nodes at distance ϵ to node $\boldsymbol{x}^i$ and along the external normal to each of the $n_{\boldsymbol{\mathcal{T}}^i}$ planes. The set $\boldsymbol{\mathcal{T}}^i$ contains all the triangles $\mathcal{T}^{i,m}$ including node $\boldsymbol{x}^i$ and $m = 1, 2, \ldots, n_{\boldsymbol{\mathcal{T}}^i}$.

$$\boldsymbol{x}^{i,\mathcal{T}^{i,m}}_{off-set} = \boldsymbol{x}^i + \epsilon \boldsymbol{n}^{\mathcal{T}^{i,m}}. \tag{2.13}$$

(c) In three-dimensional nodal configurations representing *cellular monolayers*, off-set nodes are performed at two stages:

(c1) In-plane off-set nodes are added for each node at the boundary of the monolayer (see Figure 2.9). Having elements ij and ik as boundary elements being connected to node $\boldsymbol{x}^i$ and corresponding to triangles $\mathcal{T}^{i,p}$ and $\mathcal{T}^{i,q}$, off-set nodes $\boldsymbol{x}^{i,ij}$ and $\boldsymbol{x}^{i,ik}$ are defined at the constant distance ϵ to node $\boldsymbol{x}^i$ and along external normals $\boldsymbol{n}^{ij,\|\mathcal{T}^{i,p}}$ and $\boldsymbol{n}^{ik,\|\mathcal{T}^{i,q}}$ to the elements ij and ik, respectively. Vectors $\boldsymbol{n}^{ij,\|\mathcal{T}^{i,p}}$ and $\boldsymbol{n}^{ik,\|\mathcal{T}^{i,q}}$ represent normal to element ij in the plane of $\mathcal{T}^{i,p}$, and normal to element ik in the plane of $\mathcal{T}^{i,q}$, respectively.

$$\begin{aligned} \boldsymbol{x}^{i,ij}_{off-set} &= \boldsymbol{x}^i + \epsilon \boldsymbol{n}^{ij,\|\mathcal{T}^{i,p}}, \\ \boldsymbol{x}^{i,ik}_{off-set} &= \boldsymbol{x}^i + \epsilon \boldsymbol{n}^{ik,\|\mathcal{T}^{i,q}}. \end{aligned} \tag{2.14}$$

(c2) A set of out-of-plane off-set nodes are constructed for the whole set of the nodes in the domain and at both sides of the monolayer (see Figure 2.9). So for each node $\boldsymbol{x}^i$, we define $n_{\boldsymbol{\mathcal{T}}^i}$ off-set nodes, at each side of the monolayer, in a distance ϵ from node $\boldsymbol{x}^i$, along the normal $\boldsymbol{n}^{\mathcal{T}^{i,m}}$ where $m = 1, 2, \ldots, n_{\boldsymbol{\mathcal{T}}^i}$.

$$\begin{aligned} \boldsymbol{x}^{i,\mathcal{T}^{i,m},+}_{off-set} &= \boldsymbol{x}^i + \epsilon \boldsymbol{n}^{\mathcal{T}^{i,m}}, \\ \boldsymbol{x}^{i,\mathcal{T}^{i,m},-}_{off-set} &= \boldsymbol{x}^i - \epsilon \boldsymbol{n}^{\mathcal{T}^{i,m}}. \end{aligned} \tag{2.15}$$

The Voronoi tessellation was performed taking into account Delaunay triangulation of the original nodes $\boldsymbol{X}_{n+1}$ and the additional off-set nodes $\boldsymbol{X}_{off-set,n+1}$. The triangulation on the whole three-dimensional domain formed by $\boldsymbol{X}_{n+1}$ and the off-set nodes, $DT(\{\boldsymbol{X}_{n+1}, \boldsymbol{X}_{off-set,n+1}\})$, ensures the formation of bounded regions for the original nodes in the domain. Figure 2.10a illustrates a schematic view of a set of nodes preliminary connected by Delaunay triangulation. Figure 2.10b shows the unbounded regions created by directly applying Voronoi tessellation on a two-dimensional nodal configuration, case (a) above. Figure 2.10c indicates the off-set nodes by yellow circles, while 2.10d shows Delaunay triangulation of combination of original and off-set nodes, as well as Voronoi tessellation of total nodal network, which after removing the unbounded regions and the off-set nodes, results in the final Voronoi regions of the original set of nodes (see Figure 2.10e). The off-set nodes and elements are finally removed.

In summary, the steps followed to form the Voronoi tessellation are:

1. Form off-set layer of nodes. Based on the type of the domain geometry explained previously in items (a), (b) and (c), the position of off-set nodes are computed by either equations (2.12) and (2.13), or equations (2.14) and (2.15).

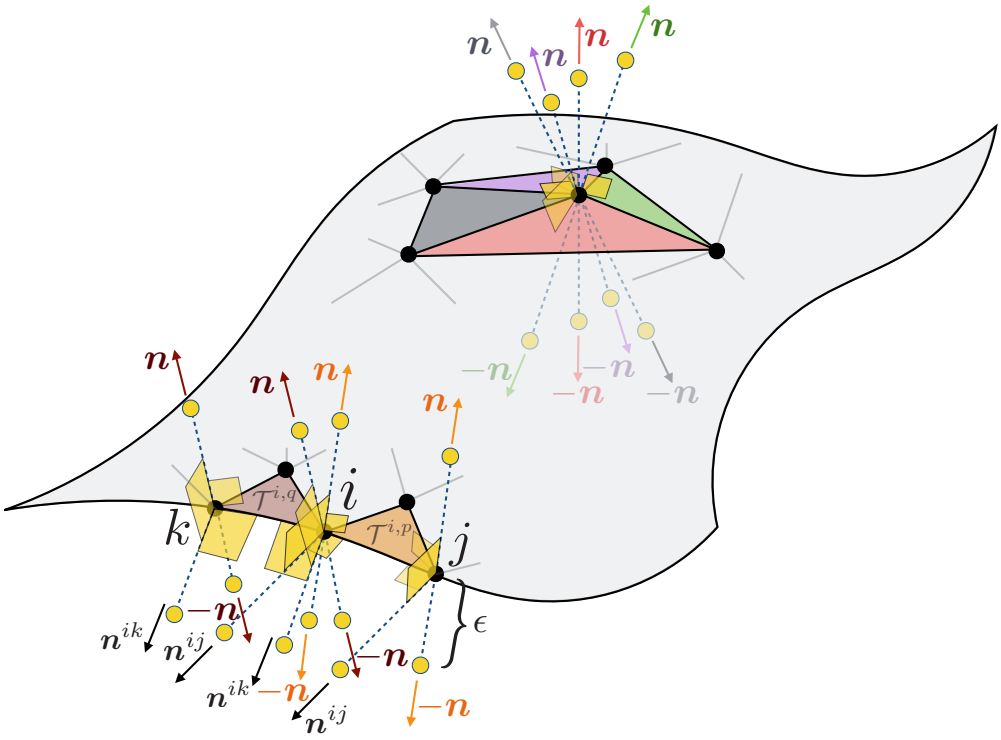

Figure 2.9: Schematic view of a monolayer in 3-D and construction of off-set nodes for the nodes on the middle and the edge of the monolayer. $\boldsymbol{n}$ and $-\boldsymbol{n}$ represent upward and downward normals to the surface of each triangle, following the same colour as the corresponding triangle. $\boldsymbol{n}^{ij}$ and $\boldsymbol{n}^{ik}$ are the normals to the edge elements ij and ik, and in the plane of triangles $\mathcal{T}^{i,p}$ and $\mathcal{T}^{i,q}$, respectively. ϵ represents the distance between each off-set node with its corresponding original node.

The new set of nodes is denoted by $\check{\boldsymbol{X}}_{n+1}$, which includes original nodes $\boldsymbol{X}_{n+1}$ and off-set nodes $\boldsymbol{X}_{off-set,n+1}$ (see Figure 2.10c). In our numerical results we have used $\epsilon = 1$ (the averaged distance between cells), which gives a reasonable cell shape for the cells at the boundary of our examples. We note that, in general, the choice of this parameter should be made dependent on the actual size of the cell, and other values such as the cell-to-cell distance. At this stage, where the cells boundary are not included in the mechanical equilibrium, the value of ϵ does not affect the deformed configurations, but just the aspect ratio of the cell region.

2. Build a new Delaunay triangulation from $\check{\boldsymbol{X}}_{n+1}$, i.e. $\check{\boldsymbol{T}}_{n+1} = DT(\check{\boldsymbol{X}}n{+}1)$, and build Voronoi tessellation of $\check{\boldsymbol{X}}_{n+1}$, that is $\check{\boldsymbol{V}}_{n+1} = Vor(\check{\boldsymbol{X}}_{n+1})$ (see Figure 2.10d).

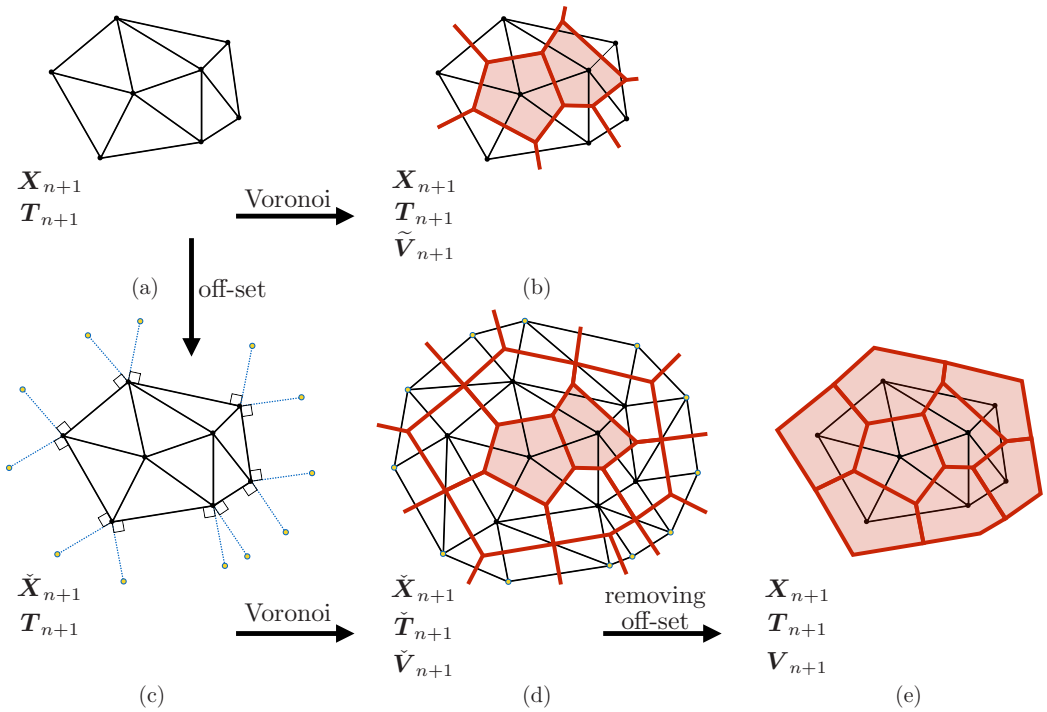

Figure 2.10: Voronoi tessellation. (a) Delaunay triangulation of original set of nodes ($\boldsymbol{T}_{n+1} = DT(\boldsymbol{X}_{n+1})$). (b) Voronoi tessellation of original set of nodes resulting in open regions for the nodes the boundary ($\widetilde{\boldsymbol{V}}_{n+1} = Vor(\boldsymbol{X}_{n+1})$). (c) construct off-set nodes at the boundary of the domain ($\check{\boldsymbol{X}}_{n+1} = \{\boldsymbol{X}_{n+1}, \boldsymbol{X}_{off-set,n+1}\}$). (d) Delaunay triangulation of total nodal configuration ($\check{\boldsymbol{T}}_{n+1} = DT(\check{\boldsymbol{X}}_{n+1})$), and obtain total Voronoi tessellation ($\check{\boldsymbol{V}}_{n+1} = Vor(\check{\boldsymbol{X}}_{n+1})$). (e) Remove off-set nodes and elements and obtain close regions for all original nodes.

3. Remove Voronoi elements coinciding at infinity (see Figure 2.10e) and remove nodes and elements at the off-set layer.

2.2 Hybrid model

So far, in the proposed model, mechanics of the tissue has been described solely by interaction between cell centres defined by the evolution of connecting bar elements. Therefore, mechanical equilibrium was obtained by minimising the elastic potential equation (2.1), while the boundary of the cells was obtained using Voronoi tessellation of the cell centres network, having no role in the mechanics of the system.

In this section, we also assign mechanics on the cells boundary, so that mechanics of the tissue will be described by resorting to a quadratic potential along cell-cell boundaries as well as bar elements between cell centres or nodes. We will also

focus on flat monolayers where the cell deformations along the thickness direction is assumed constant, and thus our description is restricted to the two-dimensional tissue architectures.

While accounting for mechanics on the cells boundary, we keep the cell centres as our primary variables for establishing the equilibrium of the cell system. This will require to compute the contribution of each cell boundary at the cell centres. The boundaries of the cells are defined by a set of *vertices* which are described in terms of the position of cell centres through an interpolation procedure.

2.2.1 Vertex geometry and barycentric tessellation

We assume a tissue with flat monolayer geometry and N_{nodes} nodes, as described in Section 2.1, and a triangulation of the domain in N_{tri} triangles $\mathcal{T}^I$, $I = 1, 2, \ldots, N_{tri}$ and N_D edges. The boundary of the cells are defined by a set of connected vertices $\{\boldsymbol{y}^1, \boldsymbol{y}^2, \ldots, \boldsymbol{y}^{N_{tri}}\}$, which define a tessellation of the tissue domain into N_{cells} cell domains Ω^i, $i = 1, 2, \ldots, N_{cells}$. Note that now $N_{cells} < N_{nodes}$ because N_{cells} does not include the external nodes. We exclude boundary of the cells at the edge of the monolayer, since the mechanical contribution of the boundary of these cells will be negligible in a tissue with high number of cells.

Each triangle $\mathcal{T}^I$ is associated to vertex $\boldsymbol{y}^I$, and each interior node i is surrounded by a number of vertices which is not necessarily constant between time-steps and may vary from cell to cell (see Figure 2.11).

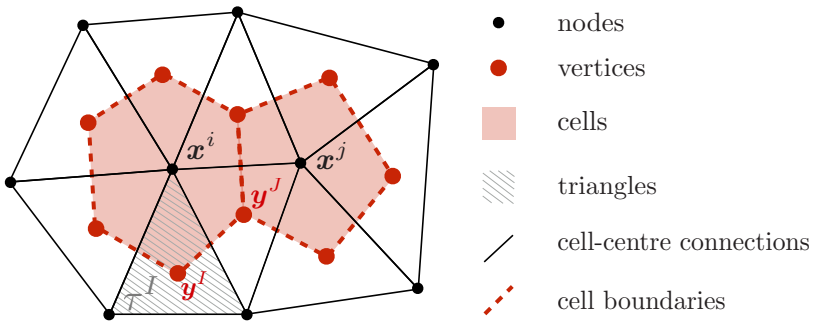

Figure 2.11: Discretisation of tissue into cell centres (nodes, $\boldsymbol{x}^i$) and cells boundaries (vertices, $\boldsymbol{y}^i$). Nodal network and vertex network are outlined with continuous and dashed lines, respectively.

The position of vertex $\boldsymbol{y}^I$ is given by a local parametric coordinate $\boldsymbol{\xi}^I$ in triangle $\mathcal{T}^I$. The kinematic relation between the nodal positions $\boldsymbol{x}^i$ and the vetices is given

by the interpolation

$$\boldsymbol{y}^I = \sum_{i \in \mathcal{T}^I} p^i(\boldsymbol{\xi}^I)\boldsymbol{x}^i. \tag{2.16}$$

Summation in equation (2.16) extends to the three nodes of triangle $\mathcal{T}^I$ where vertex I is located. Function $p^i(\boldsymbol{\xi}^I)$ is the standard finite element interpolation function of node i in triangle $\mathcal{T}^I$ evaluated at coordinate $\boldsymbol{\xi}^I = \{\xi_1^I \ \xi_2^I\}$:

$$\begin{aligned} p^1(\boldsymbol{\xi}^I) &= \xi_1^I \\ p^2(\boldsymbol{\xi}^I) &= \xi_2^I \\ p^3(\boldsymbol{\xi}^I) &= 1 - \xi_1^I - \xi_2^I. \end{aligned}$$

Choice of tessellation

We recall that Voronoi tessellation guarantees that the cells are convex and can be obtained by interpolation of nodes in a triangle following a Delaunay triangulation. However, when the nodal network is mechanically deformed, convexity of the cells can be violated due to length changes of the Delaunay triangulation (see Figure 2.12), and we will avoid using Voronoi tessellation to define cells. For completeness reasons though, appendices D.3 and D.4 show how the values of $\boldsymbol{\xi}^I$ may be computed when the positions of the vertices correspond to Voronoi locations.

Instead, we introduce *barycentric* tessellation of the nodal network to define the position of vertices, which is tantamount to considering that all parameters $\boldsymbol{\xi}^I$ have a constant value $\boldsymbol{\xi}^I = \frac{1}{3}\{1 \ 1\}$. The value guarantees that the vertices are always located at the interior of the triangles, and thus ensures that the tessellation has no cross-overs even if the Delaunay triangulation is deformed (see Figure 2.12). We will eventually allow varying values of $\boldsymbol{\xi}^I$ in Section 2.2.4, where ξ-relaxation is introduced.

2.2.2 Vertex mechanical equilibrium

To provide mechanics on cells boundary, we define an elastic strain function from which the force between any two vertices is derived,

$$\begin{aligned} W_V^{IJ}(\boldsymbol{y}) &= \frac{1}{2}k_V(\varepsilon^{IJ})^2 \\ W_V(\boldsymbol{y}) &= \sum_{IJ=1}^{N_V} W_V^{IJ}(\boldsymbol{y}), \end{aligned} \tag{2.17}$$

with k_V the cell boundary stretching stiffness and $\varepsilon^{IJ} = \frac{l^{IJ} - L^{IJ}}{L^{IJ}}$ is a scalar elastic strain where $l^{IJ} = \left\|\boldsymbol{y}^I - \boldsymbol{y}^J\right\|$ and L^{IJ} are the current and reference lengths of

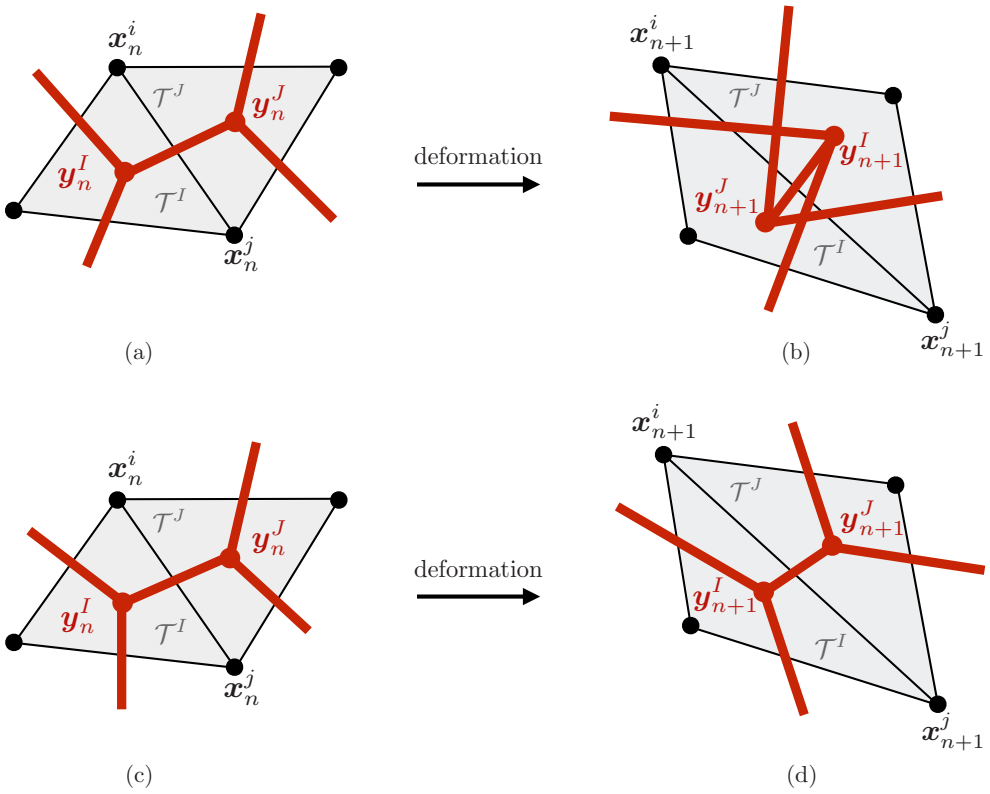

Figure 2.12: Differences between Voronoi (top) and barycentric vertex positions (bottom) for undeformed (left) and deformed networks (right).(a) Nodal network (in black) with Delaunay triangulation and vertex network (in red) with Voronoi tessellation. (b) Deformed nodal network: non-Delaunay triangulation; vertices defined by interpolation of nodes in each triangle, located at the intersection of perpendicular bisectors of each triangle, forming a non-Voronoi vertex network. (c) Nodal network with Delaunay triangulation and vertex network with Barycentric tessellation. (d) Deformed nodal network: non-Delaunay triangulation; vertices defined by interpolation of nodes in each triangle, located at the Barycentres of each triangle, forming a barycentric vertex network.

boundary element IJ. The mechanical strain energy of the system is the sum of the contributions of the nodal and vertex networks,

$$W_D(\boldsymbol{x}) + W_V(\boldsymbol{y}(\boldsymbol{x})).$$

The new nodal positions are found by solving the minimisation problem

$$\boldsymbol{x}^* = \underset{\boldsymbol{x}}{\operatorname{argmin}} \Big(W_D(\boldsymbol{x}) + W_V(\boldsymbol{y}(\boldsymbol{x})) \Big), \tag{2.18}$$

which may be solved in two manners:

1. as a constrained minimisation problem, where nodes $\boldsymbol{x}^i$ and vertices $\boldsymbol{y}^I$ are independent but coupled through the constraint in equation (2.16), that is imposed with Lagrange multipliers.

2. by using the constraint in equation (2.16) in the expression of the objective function (total strain energy) and keeping this relation in the minimisation process.

We choose approach (2) in order to reduce the number of unknowns, and thus the size of the resulting system of equations. In order to deduce the expression of $\frac{\partial W_V}{\partial \boldsymbol{x}^i}$, by using equation (2.17), we define first the vertex tractions as

$$\begin{aligned} \boldsymbol{t}_V^{IJ} &= \frac{\partial W_V^{IJ}}{\partial \boldsymbol{y}^I} = k_V \varepsilon^{IJ} \frac{1}{L^{IJ} l^{IJ}} (\boldsymbol{y}^I - \boldsymbol{y}^J), \\ \boldsymbol{t}_V^{JI} &= \frac{\partial W_V^{IJ}}{\partial \boldsymbol{y}^J} = k_V \varepsilon^{IJ} \frac{1}{L^{IJ} l^{IJ}} (\boldsymbol{y}^J - \boldsymbol{y}^I). \end{aligned} \tag{2.19}$$

Therefore,

$$\boldsymbol{t}_V^{IJ} = \frac{\partial W_V^{IJ}}{\partial \boldsymbol{y}^I} = -\boldsymbol{t}_V^{JI} = -\frac{\partial W_V^{JI}}{\partial \boldsymbol{y}^J}. \tag{2.20}$$

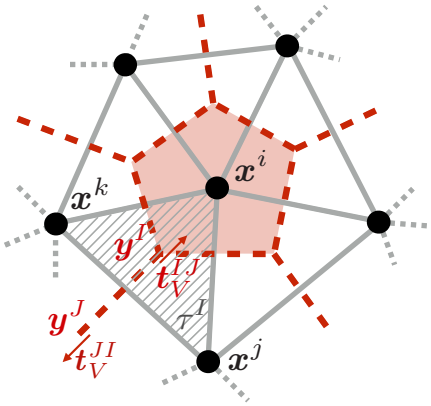

Figure 2.13: Cell boundary (highlighted polygon) corresponding to node i. Barycentric tessellation of $\triangle ijk$ results to triple-junction $\boldsymbol{y}^I$. Vector $\boldsymbol{t}_V^{IJ}$ represents the traction between vertices $\boldsymbol{y}^I$ and $\boldsymbol{y}^J$ along the shared boundary of cells $\boldsymbol{x}^i$ and $\boldsymbol{x}^k$.

The nodal residual due to contributions of the vertex network, denoted by $\boldsymbol{g}_V^i$, may be then computed by using the chain rule and the kinematic relation in equation (2.16),

$$\begin{aligned} \boldsymbol{g}_V^i := \frac{\partial W_V}{\partial \boldsymbol{x}^i} &= \sum_{IJ} \left(\frac{\partial W_V^{IJ}}{\partial \boldsymbol{y}^I} \frac{\partial \boldsymbol{y}^I}{\partial \boldsymbol{x}^i} + \frac{\partial W_V^{IJ}}{\partial \boldsymbol{y}^J} \frac{\partial \boldsymbol{y}^J}{\partial \boldsymbol{x}^i} \right) = \sum_{IJ} \left(\boldsymbol{t}_V^{IJ} p^i(\boldsymbol{\xi}^I) + \boldsymbol{t}_V^{JI} p^i(\boldsymbol{\xi}^J) \right) \\ &= \sum_{I \in B^i} p^i(\boldsymbol{\xi}^I) \sum_{J \in S^I} \boldsymbol{t}_V^{IJ}. \end{aligned} \tag{2.21}$$

In the last expression B^i denotes the set of vertices that form the boundary of cell i, centred on $\boldsymbol{x}^i$, and S^I is the set of vertices connected to vertex I. Note also that the last equality follows from the fact that $p^j(\boldsymbol{\xi}^K)$ vanishes if $K \notin B^j$.

Total mechanical equilibrium is then found by solving the minimisation in equation (2.18), which yields,

$$\sum_{j \in S^i} \boldsymbol{t}_D^{ij} + \sum_{I \in B^i} p^i(\boldsymbol{\xi}^I) \sum_{J \in S^I} \boldsymbol{t}_V^{IJ} = \boldsymbol{0}, \; i = 1, 2, \ldots, N_{nodes}, \tag{2.22}$$

which in terms of the force contributions $\boldsymbol{g}_D^i$ and $\boldsymbol{g}_V^i$ reads

$$\boldsymbol{g}_D^i + \boldsymbol{g}_V^i = \boldsymbol{0}, i = 1, 2, \ldots, N_{nodes}. \tag{2.23}$$

The summation in the second term of equation (2.22) involves the vertex bars that have at least one vertex on the triangles that surround node $\boldsymbol{x}^i$. Figure 2.13 shows schematic view of how the boundary of each cell is defined within the tissue, and the traction vectors $\boldsymbol{t}_V^{IJ}$ and $\boldsymbol{t}_V^{JI}$.

Mechanical equilibrium of the system is obtained at cell centres (nodes) by solving the set of equations in equation (2.22). As mentioned before, since this equation is non-linear with respect to the positions of the nodes, we resort to Newton-Raphson method for its solution. The required linearisation of the terms in equation (2.22) is given in Appendix E.

Note that the second term in equation (2.22) arises due to the kinematic interpolation in equation (2.16). This term represents the nodal contribution of the vertex forces (reactions of the constraints in equation (2.16)), which is proportional to the values of the shape functions $p^i(\boldsymbol{\xi}^I)$. This equation shows the coupling between nodal and vertex equilibrium. When vertex forces exist ($k_V \neq 0$), nodal forces and vertex forces are not necessarily equilibrated at nodes and vertices, respectively, that is, we may have that $\boldsymbol{g}_D^i \neq \boldsymbol{0}$ and $\sum_{J \in S^I} \boldsymbol{t}_V^{IJ} \neq \boldsymbol{0}$. The latter condition is the equilibrium equation usually imposed in purely vertex models (Alt et al., 2017). We will analyse the evolution of these resultants in Chapter 4.

2.2.3 Area constraint

Cell volume invariance under tissue extension is relevant when the size and the number of cells within the tissue is considered as constant. A two-dimensional area constraint will be imposed here by adding the energy term

$$W_A = \frac{\lambda_A}{2} \sum_{m=1}^{N_{cells}} (A^m - A_0^m)^2, \tag{2.24}$$

where λ_A is a penalisation coefficient and A_0^m and A^m are the initial and the current areas of cell m, respectively. Very high values of λ_A may yield an ill-conditioned system of equations, while very low values may exceedingly relax the area constraint. In our numerical examples, we used $\lambda_A \approx 5\, max(k_D, k_V)$, which yielded area variation below 5% in all cases.

The area of cell m can be expressed in terms of its vertices by using Gauss theorem

$$A^m = \int_{\Omega^m} dA = \frac{1}{2} \int_{\partial\Omega^m} \boldsymbol{y} \cdot \boldsymbol{n}\ ds, \tag{2.25}$$

where $\boldsymbol{y}$ is an arbitrary point on the boundary of cell m, ds is the differential segment of the cell boundary and $\boldsymbol{n}$ is the outward normal. Since each cell boundary forms a polygon, we will break the integral over the whole cell boundary into N_m line integrals. Points between vertices I and J can be obtained by using a linear interpolation

$$\boldsymbol{y} = q^I(\alpha)\boldsymbol{y}^I + q^J(\alpha)\boldsymbol{y}^J, \tag{2.26}$$

with $\alpha \in [-1, 1]$ a local coordinate along the cell boundary segment IJ, and $q^I(\alpha) = \frac{1}{2}(1-\alpha)$ and $q^J(\alpha) = \frac{1}{2}(1+\alpha)$ the interpolation functions. By inserting equation (2.26) into equation (2.25) and noting that $ds = l^{IJ} d\alpha/2$, with $l^{IJ} = \left\|\boldsymbol{y}^I - \boldsymbol{y}^J\right\|$, we have

$$A^m = \frac{1}{2} \sum_{IJ \in P^m}^{N_m} \int_{-1}^{1} \sum_{I} q^I(\alpha)\boldsymbol{y}^I \cdot \boldsymbol{n}^{IJ} \frac{l^{IJ}}{2} d\alpha = \frac{1}{2} \sum_{IJ \in P^m}^{N_m} \frac{l^{IJ}}{2} (\boldsymbol{y}^I + \boldsymbol{y}^J) \cdot \boldsymbol{n}^{IJ}, \tag{2.27}$$

where P^m denotes the segments of the polygon that surround node $\boldsymbol{x}^m$ (see Figure 2.13). The expression above can be simplified as

$$A^m = \frac{1}{2} \sum_{IJ \in P^m}^{N_m} (\boldsymbol{y}^I \times \boldsymbol{y}^J).\boldsymbol{e}_z = \frac{1}{2} \sum_{IJ \in P^m}^{N_m} \boldsymbol{y}^I \cdot \mathbf{J}\boldsymbol{y}^J, \tag{2.28}$$

where matrix $\mathbf{J} = \begin{bmatrix} 0 & -1 \\ 1 & 0 \end{bmatrix} = -\mathbf{J}^T$ is such that $(\boldsymbol{y}^I \times \boldsymbol{y}^J) \cdot \boldsymbol{e}_z = \boldsymbol{y}^I \cdot \mathbf{J}\boldsymbol{y}^J$. Finally the total area of the whole set of N_{cells} cells in the tissue, A_T, can be expressed as

$$A_T = \frac{1}{2} \sum_{m=1}^{N_{cells}} \sum_{IJ \in P^m} \boldsymbol{y}^I \cdot \mathbf{J}\boldsymbol{y}^J. \tag{2.29}$$

The expression of the contribution in equation (2.28) is inserted in the energy term in equation (2.24), and appended to the total elastic energy,

$$W = W_D(\boldsymbol{x}) + W_V(\boldsymbol{y}(\boldsymbol{x})) + W_A(\boldsymbol{y}(\boldsymbol{x})),$$

which is minimised with respect to the nodal positions $\boldsymbol{x}^i$. This gives rise to an additional nodal contribution,

$$\boldsymbol{g}_A^i := \frac{\partial W_A}{\partial \boldsymbol{x}^i} = \frac{\lambda_A}{2} \sum_{m \in \bar{S}^i} (A^m - A_0^m) \sum_{IJ \in P^m} \Big(p^i(\boldsymbol{\xi}^I)\boldsymbol{y}^I - p^i(\boldsymbol{\xi}^J)\boldsymbol{y}^J \Big). \tag{2.30}$$

The set $\bar{S}^i$ in the first summation includes the nodes that surround node $\boldsymbol{x}^i$ and also node $\boldsymbol{x}^i$ itself. Since the force vector above is non-linear, the Jacobian must be complemented with additional terms arising from the linearisation of $\boldsymbol{g}_A^i$. These terms are given in Appendix E.

2.2.4 ξ-Relaxation

When the values of $\boldsymbol{\xi}^I$ are kept constant, vertices and cell-centred positions are coupled through the constraint in equation (2.16). As pointed in Section 2.2.2, this constraint has the effect of altering the usual equilibrium conditions in cell-centred and vertex networks (vanishing of the sum of forces at nodes and at vertices, respectively). In fact, in our equilibrium equations in (2.22) and (2.23), the additional force due to $\boldsymbol{g}_V^i$ (which contains the tractions $\boldsymbol{t}_V^{IJ}$) may be regarded as a reaction force stemming from the constraints in equation (2.16). This modified equilibrium may furnish non-smooth and unrealistic deformations at the tissue boundaries, which can then exhibit a zig-zag shape.

In order to avoid these effects, we will disregard the constraint in equation (2.16) for those vertices at the boundary, and relax the value of $\boldsymbol{\xi}^I$, which can attain values different from $\frac{1}{3}\{1\ 1\}$. Those vertices are then allowed to change their relative positions within the corresponding triangle $\mathcal{T}^I$, and may be not necessarily located at the barycentre. In this case, mechanical equilibrium is expressed as a vanishing sum of tractions at the vertex location, as it is customary in vertex models (Okuda et al., 2015; Perrone et al., 2016). In our hybrid model, we interpret the parametric coordinates $\boldsymbol{\xi}$ of those vertices as additional unknowns. The energy terms including the vertices are now made dependent on these extra parametric coordinates, i.e. we write $W_V(\boldsymbol{y}(\boldsymbol{x}, \boldsymbol{\xi}))$ and $W_A(\boldsymbol{y}(\boldsymbol{x}, \boldsymbol{\xi}))$.

When relaxing the constraint, we will further limit the increment of $\boldsymbol{\xi}$ between time-steps, so that their positions are kept not too far from their otherwise interpolated value in order to minimise large discontinuities between discrete time-points on the resulting force contributions. This is achieved by adding to the total energy of the system W and at each time t_{n+1} a term that penalises the variations of $\boldsymbol{\xi}$,

$$W_\xi(\boldsymbol{\xi}) = \frac{\lambda_\xi}{2} \sum_{I \ relaxed} \left\| \boldsymbol{\xi}_{n+1}^I - \boldsymbol{\xi}_n^I \right\|^2. \tag{2.31}$$

By interpreting the factor λ_ξ as a viscous coefficient $\approx \frac{\eta}{\Delta t}$, this additional term is equivalent to a viscous-like effect, since it generates forces proportional to the incremental vertex positions (or vertex velocities).

The extension of the system with additional variables $\boldsymbol{\xi}$ also modifies the minimisation problem in equation (2.18), which now takes the form

$$\{\boldsymbol{x}^*, \boldsymbol{\xi}^*\} = \underset{\boldsymbol{x},\boldsymbol{\xi}}{\operatorname{argmin}}\, W(\boldsymbol{x}, \boldsymbol{\xi}), \tag{2.32}$$

with

$$W(\boldsymbol{x}, \boldsymbol{\xi}) = W_D(\boldsymbol{x}) + W_V(\boldsymbol{y}(\boldsymbol{x}, \boldsymbol{\xi})) + W_A(\boldsymbol{y}(\boldsymbol{x}, \boldsymbol{\xi})) + W_\xi(\boldsymbol{\xi}). \tag{2.33}$$

Equilibrium is now represented by two systems of equations,

$$\boldsymbol{g} := \begin{Bmatrix} \boldsymbol{g}_x \\ \boldsymbol{g}_y \end{Bmatrix} = \boldsymbol{0}, \tag{2.34}$$

with $\boldsymbol{g}_x = \nabla_{\boldsymbol{x}} W(\boldsymbol{x}, \boldsymbol{\xi})$ and $\boldsymbol{g}_y = \nabla_{\boldsymbol{\xi}} W(\boldsymbol{x}, \boldsymbol{\xi})$. Each residual contribution in the total residual $\boldsymbol{g}$ is the sum of different energy contributions in (2.33), so that $\boldsymbol{g} = \boldsymbol{g}_D + \boldsymbol{g}_V + \boldsymbol{g}_A + \boldsymbol{g}_{\boldsymbol{\xi}}$, where each term contains in turn nodal ($\boldsymbol{x}$) and vertex ($\boldsymbol{\xi}$) contributions,

$$\begin{aligned} \boldsymbol{g}_x^i &:= \frac{\partial W(\boldsymbol{x}, \boldsymbol{\xi})}{\partial \boldsymbol{x}^i} = \boldsymbol{g}_D^i + \boldsymbol{g}_V^i + \boldsymbol{g}_A^i + \boldsymbol{g}_{\boldsymbol{\xi}}^i, \\ \boldsymbol{g}_y^I &:= \frac{\partial W(\boldsymbol{x}, \boldsymbol{\xi})}{\partial \boldsymbol{\xi}^i} = \boldsymbol{g}_D^I + \boldsymbol{g}_V^I + \boldsymbol{g}_A^I + \boldsymbol{g}_{\boldsymbol{\xi}}^I. \end{aligned} \tag{2.35}$$

Since the nodal strain energy W_D does not depend on $\boldsymbol{\xi}^I$, and the penalty term W_ξ does not depend on nodal positions $\boldsymbol{x}^i$ (see equations (2.1) and (2.31)), we have that $\boldsymbol{g}_D^I = \boldsymbol{0}$ and $\boldsymbol{g}_\xi^i = \boldsymbol{0}$. The nodal contributions $\boldsymbol{g}_D^i$, $\boldsymbol{g}_V^i$ and $\boldsymbol{g}_A^i$ have been given respectively in equations (2.2), (2.21) and (2.30). The vertex contributions require the computations of

$$\begin{aligned} \nabla_{\boldsymbol{\xi}} W &= \nabla_{\boldsymbol{\xi}} W_V + \nabla_{\boldsymbol{\xi}} W_A + \lambda_\xi(\boldsymbol{\xi}_{n+1} - \boldsymbol{\xi}_n) \\ \frac{\partial \boldsymbol{y}^I}{\partial \boldsymbol{\xi}^I} &= \sum_{\boldsymbol{x}^i \in \mathcal{T}^I} \boldsymbol{x}^i \otimes \nabla p^i(\boldsymbol{\xi}^I), \end{aligned} \tag{2.36}$$

so that we have, also from equations (2.24) and (2.28),

$$\begin{aligned} \boldsymbol{g}_V^I &:= \frac{\partial W_V}{\partial \boldsymbol{\xi}^I} = \sum_{JK} \frac{\partial W_V^{JK}}{\partial \boldsymbol{y}^J} \frac{\partial \boldsymbol{y}^J}{\partial \boldsymbol{\xi}^I} + \frac{\partial W_V^{JK}}{\partial \boldsymbol{y}^K} \frac{\partial \boldsymbol{y}^K}{\partial \boldsymbol{\xi}^I} = \sum_{K \in S^I} \sum_{\boldsymbol{x}^i \in \mathcal{T}^I} (\boldsymbol{t}_V^{IK} \cdot \boldsymbol{x}^i) \nabla p^i(\boldsymbol{\xi}^I) \\ \boldsymbol{g}_A^I &:= \lambda_A \sum_{m=1}^{\bar{N}_{nodes}} (A^m - A_0^m) \frac{\partial A^m}{\partial \boldsymbol{\xi}^I} \\ \boldsymbol{g}_\xi^I &:= \nabla_{\boldsymbol{\xi}} W_\xi = \lambda_\xi(\boldsymbol{\xi}_{n+1}^I - \boldsymbol{\xi}_n^I) \end{aligned} \tag{2.37}$$

with $\frac{\partial \boldsymbol{y}^I}{\partial \boldsymbol{\xi}^I}$ given in equation (2.36), and

$$\frac{\partial A^m}{\partial \boldsymbol{\xi}^I} = \frac{1}{2} \sum_{KL \in P^m} \left(\delta_{KI} \left(\frac{\partial \boldsymbol{y}^K}{\partial \boldsymbol{\xi}^I} \right)^T \mathbf{J} \boldsymbol{y}^L - \delta_{LI} \left(\frac{\partial \boldsymbol{y}^L}{\partial \boldsymbol{\xi}^I} \right)^T \mathbf{J} \boldsymbol{y}^K \right). \tag{2.38}$$

The symbol δ_{KI} above is the Kronecker delta, which is equal to 1 if $K = I$ and 0 otherwise. We note that if we extended ξ-relaxation to the whole tissue, we could recover standard vertex models, that is, a model where the vertices positions are solely determined by their mechanical equilibrium: sum of forces at each vertex equal to zero. In our numerical simulations we have though just applied ξ-relaxation to specific boundaries of the domain.

2.2.5 Remodelling: Equilibrium Preserving Mapping

One of the key features of soft biological tissues is their ability to remodel, that is, to change their neighbouring cells during growth, mobility and morphogenesis. We aim to include this feature in our hybrid model by computing a new connectivity $\boldsymbol{T}_{n+1}$ after each time point t_n and choose a convenient value of the resting length for the new bar elements (Mosaffa et al., 2017). Like in the purely cell-centred model, we resort to the Delaunay triangulation of the nodal network, which guarantees a minimum aspect-ratio of the resulting triangles. We also assume that these optimal aspect ratios will not be exceedingly spoiled during tissue deformation.

The redefinition of the network topology from $\boldsymbol{T}_n$ to $\boldsymbol{T}_{n+1}$ may involve drastic changes in the nodal and vertex equilibrium equations. Furthermore, the resting lengths L^{ij} and L^{IJ} are undefined for the newly created bar elements, and the computation of nodal resting length tensor described in Section 2.2.4 is not suitable in the present case since the number of vertices, in contrast to nodes, is not constant. In order to smooth mechanical transition between time-steps, we will here present an *Equilibrium-Preserving Map* that computes L^{ij} and L^{IJ} by minimising the error of the mechanical equilibrium for the new connectivity. We will consider two approaches: a map that preserves the nodal and vertex equilibrium in a coupled manner (*full-network mapping*), and a map that preserves nodal equilibrium and vertex equilibrium independently (*split-network mapping*). The computational process depicted in Figure 2.6 is now completed with the Equilibrium Preserving Mapping (EPM) as shown in Figure 2.14.

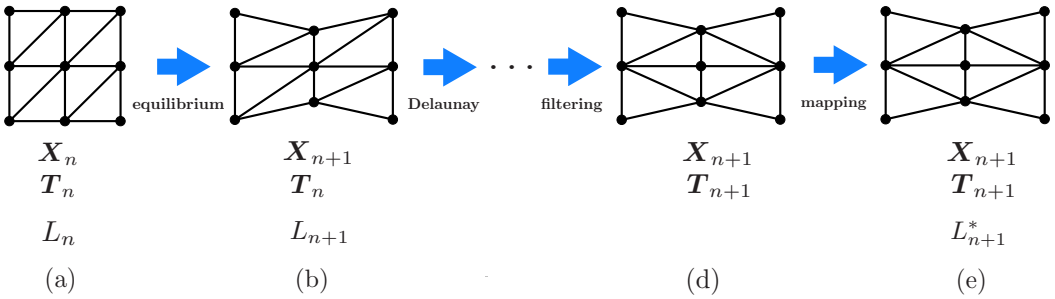

Figure 2.14: Deformation and remodelling process, including the computation of the resting lengths L^*_{n+1} through the Equilibrium-Preserving Map, which maintains the network connectivity and nodal and vertex positions.

Full-network mapping

In this approach, we aim to compute a new set of resting lengths L^{ij} and L^{IJ} that minimise the functional

$$\hat{\pi}_F(L^{ij}, L^{IJ}) = \sum_{i}^{nodes} \left\| \tilde{\boldsymbol{g}}^i_D + \tilde{\boldsymbol{g}}^i_V + \boldsymbol{g}^i_A - \boldsymbol{r}^i \right\|^2 . \tag{2.39}$$

This functional measures the error in the mechanical equilibrium considering all the residual contributions at node i due to the cell centres ($\tilde{\boldsymbol{g}}^i_D$), the vertex network ($\tilde{\boldsymbol{g}}^i_V$) and area constraints ($\boldsymbol{g}^i_A$). The latter is the value obtained from the expression in equation (2.30), while $\boldsymbol{r}^i$ is the total reaction for those nodes that have prescribed displacements. The residual contributions are computed as a function of nodal and vertex tractions as

$$\begin{aligned} \tilde{\boldsymbol{g}}^i_D &= \sum_{j\in S^i} \tilde{\boldsymbol{t}}^{ij}_D = \sum_{j\in S^i} k_D \left(\frac{l^{ij}}{L^{ij}} - 1 \right) \mathbf{e}^{ij} \\ \tilde{\boldsymbol{g}}^i_V &= \sum_{I\in B^i} p^i(\boldsymbol{\xi}^I) \sum_{J\in S^I} \tilde{\boldsymbol{t}}^{IJ}_V = \sum_{I\in B^i} p^i(\boldsymbol{\xi}^I) \sum_{J\in S^I} k_V \left(\frac{l^{IJ}}{L^{IJ}} - 1 \right) \mathbf{e}^{IJ}. \end{aligned} \tag{2.40}$$

Note that $\tilde{\boldsymbol{t}}^{ij}_D$ and $\tilde{\boldsymbol{t}}^{IJ}_V$ are not defined as $\frac{\partial W^{ij}_D}{\partial \boldsymbol{x}^i}$ or $\frac{\partial W^{IJ}_V}{\partial \boldsymbol{y}^I}$, but with a simpler purely elastic law given by $\tilde{\boldsymbol{t}} = k(\frac{l}{L} - 1)\mathbf{e}$, which disregards any rheological law with evolving resting length. These latter laws will be described in Chapter 3.

We emphasise that while computing the new resting lengths and thus the variables L^{ij} and L^{IJ}, the nodal and vertex positions $\boldsymbol{x}^i$ and $\boldsymbol{y}^I$, and also the current lengths l^{ij} and l^{IJ}, are all constant.

The minimisation of $\hat{\pi}_F$ in equation (2.39) gives rise to a non-linear system of equations in terms of the unknowns L^{ij} and L^{IJ}, but that is linear with respect to

the inverse of these quantities. We will denote these inverses by $\theta^{ij} = 1/L^{ij}$ and $\theta^{IJ} = 1/L^{IJ}$. The new functional, denoted by $\pi_F(\theta^{ij}, \theta^{IJ})$, is obtained by inserting this change of variables

$$(\theta^{ij}, \theta^{IJ})^* = \operatorname{argmin} \pi_F(\theta^{ij}, \theta^{IJ}).$$

The optimal variables θ^{ij*} and θ^{IJ*} are found by solving the associated normal equations of this least-squares problem, which after making use of equation (2.40) reads

$$\begin{bmatrix} \mathbf{A}_{DD} & \mathbf{A}_{DV} \\ \mathbf{A}_{DV}^T & \mathbf{A}_{VV} \end{bmatrix} \begin{Bmatrix} \boldsymbol{\theta}_D \\ \boldsymbol{\theta}_V \end{Bmatrix} = \begin{Bmatrix} \boldsymbol{b}_D \\ \boldsymbol{b}_V \end{Bmatrix}, \tag{2.41}$$

with $\boldsymbol{\theta}_D$ and $\boldsymbol{\theta}_V$ vectors containing all the inverses of the resting lengths for the nodal and vertex networks, $1/L^{ij}$ and $1/L^{IJ}$ respectively, and

$$\begin{aligned}
\mathbf{A}_{DD}^{mn,pq} =& k_D^2 l^{mn} \mathbf{e}^{mnT} \left(\sum_{j \in S^m} l^{mj} \mathbf{e}^{mj} \delta_{mj}^{pq} - \sum_{j \in S^n} l^{nj} \mathbf{e}^{nj} \delta_{nj}^{pq} \right) \\
\mathbf{A}_{DV}^{mn,PQ} =& k_D k_V l^{mn} \mathbf{e}^{mnT} \left(\sum_{I \in B^m} p^m(\boldsymbol{\xi}^I) \sum_{J \in S^I} l^{IJ} \mathbf{e}^{IJ} \delta_{IJ}^{PQ} \right. \\
& \left. - \sum_{I \in B^n} p^n(\boldsymbol{\xi}^I) \sum_{J \in S^I} l^{IJ} \mathbf{e}^{IJ} \delta_{IJ}^{PQ} \right) \\
\mathbf{A}_{VV}^{MN,PQ} =& k_V^2 \sum_i^{N_{nodes}} \left(\sum_{I \in B^i} p^i(\boldsymbol{\xi}^I) \sum_{J \in S^I} l^{IJ} \mathbf{e}^{IJ} \delta_{IJ}^{PQ} \right) \\
& \left(\sum_{I \in B^i} p^i(\boldsymbol{\xi}^I) \sum_{J \in S^I} l^{IJ} \mathbf{e}^{IJ} \delta_{IJ}^{MN} \right) \\
\boldsymbol{b}_D^{mn} =& k_D l^{mn} \left(\hat{\boldsymbol{g}}^m - \hat{\boldsymbol{g}}^n \right)^T \mathbf{e}^{mn} \\
\boldsymbol{b}_V^{MN} =& \sum_i^{N_{nodes}} k_V \hat{\boldsymbol{g}}^{iT} \left(\sum_{I \in B^i} p^i(\boldsymbol{\xi}^I) \sum_{J \in S^I} l^{IJ} \mathbf{e}^{IJ} \delta_{IJ}^{MN} \right).
\end{aligned} \tag{2.42}$$

In the equations above, we have defined

$$\begin{aligned}
\hat{\boldsymbol{g}}^i &= k_D \sum_{j \in S^i} l^{ij} \mathbf{e}^{ij} + k_V \sum_{I \in B^i} p^i(\boldsymbol{\xi}^I) \sum_{J \in S^I} \mathbf{e}^{IJ} - \boldsymbol{g}_A^i + \boldsymbol{r}^i \\
\delta_{mj}^{pq} &= \begin{cases} 1, & \text{if } mj = pq, \text{or } mj = qp, \\ 0, & \text{otherwise.} \end{cases} \\
\delta_{IJ}^{PQ} &= \begin{cases} 1, & \text{if } IJ = PQ, \text{or } IJ = QP, \\ 0, & \text{otherwise.} \end{cases}
\end{aligned} \tag{2.43}$$

The uniqueness of the solution of system of equations in equation (2.41), and thus the regularity of the system matrix, is in general not guaranteed, since more than one combination of tractions in equilibrium with the reaction field may be found in some cases. This is algebraically reflected by a large condition number of the system matrix. For this reason, the functional is regularised by adding an extra term,

$$\pi_{F\lambda}(\theta^{ij},\theta^{IJ}) = \pi_F(\theta^{ij},\theta^{IJ}) + \lambda_L \left(\sum_{ij} ||\theta^{ij} - \frac{1}{l^{ij}}||^2 + \sum_{IJ} ||\theta^{IJ} - \frac{1}{l^{IJ}}||^2 \right), \quad (2.44)$$

with l^{ij} and l^{IJ} the current distances between connected nodes and vertices, respectively. This regularisation adds a factor λ_L on the diagonal components and factors λ_L/l^{mn} and λ_L/l^{MN} on $\boldsymbol{b}_D^{mn}$ and $\boldsymbol{b}_V^{MN}$, which ensure that the system will have a unique solution for a sufficiently large value of the regularisation parameter λ_L. In our numerical examples we have used $\lambda_L = 10^{-12}$.

Split-network mapping

The previous approach allows us to find equilibrated tractions with a possible redistribution of forces between the vertex and nodal networks. In some cases though, it is desirable to keep the traction contributions of the two networks split. For this reason, we present an alternative Equilibrium-Preserving Map that aims to compute the resting lengths by considering equilibrium conditions for the nodal and vertex networks independently. This is achieved by minimising the functional

$$\pi_S(\theta^{ij},\theta^{IJ}) = \pi_D(\theta^{ij}) + \pi_V(\theta^{IJ}) \quad (2.45)$$

with

$$\pi_D(\theta^{ij}) = \sum_i^{N_{nodes}} ||\tilde{\boldsymbol{g}}_D^i - \boldsymbol{r}_D^i||^2$$
$$\pi_V(\theta^{IJ}) = \sum_i^{N_{nodes}} ||\tilde{\boldsymbol{g}}_V^i - \boldsymbol{r}_V^i||^2$$

where $\boldsymbol{r}_D^i$ is the contribution from the nodal network on node i before remodelling, and $\boldsymbol{r}_V^i$ is the contribution from the vertex network to node i before remodelling. This contributions are obtained from the residual contributions before remodelling takes place as

$$\begin{aligned} \boldsymbol{r}_D^i &= \boldsymbol{g}_D^i, \\ \boldsymbol{r}_V^i &= \boldsymbol{g}_V^i + \boldsymbol{g}_A^i. \end{aligned} \quad (2.46)$$

Applying the same approach as in Section 2.2.5 to π_F, the minimisation of π_S yields two uncoupled systems of equations,

$$\begin{aligned} \mathbf{A}_{DD}\boldsymbol{\theta}_D &= \boldsymbol{b}'_D \\ \mathbf{A}_{VV}\boldsymbol{\theta}_V &= \boldsymbol{b}'_V. \end{aligned} \tag{2.47}$$

Matrices $\mathbf{A}_{DD}$ and $\mathbf{A}_{VV}$ are those written in equation (2.42), while the right-hand sides are now given by

$$\begin{aligned} {\boldsymbol{b}'_D}^{mn} =& k_D l^{mn} \left(\hat{\boldsymbol{g}}_D^m - \hat{\boldsymbol{g}}_D^n\right)^T \mathbf{e}^{mn} \\ {\boldsymbol{b}'_V}^{MN} =& \sum_i^{N_{nodes}} k_V \hat{\boldsymbol{g}}_V^{i\,T} \left(\sum_{I \in B^i} p^i(\boldsymbol{\xi}^I) \sum_{J \in S^I} l^{IJ} \mathbf{e}^{IJ} \delta_{IJ}^{MN} \right) \end{aligned}$$

with

$$\begin{aligned} \hat{\boldsymbol{g}}_D^i &= k_D \sum_{j \in S^i} l^{ij} \mathbf{e}^{ij} + \boldsymbol{r}_D^i, \\ \hat{\boldsymbol{g}}_V^i &= k_V \sum_{I \in B^i} p^i(\boldsymbol{\xi}^I) \sum_{J \in S^I} \mathbf{e}^{IJ} + \boldsymbol{r}_V^i. \end{aligned}$$

Like in the previous section, a regularisation term, equal to the one used in equation (2.44) is added to the functional π_S in order to ensure the regularity and uniqueness of the solution, with the same value of the regularisation parameter $\lambda_L = 10^{-12}$.

The split-network approach is in fact relevant when the stresses in the nodal and vertex networks follow different patterns, and it is necessary to maintain this difference between the networks, such as wound healing, where the stresses around the wound ring are significantly higher. Preserving stress residuals independently at each network guarantees the stress contrast. The full-network approach on the other hand, spoils this contrast and may transfer some of the stresses on the wound ring to the nodal network. The numerical example in Chapter 4 illustrates this fact.

Chapter 3

Rheological model

Many phenomena at cellular level deal with variations in the elastic and viscous properties of biological matter. A model should consider these features within the inhomogeneous structure of biological tissue. As a result, a cell can be deduced as a combination of viscous and elastic elements.

Within the next sections we provide description of some classical rheological models traditionally applied to describe live soft matter, as well as some recently developed models. Since rheological properties of tissues are modelled through a system of truss elements, we restrict our description to one-dimensional rheology. For instance, a spring and a dash-pot element will display the elastic and viscous components along the truss elements, respectively, which is implemented as assigning the resulting stresses along the direction of the bar element.

3.1 Elastic model

When a material behaves elastically, the stress can be calculated directly from the strain, due to non-existence of path or/and time dependency. When the stress is released, the strain will become zero, so there is no permanent deformation at zero stress. All stored strain energy is released and there is no energy dissipation.

As mentioned above, the discrete material behaviour along a one-dimensional truss element is modelled as a spring. The behaviour here is modelled with a linear relation between the stress σ and the elongation factor or strain ε,

$$\sigma = k\,\varepsilon, \tag{3.1}$$

where k is the stiffness coefficient. The strain in (3.1) is defined by $\varepsilon = \frac{l-L_0}{L_0}$, where L_0 is the element reference length.

3.2 Kelvin-Voigt and Maxwell models

Appropriate choice and combination of a spring stiffness (elastic component) and a dash-pot viscosity, can describe the mechanical characteristics of many materials. There are two major rheological viewpoints towards modelling of visco-elasticity of materials: *Kelvin-Voigt* and *Maxwell* models. In the Kelvin-Voigt model (see Figure 3.1a), the two features contribute in parallel, i.e. the stress is additive and the strain is equal,

$$\begin{aligned} \sigma &= \sigma^e + \sigma^v, \\ \varepsilon &= \varepsilon^e = \varepsilon^v. \end{aligned} \tag{3.2}$$

Therefore, by having $\sigma^e = k\varepsilon^e$ and $\sigma^v = \eta\varepsilon^v$ the total stress reads,

$$\sigma = k\,\varepsilon + \eta\,\dot{\varepsilon}\,, \tag{3.3}$$

where k and η are the material stiffness and viscosity, respectively. However, in Maxwell model (see Figure 3.1b), the contribution of the two features is in series which implies additive strains and equal stresses for each element,

$$\begin{aligned} \sigma &= \sigma^e = \sigma^v, \\ \varepsilon &= \varepsilon^e + \varepsilon^v, \end{aligned} \tag{3.4}$$

and the total stress reads as,

$$\sigma = k\,\varepsilon = \eta\,\dot{\varepsilon}\,. \tag{3.5}$$

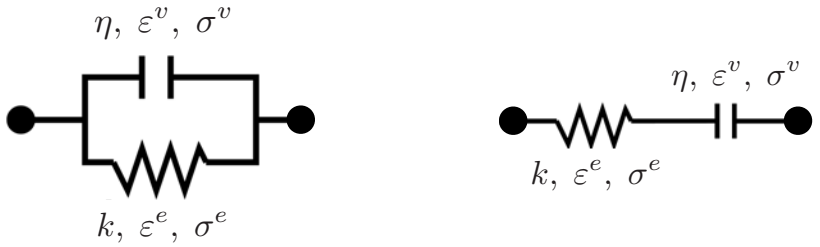

Figure 3.1: Representation of (a) Kelvin-Voigt model and (b) Maxwell model.

Kelvin-Voigt model is best suited for modelling creep (strain relaxation) in a stress controlled test, while Maxwell model is suitable to reproduce stress relaxation in a strain controlled test. The generalised Maxwell model (see Figure 3.2) is a combination of the two models which can be applied to both cases above and is able to fit general visco-elastic materials (Findely et al., 1989). These models can be generalised to non-linear regimes and to continua (Holpzafel, 2007).

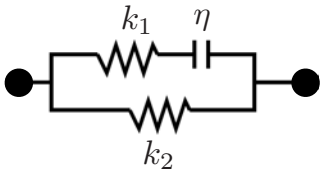

Figure 3.2: Generalised Maxwell model

3.2.1 Implementation of Kelvin-Voigt model

Kelvin-Voigt model is implemented by using double-branched bar elements, where a fully elastic element functions in parallel with a fully viscous one.

3.2.2 Implementation of Maxwell model

By taking the first derivative of ε in equation (3.4), with respect to time t we have,

$$\dot{\varepsilon} = \dot{\varepsilon}^e + \dot{\varepsilon}^v. \tag{3.6}$$

By combining equations (3.4), (3.5) and (3.12), we obtain the evolution law below,

$$\dot{\sigma} = k\left(\dot{\varepsilon} - \frac{\sigma}{\eta}\right). \tag{3.7}$$

Here, to obtain the current stress σ_{n+1} we resort to a time-discretisation method based on θ scheme where $\sigma(t_n) \approx \sigma_{n+\theta} = (1-\theta)\sigma_n + (\theta)\sigma_{n+1}$ (Wilson, 1968). Then, by assuming $\dot{\sigma} \approx \frac{\Delta\sigma}{\Delta t}$ where $\Delta(\bullet) = (\bullet)_{n+1} - (\bullet)_n$ we have,

$$\sigma_{n+1} = \left(1 + \frac{k\theta\Delta t}{\eta}\right)^{-1}\left(k\Delta\varepsilon + \left(1 + \frac{k\Delta t(\theta-1)}{\eta}\right)\sigma_n\right). \tag{3.8}$$

3.3 Active model

Cell viscosity is not solely due to the fluid part of the cytoplasm (water) but also due to cell activity (Besser et al., 2011; Fung, 1993; MacKintosh & Levine, 2008; Mizuno et al., 2007). However, when retrieving characteristic viscous coefficients of cells, there is a wide spectrum of values that have been employed, which range from $\eta = 4.2 \times 10^{-3}$Pa s, according to the Brownian motion of molecules in embryonic cells of *Drosophila melanogaster* (Gregor et al., 2005), to $\eta = 10^5$Pa s for cells at its wing imaginal disc, a value deduced from relaxation experiments (Bittig et al., 2008; Forgacs et al., 1998). While the former values are close to water viscosity ($\eta = 8.9 \times 10^{-4}$Pa s), the later coefficient is in fact similar to the viscosity of olive oil or ketchup-like materials. Hence, in order to shed light into the mechanisms that

cause the cellular response of the cell, it seems necessary to bridge the measured viscosity and the cellular biomolecular processes. For this end, we describe next a simple phenomenologically based model that considers the observed cell viscosity as a combination of the passive cell network (Gittes & MacKintosh, 1998; Janmey et al., 1994; MacKintosh et al., 1995) and also a consequence of active response of the motor proteins (MacKintosh & Levine, 2008; Mizuno et al., 2007; Morozof & Pisman, 2010).

3.3.1 Linear active model

When a set of cross-linked actin filaments in the cytoskeleton is subjected to a macroscopic strain, it stretches as a result of two combined phenomena: (i) a reversible (elastic) deformation, and (ii) a non-reversible remodelling and lengthening. The latter is phenomenologically explained as the remodelling of the cross-links and a (de-)polymerisation process of the filaments. Figure 3.3 illustrates schematically these two combined effects for a pair of cross-linked polymers under a stretch process. We model these effects by allowing the resting length to vary, and becoming an additional variable. We hypothesise that the current relative rate of resting length L of the combined filaments, is proportional to the elastic strain (Muñoz & Albo, 2013), that is

$$\frac{\dot{L}}{L} = \gamma \varepsilon^e, \tag{3.9}$$

where ε^e is the elastic strain and γ is a material parameter so-called *remodelling rate*. It has been shown that this law can mimic the apparent visco-elastic behaviour of cells (Muñoz & Albo, 2013), and that can be used to simulate tissue fluidisation (Asadipour et al., 2016) or cell cortex response (Clément et al., 2017; Doubrovinski et al., 2017). Note that due to the non-linear dependence of the used strain measure on the nodal or vertex positions, the viscous law includes geometrical non-linearities. Material non-linear viscous effects have been considered for instance in the context of tissue fluidisation (Asadipour et al., 2016), or in stress relaxation (Khalilgharibi et al., 2017). By hypothesising more sophisticated laws than the one in equation (3.9), the other non-linear effects can be simulated, as it will be developed in the next section.

The evolution law in equation (3.9) is combined with a purely linear elastic constitutive law in equation (2.1). This is implemented by discretising the differential equation in (3.9) using the θ-weighted scheme presented in Section 3.2,

$$L_{n+1} - L_n = \Delta t \gamma (l_{n+\theta} - L_{n+\theta}). \tag{3.10}$$

In our numerical tests we have used the value $\theta = 0.5$, which guarantees stability and second-order accuracy in the linear regime. The discretisation in equation

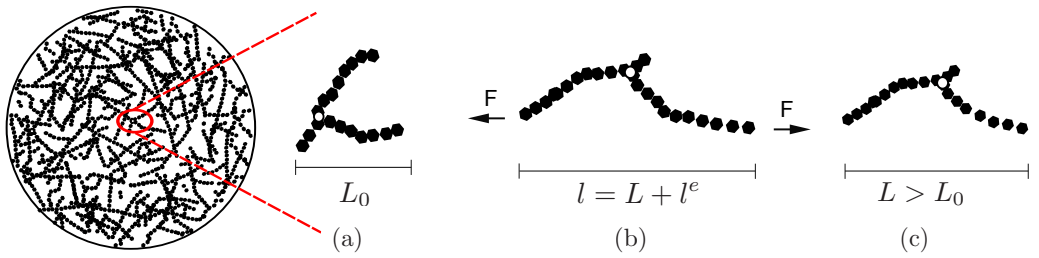

Figure 3.3: Left: Schematic of network of actin filaments connected by flexible cross-links. Right: Schematic of strain induced changes in the resting length L of a reduced system with two filaments and a cross-link (*white circle*), (a) initial configuration with resting length equal to L_0, (b) configuration under an applied load, and (c) new unstrained configuration with modified resting length $L > L_0$.

(3.10) allows us to write the dependence of the resting length on the current length variations as

$$\frac{\partial L}{\partial l} = \frac{\theta \Delta t \gamma}{1 + \theta \Delta t \gamma}. \tag{3.11}$$

Due to the varying resting length, the nodal and vertex tractions along elements ij and IJ, denoted by $\boldsymbol{t}_D^{ij}$ and $\boldsymbol{t}_V^{IJ}$, respectively, and given in equations (2.3) and (2.19), need to be rewritten taking into account the term in equation (3.11). Therefore, with the help of the following derivation,

$$\frac{\partial \varepsilon^{ij}}{\partial \boldsymbol{x}^i} = \frac{1}{L}\left(1 - \frac{1}{L}\frac{\partial L}{\partial l}\right)\mathbf{e}^{ij} \quad , \quad \frac{\partial \varepsilon^{IJ}}{\partial \boldsymbol{y}^I} = \frac{1}{L}\left(1 - \frac{1}{L}\frac{\partial L}{\partial l}\right)\mathbf{e}^{IJ}, \tag{3.12}$$

with

$$\mathbf{e}^{ij} = -\mathbf{e}^{ji} = \frac{\boldsymbol{x}^i - \boldsymbol{x}^j}{\|\boldsymbol{x}^i - \boldsymbol{x}^j\|} \quad , \quad \mathbf{e}^{IJ} = -\mathbf{e}^{JI} = \frac{\boldsymbol{y}^I - \boldsymbol{y}^J}{\|\boldsymbol{y}^I - \boldsymbol{y}^J\|}, \tag{3.13}$$

the traction forces in equations (2.3) and (2.19), then read respectively as,

$$\begin{aligned} \boldsymbol{t}_D^{ij} &= \frac{\partial W_D^{ij}}{\partial \boldsymbol{x}^i} = k_D \frac{\varepsilon^{ij}}{L^{ij} l^{ij}}\left(1 - \frac{\partial L^{ij}}{\partial l^{ij}}\frac{l^{ij}}{L^{ij}}\right)\mathbf{e}^{ij}, \\ \boldsymbol{t}_V^{IJ} &= \frac{\partial W_V^{IJ}}{\partial \boldsymbol{y}^I} = k_V \frac{\varepsilon^{IJ}}{L^{IJ} l^{IJ}}\left(1 - \frac{\partial L^{IJ}}{\partial l^{IJ}}\frac{l^{IJ}}{L^{IJ}}\right)\mathbf{e}^{IJ}, \end{aligned} \tag{3.14}$$

where the term $\partial L/\partial l$ is given in equation (3.11). The elemental active length L^{ij} can be statically condensed (Muñoz et al., 2013), so that only displacement degrees of freedom are globally solved.

Contractility

In order to include the inherent contractility that cells exert (Salbreux et al., 2012), the evolution law in (3.9) is modified as

$$\frac{\dot{L}}{L} = \gamma(\varepsilon^e - \varepsilon^c), \tag{3.15}$$

with ε^c a contractility parameter. This modification aims to attain a homoeostatic strain equal to ε^c, at which no further modifications of the resting length take place.

The ordinary differential equation (ODE) in (3.15) is employed for the bar elements of the nodal and vertex networks, and is solved together with the non-linear equations in (2.32). In fact, the evolution law is taken into account by first discretisation in time of the ODE in (3.15) with the θ-weighted scheme, presented in Section 3.2. By using the strain definition $\varepsilon^e = (l - L)/L$, the discretisation of (3.15) yields,

$$L_{n+1} - L_n = \Delta t\gamma(l_{n+\theta} - L_{n+\theta} - \varepsilon^c L_{n+\theta}). \tag{3.16}$$

By inserting the θ-wighted scheme, the discretisation in (3.16) yields

$$\frac{\partial L}{\partial l} = \frac{\theta\Delta t\gamma}{1 + \theta\Delta t\gamma(1 + \varepsilon^c)}, \tag{3.17}$$

which replaces the expression in equation (3.14).

3.3.2 Non-linear active model (power law)

Experimental tests on stress relaxation in monolayers show a trend of the stresses according to Khalilgharibi et al. (2017)

$$\sigma = At^{-\alpha} + B. \tag{3.18}$$

This contradicts the standard Maxwell model using linear stress and viscous constitutive laws introduced in (3.5), which as deduced next, exhibit a purely exponential evolution. The kinematic condition, where the total applied strain remains constant, $\dot{\varepsilon} = 0$, allows us to write equation (3.12) as

$$\dot{\varepsilon}^e + \dot{\varepsilon}^v = 0. \tag{3.19}$$

In this condition, the solution of σ in equation (3.7) has the form

$$\sigma = \sigma_0 e^{-tk/\eta}. \tag{3.20}$$

To conciliate the experimental evolution of the stress σ, introduced above, with a linear elastic law where

$$\sigma = k\left(\frac{l}{L} - 1\right), \tag{3.21}$$

we account for a variable resting length L, and a constant current length l as it is implied by kinematic condition (3.19). Combining the experimental trend introduced in equation (3.18) with linear elastic law in (3.21), the evolution of resting length L reads as

$$L = \frac{kl}{At^{-t} + B + k}. \tag{3.22}$$

The time derivative $\dot{L}$ may be expressed in terms of L, yielding

$$\begin{aligned} \dot{L} = \frac{\alpha L^2}{kl} A t^{-\alpha-1} &= \frac{\alpha L^2}{kl} A \left[\frac{1}{A}\left(\frac{kl}{L} - B - k\right)\right]^{1+1/\alpha} \\ &= \alpha \frac{L^2}{l}\left(\frac{k}{A}\right)^{1/\alpha}\left(\varepsilon - \frac{B}{k}\right)^{1+1/\alpha}. \end{aligned} \tag{3.23}$$

This evolution law may be written as

$$\frac{\dot{L}}{L} = \frac{\gamma}{\varepsilon + 1}(\varepsilon - \varepsilon^c)^n, \tag{3.24}$$

where $\varepsilon^c = B/k$ is the cell contractility (we have that $\dot{L} = 0$ when $\varepsilon = \varepsilon^c$), $\gamma = \alpha(k/A)^{1/\alpha}$ is a remodelling rate, and $n = 1 + \frac{1}{\alpha}$. This law is a non-linear extension of the previous evolution law in (3.15), which is developed here in order to simulate more sophisticated relaxation evolution of monolayers. In Chapter 4 we will numerically verify that the resulting evolution law matches the observed power law.

Chapter 4

Numerical Results

The methodology introduced in Chapters 2 and 3 has been implemented in *MATLAB R2013a* and *MATLAB R2015b*. For illustrative two- and three-dimensional problems, the post-processing has been completed using *ParaView 4.1.0*.

4.1 Extension of cell-centred networks

In this section we focus on simulation of extension of two- and three-dimensional cellular aggregates. Since non-linear mechanical response is relevant in soft tissues, we will provide a comparison of mechanical response, between tissues with and without dynamic topology. We will then show how topological changes can trigger non-linear response in tissues modelled as a cell-centre nodal network with solely elastic elements.

Two-dimensional network

A network of 45 nodes configured in two-dimensional space and forming an initially uniform rectangle (see Figure 4.1a), is subjected to a longitudinal traction by exerting prescribed forces along the long axis of the rectangle, following a step function spanned 80 time-steps.

The coordinates of the nodes at one end of the rectangle have been fixed, experiencing a reaction force against the prescribed force exerted uniformly to the nodes on the other parallel end.

Three-dimensional network

A network of 225 nodes configured in three-dimensional space and initially forming a uniform cube (see Figure 4.1c), undergoes a purely elastic longitudinal traction by exerting a prescribed force along the long axis of the cube, following a step function spanned 80 time-steps.

Like in the two-dimensional case, the coordinates of the nodes at one end of the cube have been fixed, experiencing a reaction force against the prescribed force exerted uniformly to the nodes on the other parallel end.

At each time-step, Newton-Raphson method has been employed to find the new equilibrated coordinates of the nodes. Then, the connectivity of the nodes has been updated by a Delaunay triangulation function. Finally, for visualisation purposes only, the Voronoi tessellation function has been employed to update the Voronoi vertices, at each time-step. The software package Qhull (Barber et al., 1996) has been used to generate the connectivity of Voronoi cells in the three-dimensional network. The correction methods explained in Sections 2.1.2 and 2.1.5, for eliminating unrealistic Delaunay vertices on concave edges and building closed Voronoi cells, have been also exploited at each time-step.

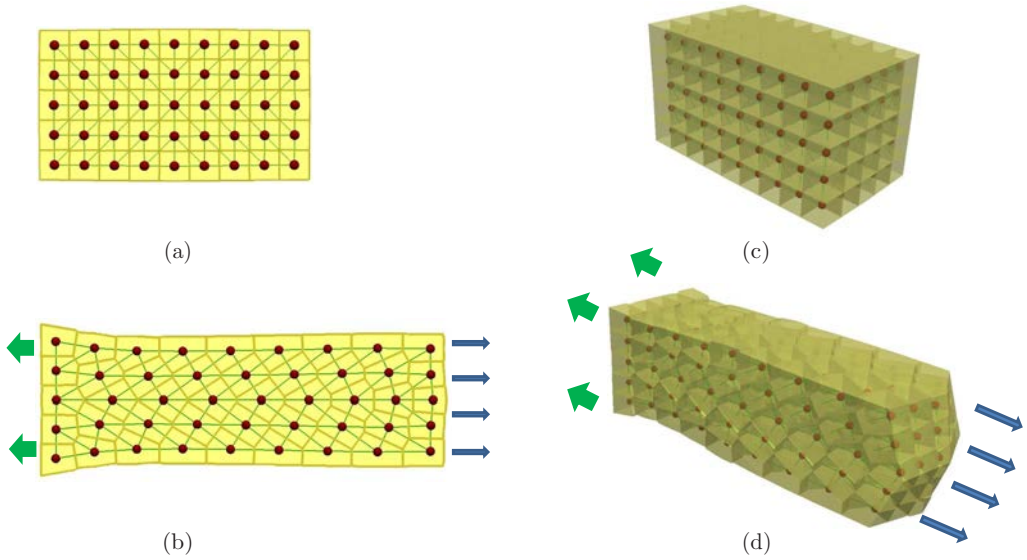

Figure 4.1: Graphical representation of (a) initial configuration of sample model in 2-D, (b) final configuration (equilibrated) of two-dimensional sample under longitudinal traction, (c) initial configuration of sample model in 3-D, and (d) final configuration (equilibrated) of three-dimensional sample model under longitudinal traction– Thin flashes represent uniform load on all nodes at the corresponding face of the networks, while thick flashes represent the reaction force on the nodes on the opposite end.

Figure 4.2a and 4.2b show plots of average displacement of those nodes experiencing a linearly increasing external force for two networks of 45 nodes in 2-D and 225 nodes in 3-D, and over a number of time-steps $n = 80$, under two conditions: 1) dynamic topology (connectivities updated by Delaunay triangulation at each time-step) and 2) frozen topology where initial connectivity is preserved throughout the

analysis.

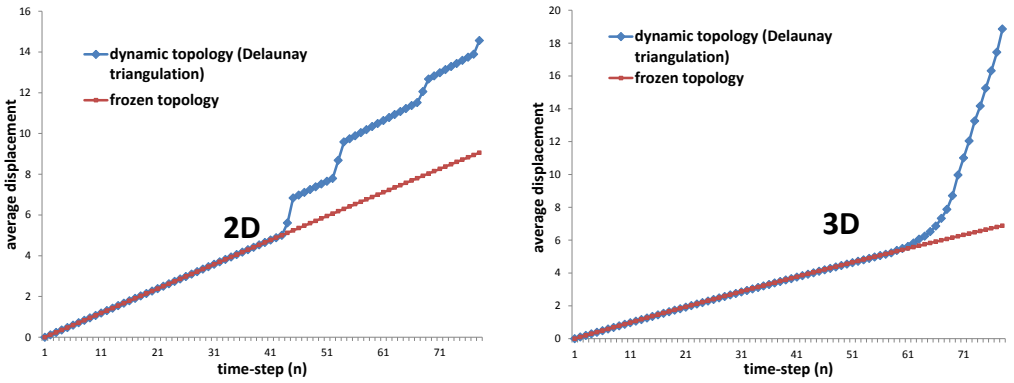

(a) (b)

Figure 4.2: Representation of average displacement of nodes under a linearly increasing external load over 80 time-steps, under two conditions: dynamic topology and frozen topology for (a) a two-dimensional network of 45 nodes, and (b) a three-dimensional network of 225 nodes.

As it can be observed, constant topology exhibits a linear elastic behaviour to material with elastic connecting elements. Even if the model can handle geometrical non-linearities, such as stiffening due to alignment of the bars, these are absent due to the reduced amount of strain.

Although the bar elements are assigned a purely elastic behaviour, the update in the Delaunay triangulation causes the whole material to behave non-linearly. This non-linear response here is obtained through a "refreshing" strategy, which implies the strain along new elements, defined by Delaunay triangulation at each time-step, is refreshed to 0. Such behaviour can be compared to other formulations in continua that use a constant mesh with a non-linear constitutive law.

In the plots above, it is also worth noticing the different responses of two- and three-dimensional simulated networks throughout the dynamic topology. While the former shows a flipping trend, the later grows smoothly. This behaviour is due to different number of degrees of freedom in either of systems, provided by different number of nodes as well as different number of degrees of freedom per node in 2-D compared to in 3-D. The discontinuous effect vanishes for aggregates with much higher number of nodes, where the connectivity changes vary more progressively, and each modification of the topology has a minor effect on the global network.

4.2 Active rheology in flat monolayers

In order to test the effects of the connectivity changes and also the active rheological law, respectively described in Sections 2.1.2 and 3.3.1, we have simulated the stretching of a flat square monolayer with dimensions $(L_x, L_y) = (11, 10)$, and subjected to an increasing displacement u_x, $0 \leq u_x \leq 20$ at the boundary $X = 11$, with the boundary $X = 0$ fixed (see Figure 4.3).

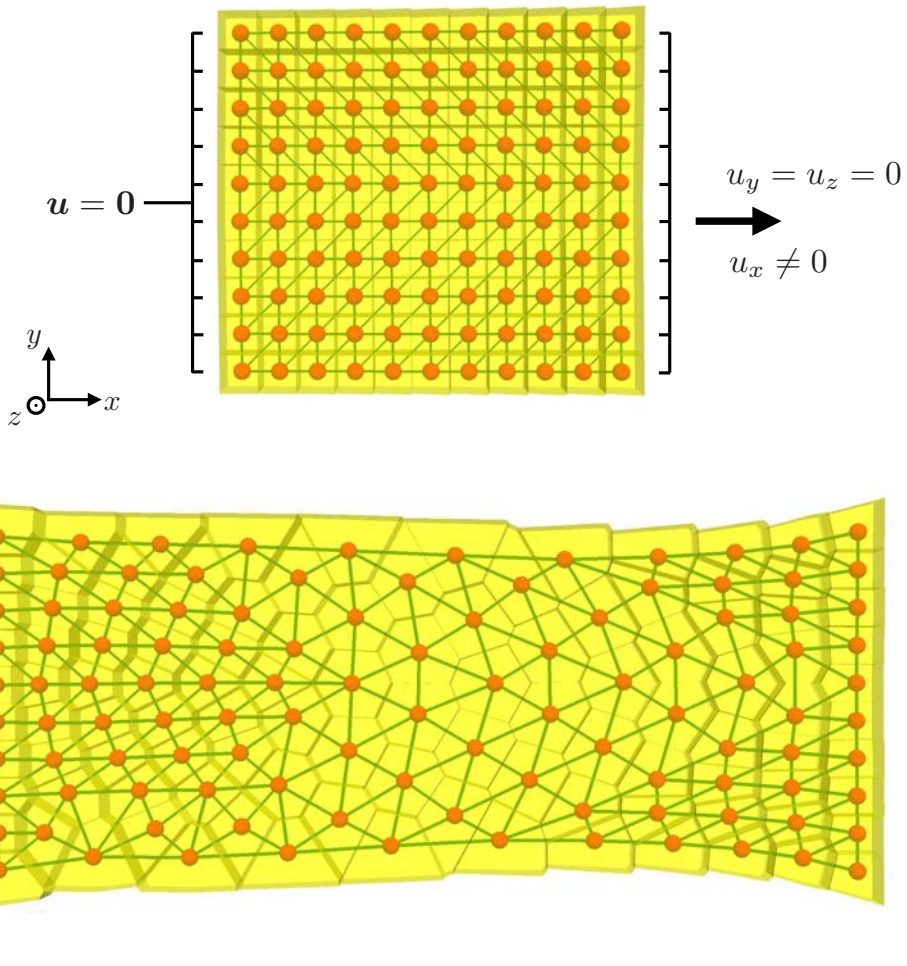

Figure 4.3: Example of flat monolayer. *Top*: initial geometry; *Bottom*: deformed geometry.

We have analysed the following two material models:

M1: $\gamma = 0$; Pure elastic material with $k = 0.8$.

M2: $\gamma = 0.01$; Elastic material with $k = 0.8$ and evolving resting length L.

We have measured the sum of all the reactions along direction x for the nodes that are initially at the boundary $X = 11$. The evolution of this sum, denoted by R_{TOT}, is plotted in Figures 4.4a-b for the two material choices M1 and M2. We have also tested the effect of allowing cell-cell remodelling. When remodelling is allowed, we have in turn implemented two possible regimes: with stress relaxation and with no stress relaxation, which corresponds to update the resting length of the new elements according to the expressions in Table 4.1.

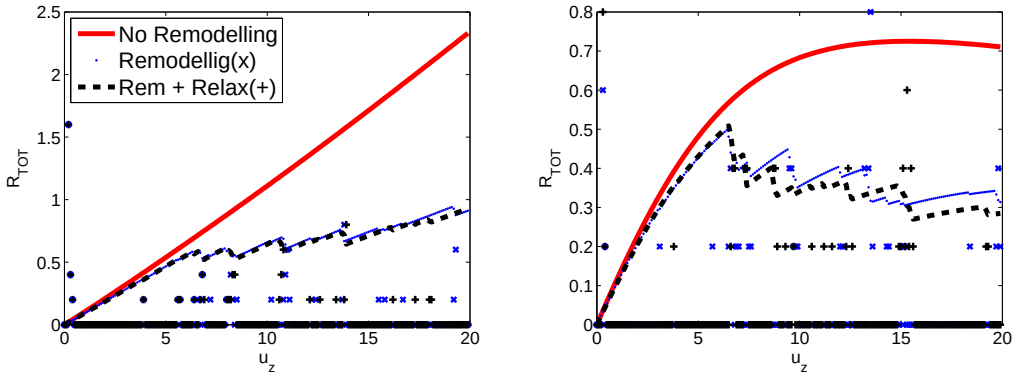

Figure 4.4: Total reaction R_{TOT} at the boundary with increasing imposed displacements for the flat monolayer. (a) Purely elastic model, (b) rheological model with active lengthening. The symbols ($\times$) and ($+$) indicate the number of connectivity changes per time-step for the two simulations with remodelling.

It can be drawn from the trends of the curves in Figure 4.4 that the stress relaxation does not have a strong effect on the total reaction, while the remodelling rate γ does have an impact in the non-linear response, introducing by itself an apparent stress relaxation. Figures 4.4a-b also indicate, with the symbols $\times$ (no relaxation) and $+$ (with relaxation), the number of connectivity changes that take place during the simulation for the cases when remodelling is activated. The height of the symbol corresponds to the number of connectivity changes divided by 10 for each time-step. It is clear that the jumps of the response are directly correlated with the changes of neighbours between cells. Since these are in general independent of the relaxation regime of the remodelling, it can be inferred that the relaxation of R_{TOT} is mostly due to these new connections, which have a stronger contribution on the minimisation of the stored elastic energy than the reduction of the stretching onto the new directions when relaxation is allowed.

In order to demonstrate the equivalence between the active rheological model

	$\gamma = 0$	$\gamma = 0.8$
Stress relaxation:	$L_n^{ij} = l_n^{ij}$	$L_n^{ij} = l_0^{ij}$
No stress relaxation:	$L_n^{ij} = L_0^{ij}$	$L_n^{ij} = 0.5(\boldsymbol{n}^i \cdot \mathbf{L}_n^i \boldsymbol{n}^i + \boldsymbol{n}^j \cdot \mathbf{L}_n^j \boldsymbol{n}^j)$

The case with $\gamma = 0.8$ and with no stress relaxation, the active length tensor $\mathbf{L}_n^i$ and $\mathbf{L}_n^j$ (time t_n and at nodes i and j) are computed according to the description in Section 2.1.3

Table 4.1: Computation of elements resting lengths with and without stress relaxation, with linear and active elasticity.

and the Maxwell model, we have applied the displacement history shown in Figure 4.5a, and plotted the corresponding total reaction in Figure 4.5b, which indeed relaxes to zero. It has been observed in laboratory experiments that monolayers do relax, but to a non-zero stress level (Harris et al., 2013). This is associated to the

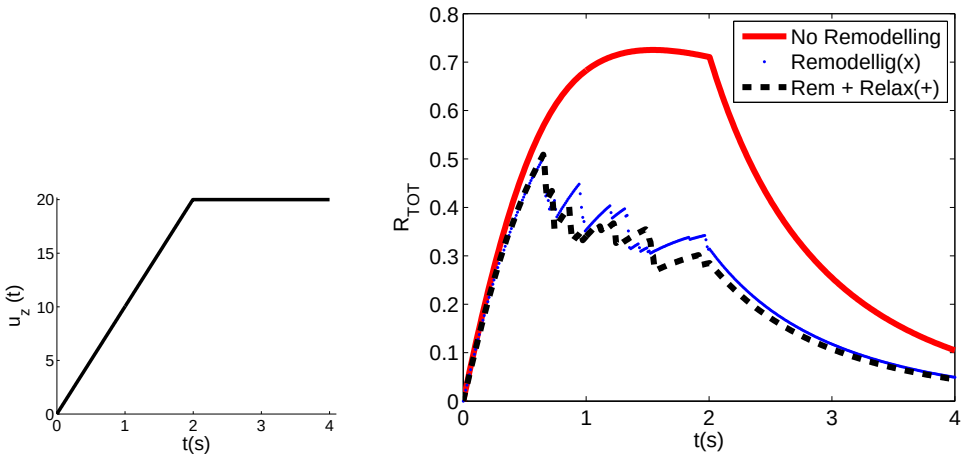

(a) (b)

Figure 4.5: (a) Time history of the applied strain. (b) Evolution of the total reaction as a function of time for the flat tissue and active rheological law.

elastic component of the polymeric structure of the cytoskeleton, and its inherent contractility. In the active model used here, which mimics the Maxwell model, the reaction tends to a zero value. Numerical examples with a non-zero asymptotic reaction are presented in Section 4.6.

We have compared in Figure 4.6 our numerical results with the experimental measurements in Harris et al. (2012). This figure shows the non-linear response of the tissue during an increasing applied displacement, which induced a loss of cell–cell integrity. In our case, this tissue rupture is presented by a decrease in the

number of cell–cell connectivities. The trends of the two curves agree qualitatively up to the measured experimental extension. Due to the adopted linear elastic model, our simulations do not capture the initial stiffening of the material. This may be recovered by modifying the quadratic potential in (2.1).

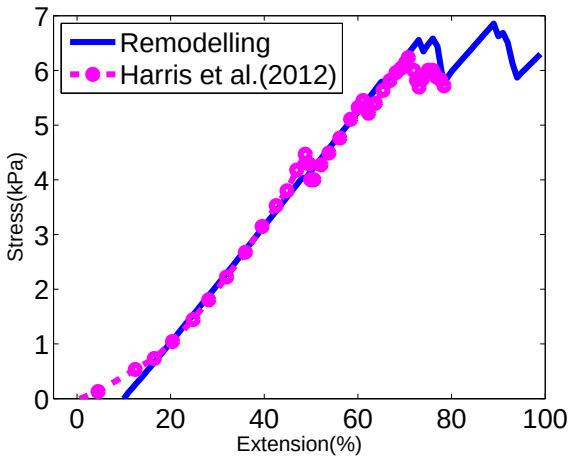

Figure 4.6: Comparison between the averaged stress value in the experimental results (Harris et al., 2012)

4.3 Active rheology in curved monolayers

We have tested a curved monolayer that has the shape of half a cylinder, with the axis on the x direction, and with the same number of nodes and similar dimensions: the projected area occupies the same domain $D = \{(X, Y) \| 0 \leq X \leq 11, 0 \leq Y \leq 10\}$ (see Figure 4.7). The monolayer is stretched along direction x, up to the displacement $u_x = 20$.

The same material models and the mapping of the surface described in Section 2.1.4 has been employed in order to apply the Delaunay triangulation. Figure 4.8 shows the evolution of the total reaction R_{TOT} and the number of connectivity changes. Similarly to the previous case, the trend of the curves is hardly affected by the update of the active length. However, in the three-dimensional case, the effect of remodelling has a more acute effect on the reduction of the total reaction than in the two-dimensional case, although this effect is only observed for larger imposed displacements.

The reduction of R_{TOT} may be attributed to two contributions. First, the sides $X = 0$ and $X = 11$ are fixed on the $y - z$ plane, and since Delaunay triangulation minimises the aspect ratio of the resulting triangles, no elongated triangles can be

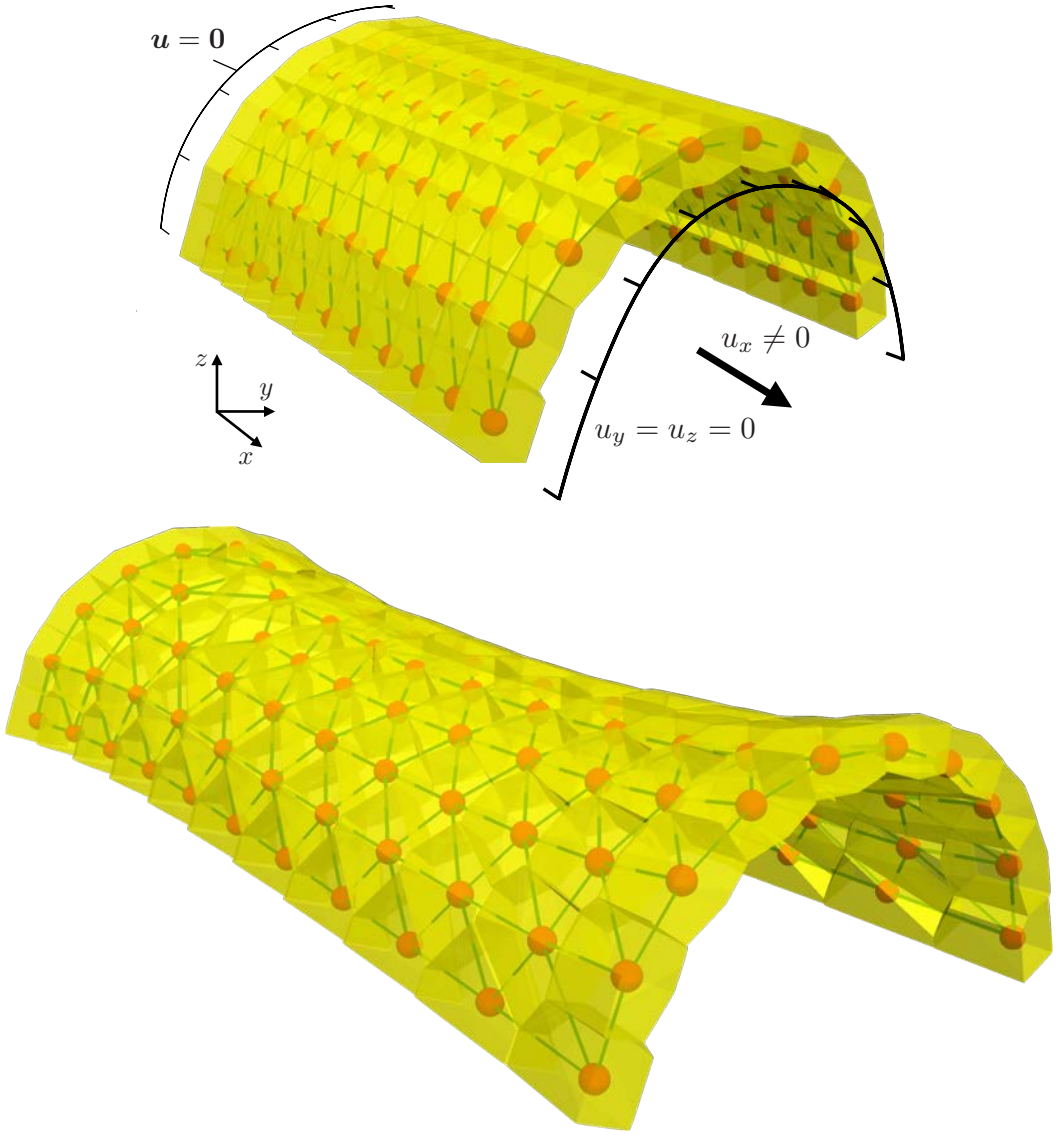

Figure 4.7: Example of curved monolayer. *Top*: initial geometry. *Bottom*: deformed geometry

created. As a result, larger cells are built at the middle of the monolayer. Second, and although the number of cells is constant, these are intercalated as the stretching process takes place: new connections are being created transversally to the stretching direction (y axis), which replace bars aligned on the x direction. We recognise that the first contribution is unrealistic. To resolve this issue, certain kinematic constraints should be added to the model in order to preserve the total volume of each cell. Such a constraint has been introduced in Section 2.2.3 for two-dimensional

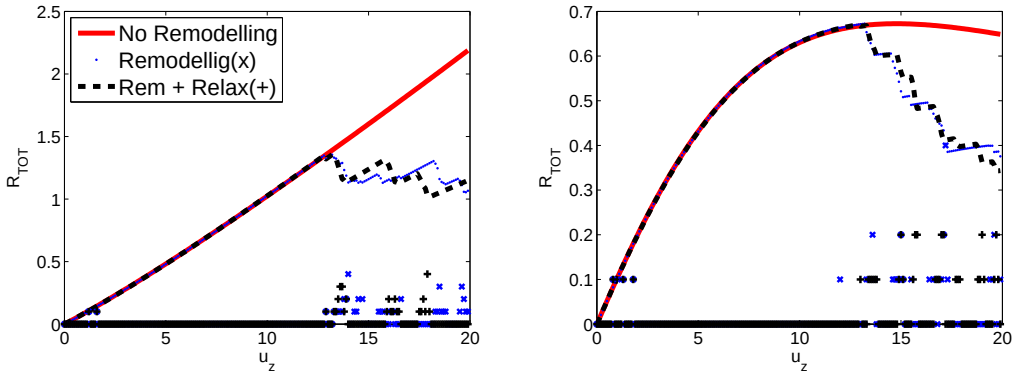

Figure 4.8: Total reaction at the boundary with increasing imposed displacements for the curved monolayer, (a) purely elastic model, (b) rheological model with active lengthening.

hybrid model. The second contribution, the intercalation process, has been observed in real embryogenetic movements of curved monolayer such as the endoderm of *Drosophila melanogaster* during germ band extension (Lecuit & Lenne, 2007). We notice that this effect is more pronounced in the three-dimensional case than in the flat monolayer, which restrained to remodel on a flat surface.

We also point out that the stress relaxation, due to either the active rheological model or the intercalation process, solely takes place along the direction of stretching. The material thus remodels anisotropically, as it has been observed on tissues during cell motility (Trepat et al., 2009).

4.4 Extension of square tissue employing hybrid model

We test our methodology by extending a square domain obtained from a random perturbation of a 10×10 grid of nodes (see Figure 4.9). The domain is formed by 81 cells, and subjected to a uniform 30% extension applied within 60 time-steps. This is the amount of stretch used in recent experimental tests on monolayers (Harris et al., 2012), and also the approximated stretch that some *in vivo* tissues in lungs or mitral valves can be subjected to. We will test two situations: extension with constant topology (evolution from (a) to (b)), and with remodelling (evolution from (a) to (c)). In the two situations we will apply the full and split approaches of the Equilibrium-Preserving Map (EPM). Since we aim to test here the effectiveness of the EPM, we prevent stress relaxation by using a small value of the remodelling rate $\gamma = 10^{-6}$, which makes the analysis quasi-static. The resting lengths remain thus constant, except when remodelling takes place.

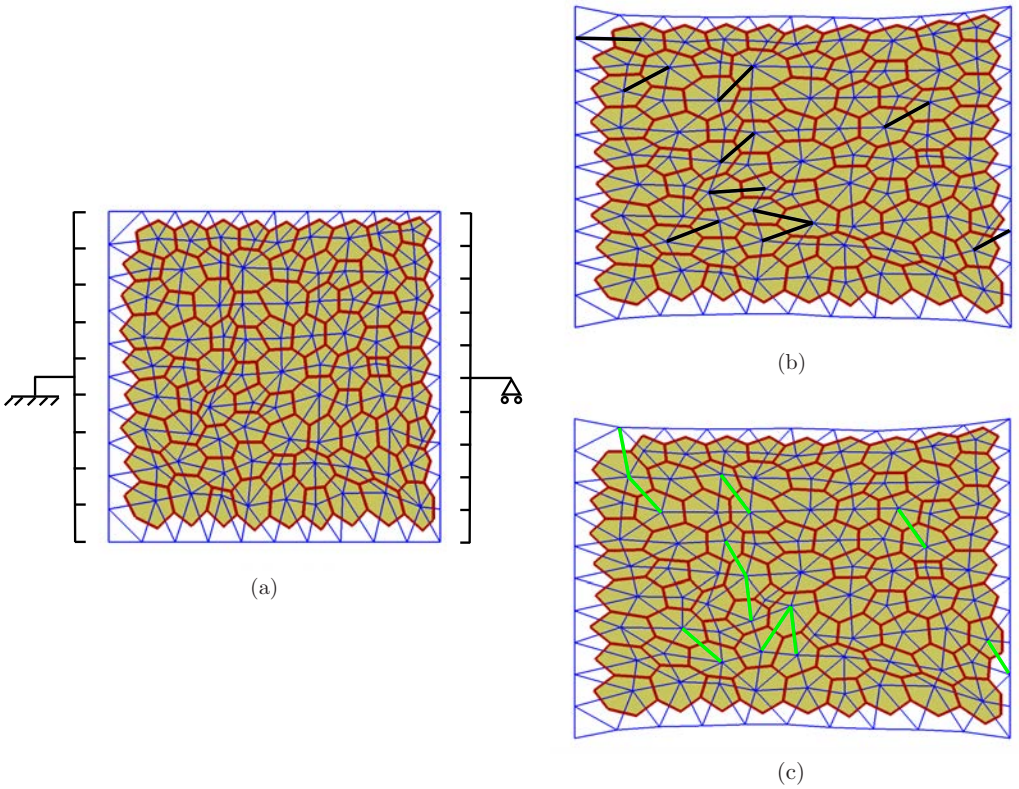

Figure 4.9: Tissue extension. (a) Initial configuration, (b) tissue configuration at 30% extension without remodelling, and (c) tissue configuration at 30% extension with remodelling. Replaced elements are marked in black in (b). Remodelled elements are marked in green.

4.4.1 Verification of EPM: fixed topology

To inquire the accuracy and effects of the EPM, we measure the horizontal total reaction at the right side as

$$R_x = \int_{\partial\Omega_{right}} (\boldsymbol{g}_D^i + \boldsymbol{g}_V^i) \cdot \begin{Bmatrix} 1 \\ 0 \end{Bmatrix} ds, \tag{4.1}$$

and the elastic energy of all the bar elements in the tissue during extension while keeping the topology constant. Figure 4.10 shows the evolution of the two quantities when $k_D = 10\, k_V$ (Figures 4.10a-b) and when $k_D = 0.1\, k_V$ (Figures 4.10c-d). It can be observed that in all cases the full-network and the split-network mappings give the same values as the tests with no mapping. This fact shows that the EPM is able to recover the same traction values as the ones when no computation of the resting lengths is applied, and that the system regularisation is not altering these lengths or the elastic response of the tissue.

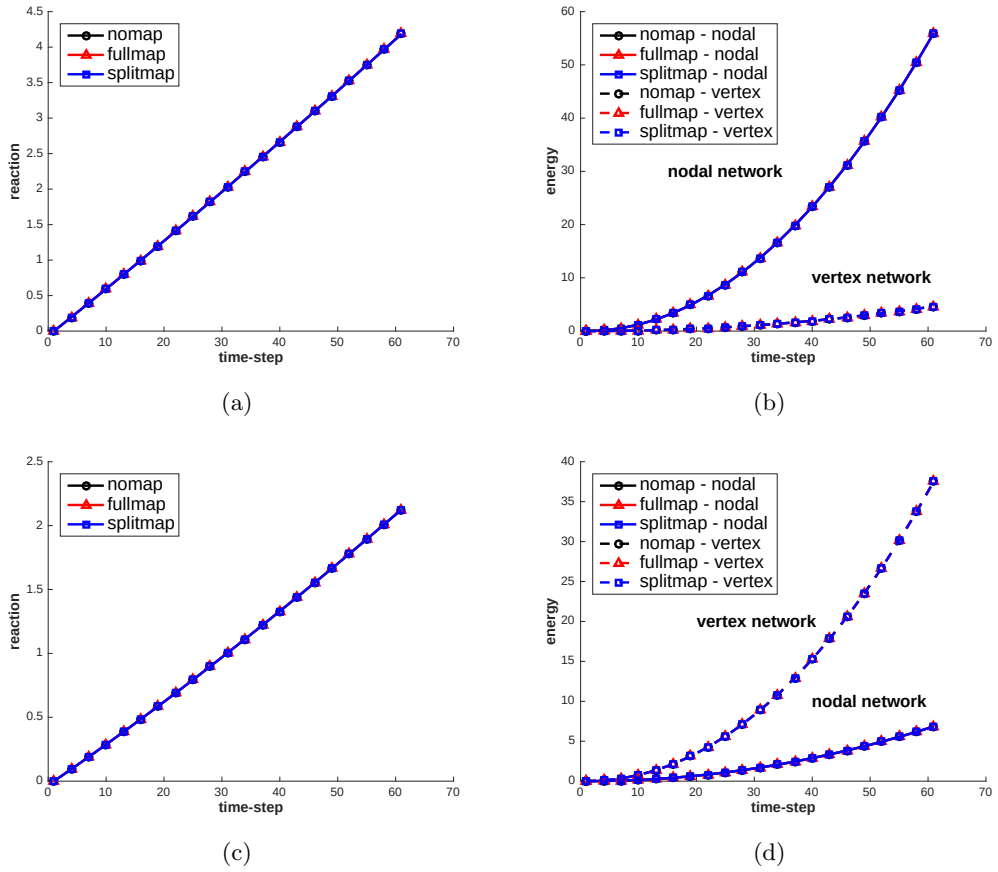

Figure 4.10: Tissue formed by linear elastic elements, under 30% uniform stretch applied within 60 time-steps while held at constant topology (no remodelling). Elements resting lengths, at each time-step, obtained by three approaches: fixed resting lengths (no network mapping), full-network mapping and split-network mapping. (a) Total tissue reaction while $k_D = 10\,k_V$, (b) potential energy of nodal and vertex networks while $k_D = 10\,k_V$, (c) total tissue reaction while $k_D = 0.1\,k_V$, and (d) potential energy of nodal and vertex networks while $k_D = 0.1\,k_V$.

4.4.2 Verification of EPM: variable topology

We now apply the same boundary conditions as in the previous tests, but allowing the tissue to remodel according to the Delaunay triangulation of the nodal positions. Figure 4.11 shows the total reaction at the right end of the tissue and the total elastic energy. We have monitored these three quantities under three conditions: no remodelling/mapping, remodelling with full-network mapping and remodelling with split-network mapping. We have tested also two sets of material properties: $k_D = 10\,k_V$ (Figures 4.11a-b), and $k_D = 0.1\,k_V$ (Figures 4.11c-d). The total number of remodelling events (elements that change their connectivity) is also plotted at each time-step, whenever this number is non-zero.

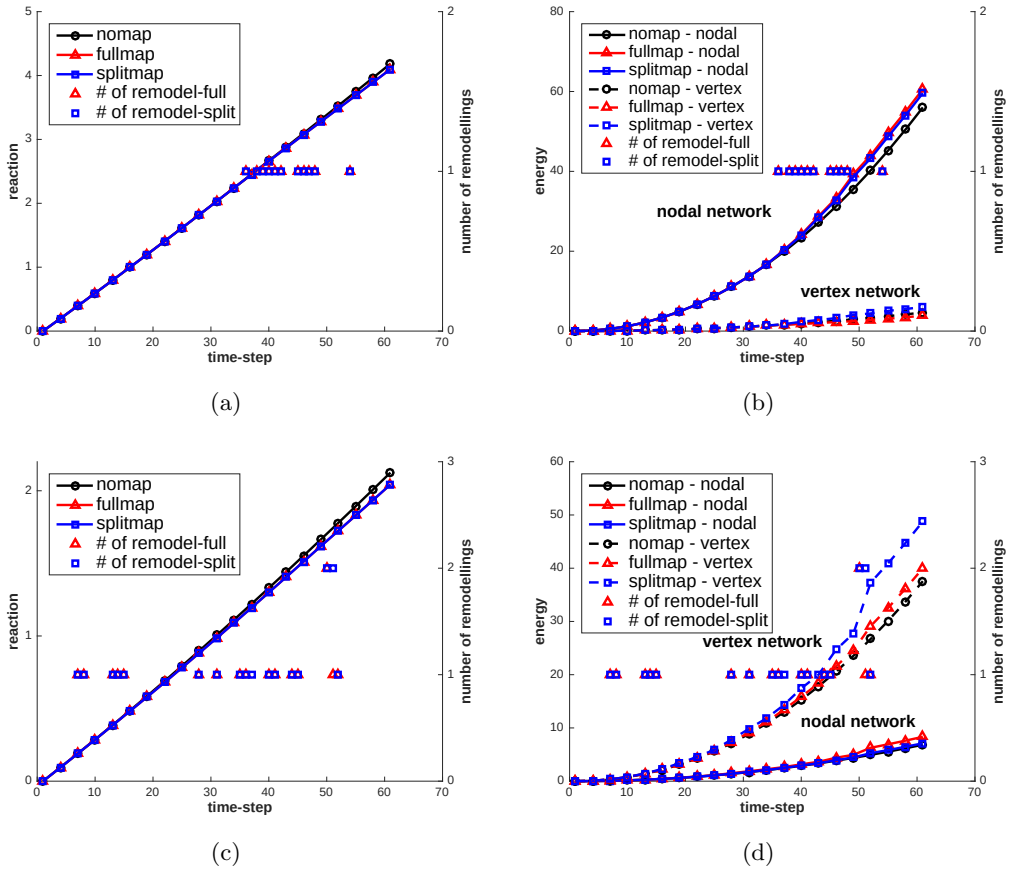

Figure 4.11: Tissue formed by linear elastic elements, under 30% uniform stretch applied within 60 time-steps which is allowed to remodel. Elements resting lengths, at each time step, obtained by three approaches: fixed resting lengths (no network mapping/remodelling), full-network mapping and split-network mapping with floating topology. (a) Total tissue reaction while $k_D = 10\,k_V$, (b) elastic energy of nodal and vertex networks while $k_D = 0.1\,k_V$, (c) total tissue reaction while $k_D = 0.1\,k_V$ and (d) elastic energy of nodal and vertex networks while $k_D = 0.1\,k_V$.

From the plots in Figure 4.11 it can be observed that the evolution of the total reaction is not substantially affected by the remodelling process. The elastic energy, however, suffers from deviations with respect to the case with no remodelling when the split-network EPM is used and the vertex network is stiffer than the nodal network. This drift is more severe when more remodelling events are encountered. Indeed, the split-network approach prevents the transfer of energy between the vertex and nodal networks, preventing in some cases the full preservation of the equilibrium conditions before the remodelling events. The total reaction of the tissue is in all cases not much affected by the mapping, which is in agreement with the fact that EPM aims to compute resting lengths distributions that match the nodal resultants before remodelling.

For the two sets of material parameters, the total reaction, and thus the tissue response, is very much unaffected by the remodelling for the two EPM approaches. The tissue keeps the correct aspect ratio of the cells while keeping the elastic response. Although cells may use remodelling events to relax their stress state, we here aim to independently control the stress relaxation and the remodelling events.

The computational cost of the simulations with and without remodelling, with and without area constraint, and for different combinations of the Delaunay and vertex networks is given in Table 4.2, when using the patch with 81 cells. The remodelling affects the first iteration of each increment, but may increase the computational cost by 15%-45% for cases without or with area constraint. Including this constraint is the factor that has a major effect, which may double the computational time. This may be attributed, besides the computation of additional terms in the Jacobian and residual, to the decrease of sparsity of the system matrix at each iteration due to the additional coupling that vertices include. The use of vertex network may also noticeably increase the computational time, while due to the methodology, assigning stiffness or not to the Delaunay has very small effects on the overall computational time.

We also note that the use of the vertex network may increase the memory requirement by about 60%. The present example required the use of 34.6 RAM MB, while the Delaunay only used 21.5 MB. These numbers reveal that cell-centred analyses are less expensive, but of course they provide no direct way to preserve cell area.

	Remodelling		No Remodelling	
	$\lambda_A = 0$	$\lambda_A > 0$	$\lambda_A = 0$	$\lambda_A > 0$
Delaunay	59	321	44	257
Vertex	153	376	108	376
Delaunay + Vertex	183	397	125	343

Table 4.2: Comparison of run time in seconds for different networks and remodelling combinations when using the stretching test with 81 cells. In the cases with remodelling, full-network mapping was used. Split-network mapping gave very similar computational times.

4.4.3 Analysis of ξ-relaxation

Tissue stiffness against tissue total reaction and strain energy is investigated by assigning a range of values to $\{k_D \; k_V\}$ at a constant total stiffness, $k_D + k_V = 1$, under two conditions: 1) when vertices are rigidly anchored at barycentres ($\boldsymbol{\xi} = \frac{1}{3}\{1 \; 1\}$), and 2) when vertices are allowed to change their relative positions with

respect to the barycentres (ξ-relaxation). Figure 4.12 compares the vertex network shown in Figure 4.9b for the two situations. The red network displays vertices anchored at barycentres, while in the green network vertices are relaxed under a penalisation factor $\lambda_\xi = 10^{-4}$.

In order to inspect the effect of ξ-relaxation we have analysed the reaction and energy of mainly nodal-driven or mainly vertex-driven tissues for different values of λ_ξ. Figure 4.13 shows the tissue response for different values of $k_V \in [0, 1]$ while keeping $k_D + k_V = 1$, and when the tissue is subjected to an 30% extension. Figure 4.13a shows that the total reaction decreases as tractions concentrate on the vertex network. This reduction is steeper when vertices are relaxed (lower values of λ_ξ). Figure 4.13b shows a faster drop in tissue total energy and a lower growth in vertex network energy when ξ-relaxation is allowed, while no significant effect on the energy of the nodal network is observed.

We have also analysed the difference of our equilibrated tractions with respect to the purely nodal and vertex equilibrium conditions: null sum of tractions at nodes and at vertices. This difference is computed as the mean value of the following nodal and vertex measures,

$$\begin{aligned} E_i &= \frac{\left\| \sum_{j \in S^i} \boldsymbol{t}_D^{ij} \right\|}{\sum_{j \in S^i} \left\| \boldsymbol{t}_D^{ij} \right\|}, \; i = 1, 2, \ldots, N_{nodes} \\ E_I &= \frac{\left\| \sum_{J \in S^I} \boldsymbol{t}_D^{IJ} \right\|}{\sum_{J \in S^I} \left\| \boldsymbol{t}_D^{IJ} \right\|}, \; I = 1, 2, \ldots, N_{tri}. \end{aligned} \tag{4.2}$$

Figures 4.13c and 4.13d plot the means,

$$\begin{aligned} \bar{E}_D &= \sum_i \frac{E_i}{N_{nodes}} \\ \bar{E}_V &= \sum_I \frac{E_I}{N_{tri}}, \end{aligned} \tag{4.3}$$

for the whole tissue. As expected, the nodal difference is zero when no stiffness is assigned to the vertex network ($k_V = 0$). As k_V increased, pure nodal equilibrium is increasingly violated, due to the coupling between the two networks. In most cases, this difference is below 10%, except when vertices are fixed. Pure vertex equilibrium is more severely affected by the kinematic constraint, but the difference also decreases rapidly as λ_ξ decreases. It can be observed that while the positions of the vertices in the two networks is very similar, purely vertex equilibrium drastically improves for approximately $\lambda_\xi < 10^{-2}$.

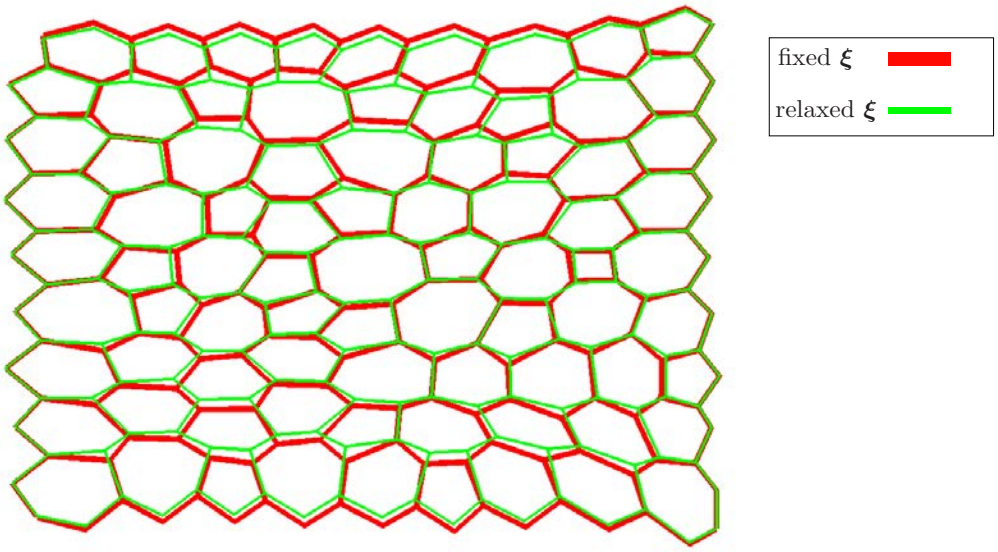

Figure 4.12: Deformed tissue at 30% extension. Red network represents vertices with fixed $\boldsymbol{\xi}$. Green network represents vertices when ξ-relaxation is allowed.

4.5 Wound healing

The hybrid model is tested to simulate a wound healing process in monolayers (Antunes et al., 2013). The evolution law in equation (3.15) is applied to the nodal and vertex networks with the values given in Table 4.3, which also indicates that the area constraint is imposed in order to mimic mechanical properties of the tissue. Topological changes in the tissue are allowed to examine the role of cell motility and cell intercalation during wound healing.

k_D	k_V	γ_D	γ_V	ε_D^c	ε_V^c	λ_A
0.1	2.0	0.5	0.5	1.0	0.7	10.0

Table 4.3: Material parameters employed in the wound healing example.

Wounding and wound healing processes are simulated during the consecutive steps below:

1. To resemble the initial condition of *in vivo* tissue before wounding, the modelled tissue is let to reach a contractile state given by the values ε_D^c and ε_V^c in Table 4.3 for the nodal and vertex networks respectively, and the evolution law

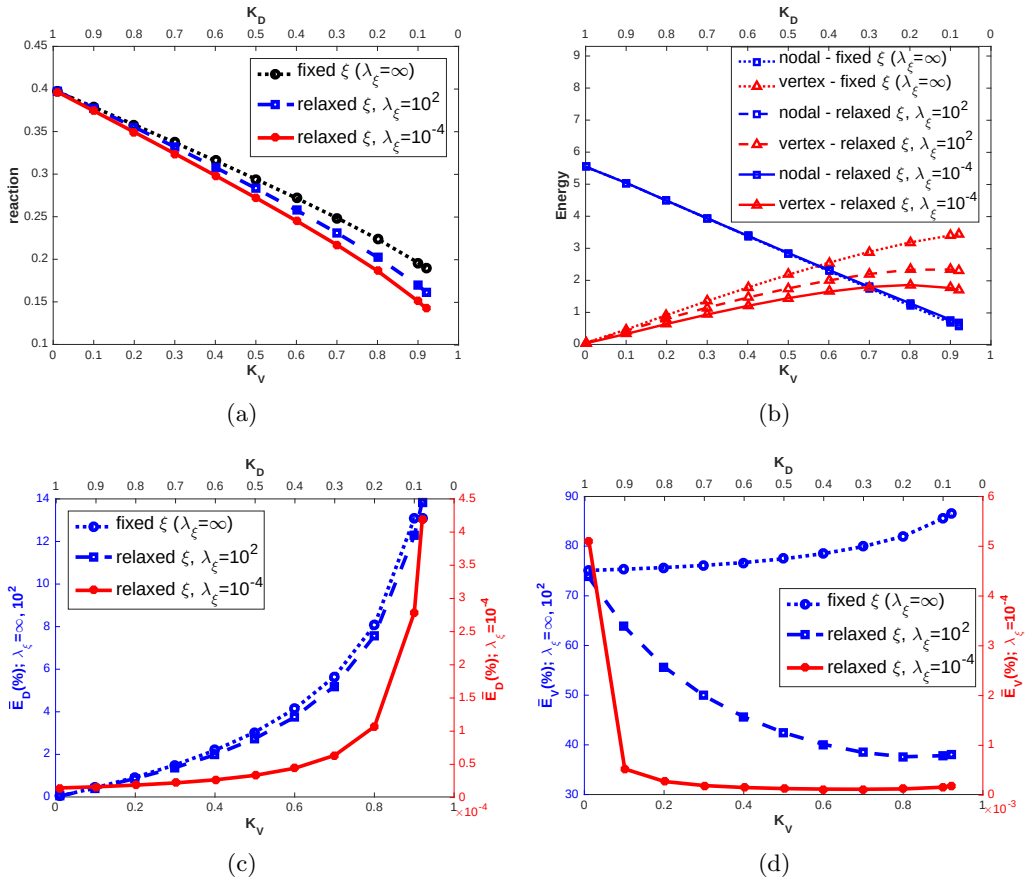

Figure 4.13: Analysis of response of tissue composed of elastic elements, under 30% uniform stretch applied within a single time-step for different combinations of $\{k_D\ k_V\}$ while $k_D + k_V = 1$, with and without ξ-relaxation. (a) Tissue reaction, (b) nodal, vertex and total strain energy of the tissue, (c) mean of the difference between pure nodal and coupled equilibrium $\bar{E}_D$ for different values of λ_ξ (note the difference on the scaling of the left and right vertical axes), and (d) mean of the difference between pure nodal and coupled equilibrium $\bar{E}_V$ for different values of λ_ξ. See equations (4.2) and (4.3) for the definitions $\bar{E}_D$ and $\bar{E}_V$.

affecting elements resting lengths, during 50 time-steps. This time is found to be sufficient to reach a steady asymptotic state.

2. Wounding by laser ablation of cells is analogised by a significant reduction of stiffness in nodal and vertex elements encircled by the wound edge, as well as removing the area constraint on wounded cells. In wounded areas we set $k_D^{wounded} = 0.1\,k_D$ and $k_V^{wounded} = 0.1\,k_V$. Also, vertices at the wound edge are allowed to relax by resorting to the ξ-relaxation. This is done to avoid unrealistic zig-zag effects on the profile of the wound edge. Figures 4.14a, 4.14d and 4.14g show the tissue initially after wounding., without remodelling,

and with full- and split-network remodelling, respectively.

3. To simulate tissue eventual response to wounding, after 12 time-steps, contractility on the elements of the vertex network surrounding the wound (wound ring) is multiplied by 5 in order to pattern actomyosin concentration, as it has been experimentally observed (Brugués et al., 2014). Figures 4.14b and 4.14e show how the extra contractility on the wound edge results in higher tractions on the wound ring, at both non-remodelling and remodelling tissues.

4. Additional tractions on the wound ring cause the wounded area being squeezed by the cells on the wound boundary. Figures 4.14c and 4.14f show the wound closure with and without remodelling. Including remodelling during the tissue evolution results in less cell elongation at the wound edge and allows cells to relocate during wound closure.

In the full-network strategy (Figures 4.14d-f), since the total residual of nodal and vertex networks were preserved at the nodes, the interplay of stresses in nodal and vertex networks could not preserve the higher stress in the vertex elements at the wound ring. Instead, the split-network strategy could provide the expected higher stress in the elements at the wound ring. This is due to preserving nodal residual independently in each of the networks.

We have compared the time evolution of the relative wounded area $r_A(t)$ computed as

$$r_A(t) = \frac{A_{wounded}(t)}{A_{wounded}(t_{ablation})}. \tag{4.4}$$

In Figure 4.15a we show this ratio for the numerical simulations and also for experimental measurements (Brugués et al., 2014) of the same phenomenon on an ablated tissue of Madin Darby kidney (MDCK) cells. It can be observed that the evolution of the area matches approximately the experimental values during the early stages of the closure, but that at longer time scales, the area of the experimental images closes at a slower rate. This fact may reveal that the contractility of the ring is not maintained constant, but that it may reduce progressively. Further analysis is though required to quantify the evolution of the contraction of the tissue. Also, although intercalations away from the wound edge have been observed in some systems (Razzell et al., 2014), the impact of remodelling on wound closure in biological systems needs to be further investigated.

In order to also evaluate the effects of using solely a nodal or a vertex network, we show in Figure 4.15b the same ratio r_A for tissues where nodal or vertex stiffness has been reduced by 10^{-6}. The resulting evolutions of r_A reveal that the inhibition of the Delaunay has very minor effects, while removing vertex stiffness does slow

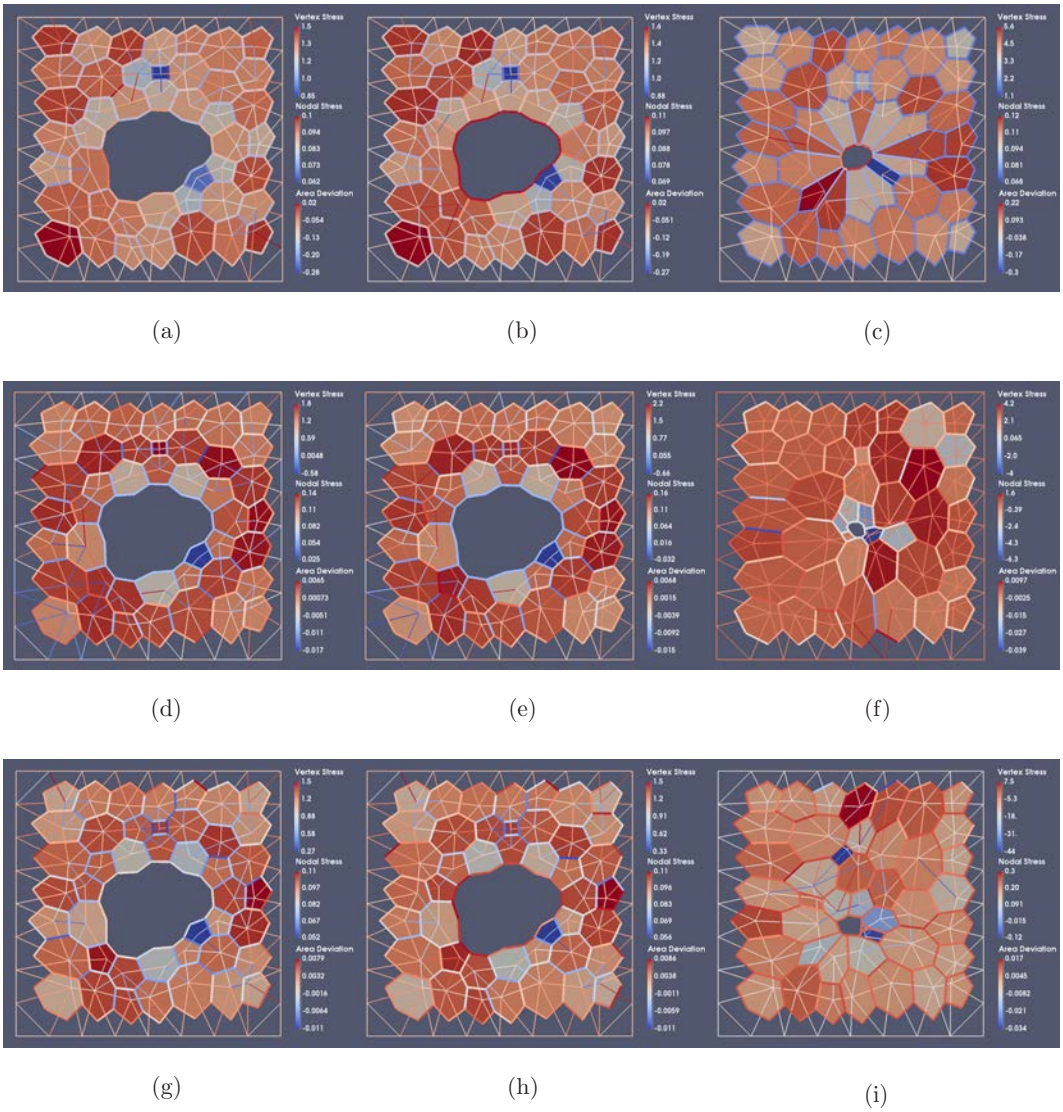

(a) (b) (c)

(d) (e) (f)

(g) (h) (i)

Figure 4.14: Wound healing model visualised at different stages. The deviation from cells initial area, as well as traction values along nodal and vertex elements, are shown in the corresponding colour-bars at each stage. (a-c) Wound healing in non-remodelling tissue. (d-f) Wound healing with full-network EPM. (g-i) Wound healing with split-network EPM. Figures (a), (d) and (g) correspond to time-steps just after wounding. Figures (b), (e) and (h) correspond to when extra contractility was applied on the elements at the wound ring. Figures (c), (f) and (i) correspond to when extra contractility at the wound edge caused wound closure.

down dramatically the area evolution. This can be explained by the fact that the vertex network is responsible of the increased contractility at the wound ring.

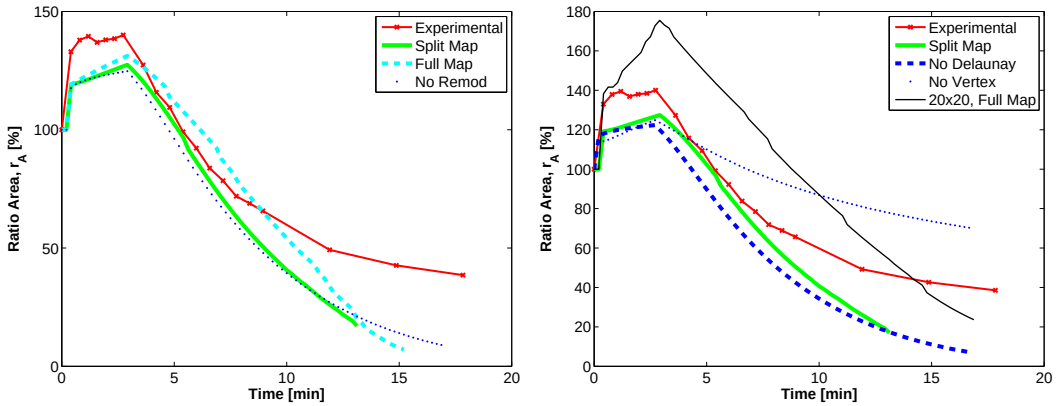

(a) (b)

Figure 4.15: Time evolution of the wounded area. (a) Comparison for the three models shown in Figure 4.14 and an experimental measurement (Brugués et al., 2014), and (b) comparison for the case with split-network mapping, inhibiting Delaunay network, inhibiting vertex network, and using a larger mesh with 20×20 initial nodes (361 cells).

Figure 4.15b also includes the corresponding time variation for a larger patch with 361 cells, and a larger ablated area of 7 cells (see Figure 4.16). In this case, the peak of the area recoil is, as expected, also larger. In all cases, the slope of the ratio is initially similar to the experimental one, but it diverges for longer time scales. Further calibration of the contractility and its regulation is intended as a future work.

4.6 Short timescale stress relaxation in monolayers

Stress relaxation in monolayers has been shown to be biphasic, commencing with a large amplitude fast relaxation occurring within the first approximate 5 s, followed by a small amplitude slow relaxation and reaching a plateau after almost 60 s. It has been shown that the first and second phases of the relaxation are dominated by a power law and an exponential response, respectively (Khalilgharibi et al., 2017). Figure 4.17a shows an experimental plot of a monolayer stress relaxation during 100 s.

Based on the evolution law represented by equation (3.24), we have fitted stress relaxation of a monolayer with a hybrid network with fixed topology, and non-linear active nodal and vertex elements for the whole 100 s, onto the experimental curve (see Figure 4.17b). In order to mimic the monotonous stress trend at the second phase, we have combined a linear elastic element in parallel with every vertex element. The model aims to fit the power law, and as it can be observed in the figure, this evolution is captured during the first 20 s. In the second phase, where

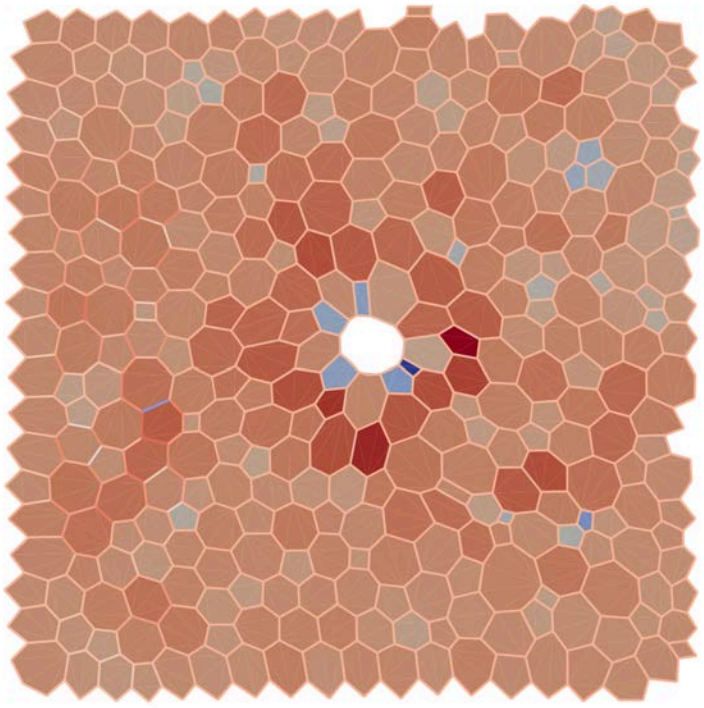

Figure 4.16: Wound healing simulation for a patch with 361 cells. The same parameters as those used in Figure 4.14 are employed here, but with 7 ablated cells, instead of 5, and for the same stage shown in Figures 4.14c, 4.14f and 4.14i. Cell colours indicate area relative variations.

cytoskeleton mechanics seems to play a major role, the numerical results are less satisfactory, although the trend does not depart substantially from the experimental curve. The value of the mechanical parameters used to fit the simulation results are given in Table 4.4.

We also have fitted a non-linear active single element, onto the relaxation curve during the first phase. Figure 4.18a shows the single element evolution, fitted onto the experimental plot during the first 20 s of the monolayer stress relaxation. Figure 4.18b shows the evolution of the resting length L for the single element stress re-

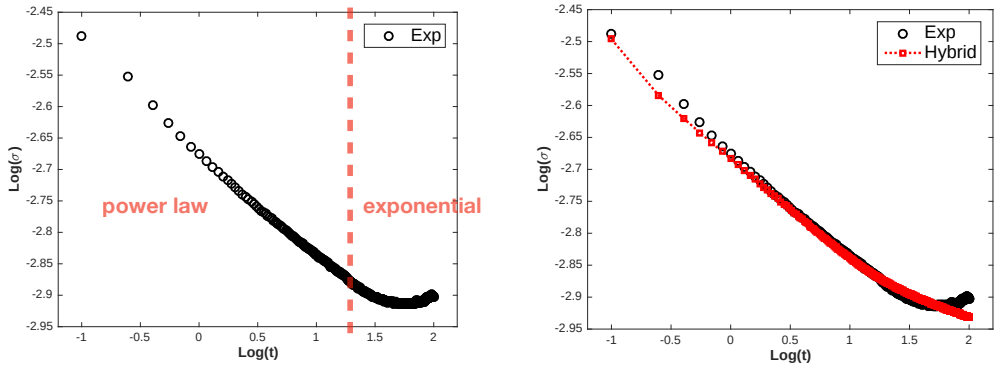

(a) (b)

Figure 4.17: Biphasic stress relaxation of monolayer based on experimental results (Khalilgharibi et al., 2017). (a) The left side represents the first approximate 20 s where a power law dominates the relaxation, whereas the right side pertains to the rest of relaxation period, dominated by an exponential trend.(b) Stress relaxation of hybrid network with non-linear active nodal elements and a double-branched vertex network of non-linear active and linear elastic elements combined in parallel, fitted onto the experimental trend.

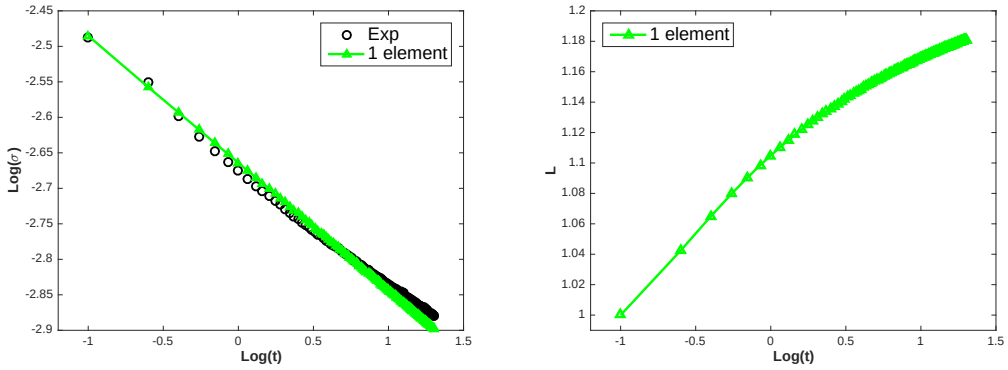

(a) (b)

Figure 4.18: (a) Stress relaxation of simulated a non-linear active single element, against the experimental plot during the first 20 s from the beginning of the relaxation period. (b) Evolution of the single element resting length L during the first 20 s from the beginning of the relaxation.

laxation with respect to the evolution law presented in equation (3.24) . The initial resting length has been normalised to a value of 1 unit of length.

	k_D	γ_D	ε_D^c	k_{V1}	γ_{V1}	ε_{V1}^c	k_{V2}	n
1 element	0.011	1000	0.005	-	-	-	-	6.4
Hybrid	0.0049	450	0.004	0.0008	0.15	0.03	0.004	4

Table 4.4: Mechanical parameters used to fit the simulation results onto the experimental results.

Chapter 5

Conclusions

We have presented a cell-centred approach by which the non-linear response of soft cellular tissues, formed as either monolayer or three-dimensional aggregate, can be simulated by modelling the relative position of cell centres and their topological changes. At this stage, we have presented a method to handle mechanical response in curved monolayers by removing the rigid-body modes of the system, as well as introducing L-tensor method to handle the tissue topological changes by computing an appropriate resting length for the remodelled elements.

At a later stage, we have presented a hybrid approach which includes the mechanical effect of cell boundaries in the tissues total response. This approach allows to independently control the material properties of the cell boundaries and the cytoplasm (cell interior). The methodology solves the mechanical equilibrium of the two networks in a coupled manner. The numerical results show that the approach can reproduce relevant phenomena such as tissue extension or wound healing.

The method resorts to a rheological law that is based on an evolution law of the resting length (Doubrovinski et al., 2017; Muñoz & Albo, 2013). This evolution is controlled through the remodelling rate γ. For high values of γ, the tissue relaxes and adapts its reference free configuration rapidly, while for very low values of γ, a purely elastic response is recovered. Parameter γ plays a similar role than the inverse of the viscosity η in Maxwell models, with slight differences in the time evolution of the responses (see Muñoz & Albo (2013) for a more detailed analysis). As such, the proposed evolution law yields an exponential relaxation with a characteristic time that is proportional to γ^{-1}. Other non-linear evolution laws giving rise to power-like relaxations may be included by resorting to more sophisticated evolution laws of the resting length L like the one introduced in Section 3.3.2. Further use of these rheological laws can be found in Asadipour et al. (2016) and Khalilgharibi et al. (2017) in the context of developmental biology.

The variations of the resting lengths allow also to design an Equilibrium-Preserving Map (EPM) that computes a set of resting lengths and traction field that mimics the force distribution on the nodal and vertex network before remodelling. The numerical examples presented show that this recovery of tractions alters minimally the stress state.

The EPM can be regarded as a mapping that preserves the stress state while transferring the stress state onto a different network. The map aims to smooth the force jumps between connectivity changes, and although it minimises the effects of the cell forces during cell reorganisation, it eases numerically these changes which do have an effect in the macroscopic shape of the tissue, as it occurs in morphogenetic events (Hardin & Walston, 2004). Furthurmore, the EPM also opens the possibility of designing mappings that regulate the force jumps in a controlled manner or along certain directions only. We have not investigated this possibility yet, but we plan to do so in the future.

Publications

Here is a list of co-authored publications:

- Mosaffa P, Asadipour N, Millán D, Rodríguez-Ferran A, and Muñoz JJ. **Cell-centred model for the simulation of curved cellular monolayers**. *Comp. Part. Mech.*, 2(4):359–370, 2015.

- Mosaffa P, Rodríguez-Ferran A, and Muñoz JJ. **Hybrid cell-centred/vertex model for multicellular systems with equilibrium-preserving remodelling**. *Int. J. Num. Meth. Biomed. Engng.*, 2017 (In press).

- Khalilgharibi N, Fouchard J, Asadipour N, Yonis A, Harris A, Mosaffa P, Fujita Y, Kabla A, Baum B, Muñoz JJ and Charras GT. **Stress relaxation in epithelial monolayers arises from length change controlled by actomyosin**, 2017 (Manuscript submitted for publication).

Conferences

Here is a list of participated conferences:

- Muñoz JJ, Mosaffa P, Mao Y, Tetley R, Asadipour N, and Rodríguez-Ferran A. **Hybrid cell-centred/vertex model for large tissue deformations**. *VII European Congress on Computational Methods in Applied Sciences and Engineering–ECCOMAS*. Crete, Greece, June 2016.

- Muñoz JJ, Mosaffa P, Asadipour N, Millán D, and Rodríguez-Ferran A. **Hybrid cell-centred/vertex model for three-dimensional monolayers**. *VI International Conference on Computational Bioengineering–ICCB*. Barcelona, Spain, September 2015.

- Mosaffa P, Asadipour N, Millán D, Rodríguez-Ferran A, and Muñoz JJ. **Hybrid cell-centred/vertex model for cellular monolayers**. *4th International Conference on Computational and Mathematical Biomechanical Engineering–CMBE*. Cachan, France, July 2015.

- Mosaffa P and Muñoz JJ. **Cell-centered model for tissues undergoing large embryonic deformations**. *5th EMBO Conference on The Molecular and Cellular Basis of Regeneration and Tissue Repair–EMBO*. Sant Feliu de Guixols, Spain, October 2014.

- Muñoz JJ, Asadipour N, and Mosaffa P. **Cell-centered model for nonlinear tissue rheology and active remodelling**. *11th World Congress on Computational Mechanics (WCCM XI)–IACM-ECCOMAS*. Barcelona, Spain, July 2014.

- Muñoz JJ, Albo S, Conte V, Asadipour N, and Mosaffa P. **Predictive model for cell softening and hardening**. *5th International Conference on Mechanics of Biomaterials and Tissues–ICMOBT*. Sitges, Spain, December 2013.

Chapter 6

Future work

This work has paved the path towards the blending of cell-based and vertex models. Although the resulting simulations have been able to reproduce the main trends of observed experiments in monolayers, further work is needed for improving the modelling capabilities and widening the applicability of the model. For instance, Delaunay triangulation could be modified in order to allow the presence of elongated cells, which do not necessarily have an optimal aspect ratio. Other issues that are foreseen for further development are listed next:

6.1 Mapping of new vertices

ξ-relaxation has been so far applied to relax vertices at the wound edge, providing a more realistic wound shape by indirectly minimising the wound perimeter. However, when topological changes occur at the wound edge, previous vertices may be replaced by new ones. A robust method should be employed to calculate appropriate parametric value for $\boldsymbol{\xi}$ in order to preserve the smoothness of the wound edge. Figure 6.1 shows vertices at the wound edge at time t_{n+1} projected onto the wound edge at time t_n. Currently, the topological changes at the wound edge are handled by the method presented in Figure 6.1. Nevertheless, this method occasionally may not preserve the smoothness. We plan to investigate a more robust technique to handle locating fresh vertices at the wound edge in the near future.

6.2 Three-dimensional extension of cellular monolayers and aggregates

The thickness in cellular monolayers has been so far ignored by the presented model. We have only applied the cell-centred approach on three-dimensional flat and curved monolayers (see Sections 2.1.4 and 2.1.5), where cells boundary has no mechanical role in the system. Extending the model to three-dimensional geome-

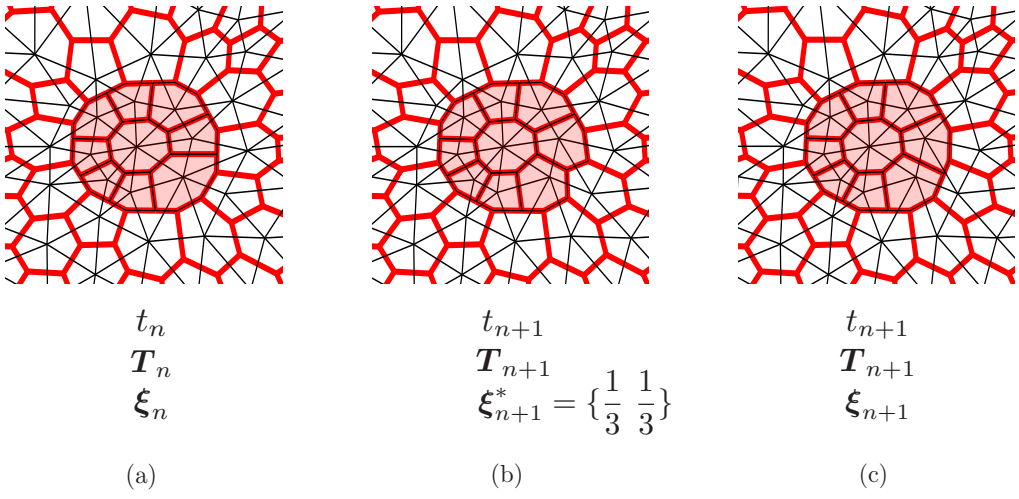

Figure 6.1: Projection of vertices onto the previous wound edges. (a) system at time t_n, topology $\boldsymbol{T}_n$ and parametric coordinate $\boldsymbol{\xi}_n$, (b) system at time t_{n+1}, topology $\boldsymbol{T}_{n+1}$and reset parametric coordinate $\boldsymbol{\xi}^*_{n+1} = \{1/3\ 1/3\}$ for vertices at the wound edge, and (c) system at time t_{n+1}, configuration $\boldsymbol{T}_{n+1}$ and parametric coordinate $\boldsymbol{\xi}_{n+1}$ obtained by projection of the wound edge vertices onto the wound edge at time t_n.

tries, make the model capable of comprising a wider range of phenomena such as apical-basal constriction in monolayers, as well as including cells volume penalisation by regulating the interplay between cells height and cells apical-basal area.

Voronoi tessellation has been applied as a standard method to provide a packed conjunction of convex subspaces (cells). However, the validity of this method is limited to Delaunay configurations (see Section 2.2.1). Previously, we have employed barycentric tessellation as a solution to this issue in two-dimensional systems. However, since handling cell faces in 3-D, formed by barycentric vertices, is a complicated task, application of barycentric tessellation to three-dimensional geometries will need further investigation.

6.3 Calibration of parameters

Mechanical parameters presented in the model, need to be quantified for different cases by fitting the simulations onto experimental results. Single cell and single vertex ablation experiments dedicated to study recoil dynamics of tissue, are helpful to quantify parameters such as k_D, k_V, ε^c, γ and λ_A.

6.4 Strain dependent contractility

So far, contractility ε^c has been applied as an external parameter to the model. Further study of tissue recoil dynamics against monitored actomyosin concentration during wound closure shows a variable concentration of contractile agents within the wound closure. Developing a regulatory approach by which contractility is defined as correlating with strain level is in our future scope.

6.5 Definition of stress and transport in Delaunay

As yet, the stress distribution by cells bulk matter within the tissue, has been governed by line forces along the nodal elements between cell centres. Replacing line forces by body stress within the cells surface/volume will result in more realistic behaviour by the tissue.

Additionally, the triangulation provided by the Delaunay algorithm may be also employed to discretise and solve transport of agents and its concentration variations. This approach may open the possibility to model coupled chemo-mechanical processes.

6.6 Oscillations

Further studies on tissue recoil dynamics juxtaposed with monitored actomyosin level during wound closure, suggest a time lag δt between the mechanical and chemical signalling which may be also responsible of the observed oscillation and fluid like response. To simulate the observed delay, the time variable of resting length $\dot{L}_{n+1}$ needs to be implemented as a function of previous strain

$$\frac{\dot{L(t)}}{L(t)} = \gamma(\varepsilon(t - \delta t)).$$

Appendix A

Notation

The notation used in this thesis is summarised in Tables A.1-A.3.

A^m, A_0^m	Current and initial area of cell m. Equation (2.24).
A_T	Total area of cells on the tissue. Equation (2.29).
B^i	Vertices that surround node i. Equation (2.21).
$\boldsymbol{C}_n$	Nodal configuration at time t_n. Section 2.1.
$\mathbf{e}^{ij}$	Unit vector from node $\boldsymbol{x}^j$ to node $\boldsymbol{x}^i$. Equation (2.40)
$\mathbf{e}^{IJ}$	Unit vector from vertex $\boldsymbol{y}^J$ to vertex $\boldsymbol{y}^I$. Equation (2.40)
$\mathbf{e}_z$	Unit vector in z direction. Equation (2.28).
E_i, E_I	Error measures of vertex and nodal equilibrium, resp. Equation (4.2).
$E^i_{\mathbf{L}}$	Error measure of nodal equilibrium obtained by **L**-tensor method. Equation (2.7).
$\bar{E}_D, \bar{E}_V$	Mean error measures per node of nodal and per vertex of vertex equilibrium, resp. Equation (4.3).
$\boldsymbol{g}^i_A$	Area constraint force contribution at node i. Equation (2.30).
$\boldsymbol{g}_c$	Augmented residual of nodal network by zero-eigenmode penalisation. Equation (2.11).
$\boldsymbol{g}^i_D$	Nodal force contribution at node i. Equation (2.2).
$\boldsymbol{g}^i_V$	Vertex force contribution at node i. Equation (2.21).
$\boldsymbol{g}_x$	Residual vector stemming from $\frac{\partial W}{\partial \boldsymbol{x}}$. Equation (2.34).
$\boldsymbol{g}_y$	Residual vector stemming from $\frac{\partial W}{\partial \boldsymbol{\xi}}$. Equation (2.34).
$\boldsymbol{g}^I_\xi$	Force contribution of ξ-relaxation penalisation at vertex I. Equation (2.35).
$\mathbf{J}$	Matrix such that $(\boldsymbol{y}^I \times \boldsymbol{y}^J) \cdot \mathbf{e}_z = \boldsymbol{y}^I \cdot \mathbf{J}\boldsymbol{y}^J$. Equation (2.28).
k_D, k_V	Stiffness of nodal and vertex network, resp. Equations (2.1) and (2.17).

Table A.1: Notation. The explicit definition of the symbols can be found in the indicated section or equation.

$\mathbf{K}$	Stiffness matrix. Section 2.1.4.
$\mathbf{K}_c$	Augmented stiffness matrix by zero-eigenmode penalisation. Equation (2.11).
$\mathbf{L}^i$	Active length tensor of node i. Equation (2.6).
l^{ij}, L^{ij}	Current and resting lengths of bar element between nodes i and j. Equation (2.3).
l^{IJ}, L^{IJ}	Current and resting lengths of bar element between vertices I and J. Equation (2.19).
n_{eig}	Number of zero-eigenmodes. Equation (2.10).
n_{sd}	Number of space dimensions. Section 2.1.3.
$\boldsymbol{n}^{ij}$	Outward normal at nodal bar element between nodes i and j. Equation (2.12).
$\boldsymbol{n}^{IJ}$	Outward normal at vertex bar between vertices I and J. Equation (2.27).
$\boldsymbol{n}^j$	Unit vector pointing towards node j along nodal element ij. Equation (2.6).
N_D	Number of bars in nodal network. Equation (2.1).
N_m	Number of segments that surround cell centred at $\boldsymbol{x}^m$. Equation (2.27).
N_{cells}	Number of cells and internal nodes. Section 2.2.1.
N_{nodes}	Total number of nodes. Section 2.1.
N_{tri}	Total number of triangles in nodal network. Section 2.1.
$\mathbf{N}^j$	Matrix containing components of unit vector $\boldsymbol{n}^j$. Section 2.1.3.
N_V	Total number of vertex bars. Section 2.2.2.
$\boldsymbol{P}$	Set of points defining cell centres. Section 2.1.2.
$p^i(\boldsymbol{\xi}^I)$	Shape function defining vertex positions. Equation (2.16).
P^m	Set of segments that form boundary of cell m. Equation (2.27).
p_r	Penalisation factor of zero-eigenmodes of stiffness matirx. Equation (2.10).
$q(\alpha)$	Interpolation function of cell boundary. Equation (2.16).
r, R	Inradius and circumradius of atriangle, reps. Equation (2.5).
$\boldsymbol{r}^i$	Nodal reaction due to boundary condition on node i. Equation (2.39).
$\boldsymbol{r}^i_D, \boldsymbol{r}^i_V$	Nodal and vertex contribution to reaction $\boldsymbol{r}^i$. Equation (2.45)
S^i	Set of nodes connected to node i. Equation (2.2).
S^I	Set of vertices connected to vertex I. Equation (2.21).
$\bar{S}^i$	Set of nodes surrounding node i, including node i itself. Equation (2.30).
$\boldsymbol{t}^{ij}_D$	Traction vector at node i exerted by nodal element ij. Equation (2.2).

Table A.2: Notation (continuation).

$\boldsymbol{t}_V^{IJ}$	Traction vector at vertex I exerted by vertex element IJ. Equation (2.19).
t_n	nth time-step. Section 2.1.
$\mathcal{T}^I$	Triangle where vertex I is located. Section 2.1.
$\boldsymbol{T}_n$	Connectivity of nodal network at time t_n. Section 2.1.
tol_R	Aspect ratio tolerance. Equation (2.5).
$\boldsymbol{u}$	Displacement vector. Equation (2.10).
W_A	Energy term associated to area penalisation. Equation (2.24).
W_c	Augmented energy of nodal network by penalisation of zero-eigenmodes. Equation (2.10).
W_D, W_D^{ij}	Total nodal strain energy and strain energy of nodal element ij. Equation (2.1).
W_V, W_V^{IJ}	Total vertex strain energy and strain energy of vertex element IJ. Equation (2.17).
$\boldsymbol{x}^i$	Position of node i. Section 2.1.
$\boldsymbol{X}_n$	List of nodal positions at time t_n. Section 2.1.
$\boldsymbol{y}^I$	Position of vertex I. Section 2.2.1.
α	Local coordinate of points in vertex bars. Equation (2.16).
γ	Remodelling rate in rheological model. Equation (3.9).
δ	Numerical precision. Section 2.1.4.
δ_{IJ}	Kronecker delta. Equation (2.38).
$\delta_{mj}^{pq}, \delta_{IJ}^{PQ}$	See definitions in equation (2.43).
Δt	Time increment. Equation (3.8).
ϵ	Distance of each off-set node from the corresponding boundary node. Equation (2.12).
ε^c	Contractility of bar elements. Equation (3.15).
$\varepsilon_D^c, \varepsilon_V^c$	Contractility employed in nodal and vertex network. Section 4.5.
$\varepsilon^{ij}, \varepsilon^{IJ}$	Strain at nodal and vertex bar elements, resp. Equations (2.1) and (2.17).
η	Viscousity. Equation (3.3).
θ^{ij}, θ^{IJ}	Inverse of resting lengths L^{ij} and L^{IJ}, resp. Section 2.2.5.
κ	Eigen value of system stiffness matrix $\mathbf{K}$. Section 2.1.4.
λ_A	Penalty terms for area constraint. See equation (2.24).
λ_L	Penalisation factor of regularisation term. Equation (2.44).
λ_ξ	Penalty terms for ξ-relaxation. See equation (2.31).
$\boldsymbol{\xi}^I$	Local coordinate of vertex I in triangle $\mathcal{T}^I$. Section 2.2.1.
π_D, π_V	Nodal and vertex contributions in EPM, resp. Equation (2.45).
π_F, π_S	Functionals of full- and split-network EPM. Equations (2.39) and (2.45).
σ	Stress. Equation (3.1).
Ω^i	Domain of cell i. Section 2.2.1.

Table A.3: Notation (continuation).

Appendix B

Inradius and circumradius

B.1 Inradius

In 2-D Euclidean geometry, *inradius*, r, of a triangle is the radius of the circle tangetial to the sides of the triangle. *Incentre* is the centre of this circle.

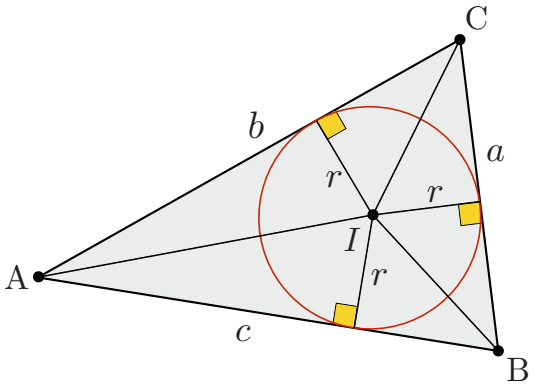

Figure B.1: $\triangle ABC$ and its incircle

Let I be the incentre of $\triangle ABC$.

Let r be the inradius of $\triangle ABC$.

The total area of $\triangle ABC$, $\mathcal{A}$, is equal to the sum of the areas of the triangles formed by the vertices of $\triangle ABC$ and its incentre:

$$\mathcal{A} = \mathcal{A}_{\triangle AIB} + \mathcal{A}_{\triangle BIC} + \mathcal{A}_{\triangle CIA}. \tag{B.1}$$

Let AB, BC and CA be the bases of $\triangle AIB$, $\triangle BIC$ and $\triangle CIA$ respectively.

The length of AB, BC and CA respectively are c, a and b.

The altitude of each of these triangles is r. Thus from are of triangle in terms of side and altitude:

$$\begin{aligned} \mathcal{A}_{\triangle AIB} &= \frac{cr}{2} \\ \mathcal{A}_{\triangle BIC} &= \frac{ar}{2} \\ \mathcal{A}_{\triangle CIA} &= \frac{br}{2}. \end{aligned} \tag{B.2}$$

Thus, from (B.1) and (B.2) we have,

$$r = \frac{2\mathcal{A}}{a+b+c}. \tag{B.3}$$

B.2 Circumradius

The *circumradius*, R, of a triangle is the radius of the circle in which the triangle can be inscribed. *Circumcentre* is the centre of this circle.

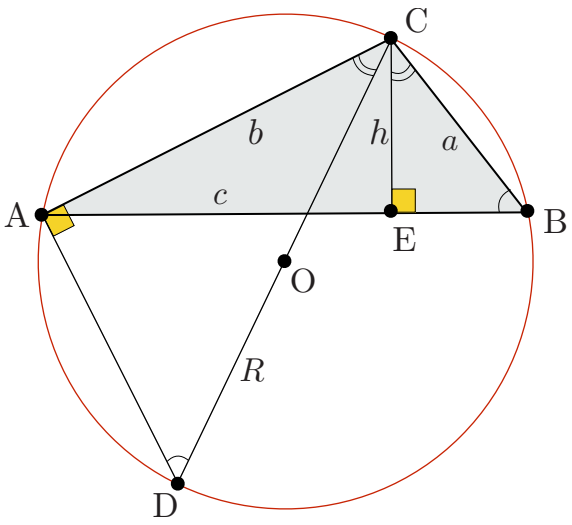

Figure B.2: $\triangle ABC$ and its circumcircle

Let O be the circumcentre of $\triangle ABC$.

Let $\mathcal{A}$ be the area of $\triangle ABC$.

Let a perpendicular be dropped from C to AB at E.

Let $h := CE$

Then by area of triangle in terms of side and altitude we have,

$$\begin{aligned} \mathcal{A} &= \frac{ch}{2} \\ \Rightarrow h &= \frac{2\mathcal{A}}{c}. \end{aligned} \tag{B.4}$$

Let a diameter of the circumcircle CD be passed through O.

By definition of circumradius, $CD = 2R$.

By Thales' theorem, $\angle CAD$ is a right angle.

Then, as angles on equal arcs are equal, $\angle ADC = \angle ABC$. As $\triangle ACD$ and $\triangle ECB$ are right angle triangles with one similar angle, then $\angle ACD = \angle ECB$. Then as equiangular triangles are similar, we have,

$$\begin{aligned} \frac{CA}{CD} &= \frac{CE}{CB} \\ \Rightarrow \frac{b}{2R} &= \frac{h}{a}. \end{aligned} \tag{B.5}$$

Then from (B.4) and (B.5) we have,

$$\begin{aligned} \mathcal{A} &= \frac{abc}{4R} \\ \Rightarrow R &= \frac{abc}{4A}. \end{aligned} \tag{B.6}$$

B.3 Aspect ratio of triangles

We define the aspect ratio as $\frac{r}{R}$. From (B.3) and (B.6) we have,

$$\frac{r}{R} = \frac{8\mathcal{A}^2}{(abc)(a+b+c)}. \tag{B.7}$$

Then by replacing $a = \|B - C\|$, $b = \|C - A\|$, $c = \|A - B\|$, and $\mathcal{A} = \frac{\|(B-A)\times(C-A)\|}{2}$ in (B.7) we have,

$$\frac{r}{R} = \frac{2\left\|(B-A)\times(C-A)\right\|^2}{(\|A-B\|\,\|B-C\|\,\|C-A\|)(\|A-B\| + \|B-C\| + \|C-A\|)}. \tag{B.8}$$

B.4 Aspect ratio of tetrahedrons

In three-dimensional Euclidean Geometry, a tetrahedron inradius, r, is the radius of the sphere tangetial to the faces of the tetrahedron, whereas circumradius of a tetrahedron is defined as the radius of the sphere circumscribed to it. Given $\boldsymbol{A}$, $\boldsymbol{B}$, $\boldsymbol{C}$, and $\boldsymbol{D}$ the coordinates of the tetrahedron vertices are

$$\begin{aligned}\boldsymbol{A} &= (A_x, A_y, A_z),\\ \boldsymbol{B} &= (B_x, B_y, B_z),\\ \boldsymbol{C} &= (C_x, C_y, C_z),\\ \boldsymbol{D} &= (D_x, D_y, D_z).\end{aligned}$$

Then by resorting to the following parentheses (Casey, 1988)

$$\alpha = \begin{vmatrix} A_x & A_y & A_z & 1\\ B_x & B_y & B_z & 1\\ C_x & C_y & C_z & 1\\ D_x & D_y & D_z & 1 \end{vmatrix},$$

$$\boldsymbol{N}_{ABC} = (\boldsymbol{B} - \boldsymbol{A}) \times (\boldsymbol{C} - \boldsymbol{A}),$$

$$\gamma = \begin{vmatrix} A_x^2 + A_y^2 + A_z^2 & A_x & A_y & A_z\\ B_x^2 + B_y^2 + B_z^2 & B_x & B_y & B_z\\ C_x^2 + C_y^2 + C_z^2 & C_x & C_y & C_z\\ D_x^2 + D_y^2 + D_z^2 & D_x & D_y & D_z \end{vmatrix},$$

$$F_x = \begin{vmatrix} A_x^2 + A_y^2 + A_z^2 & A_y & A_z & 1\\ B_x^2 + B_y^2 + B_z^2 & B_y & B_z & 1\\ C_x^2 + C_y^2 + C_z^2 & C_y & C_z & 1\\ D_x^2 + D_y^2 + D_z^2 & D_y & D_z & 1 \end{vmatrix}, \; F_y = \begin{vmatrix} A_x^2 + A_y^2 + A_z^2 & A_x & A_z & 1\\ B_x^2 + B_y^2 + B_z^2 & B_x & B_z & 1\\ C_x^2 + C_y^2 + C_z^2 & C_x & C_z & 1\\ D_x^2 + D_y^2 + D_z^2 & D_x & D_z & 1 \end{vmatrix},$$

$$F_z = \begin{vmatrix} A_x^2 + A_y^2 + A_z^2 & A_x & A_y & 1\\ B_x^2 + B_y^2 + B_z^2 & B_x & B_y & 1\\ C_x^2 + C_y^2 + C_z^2 & C_x & C_y & 1\\ D_x^2 + D_y^2 + D_z^2 & D_x & D_y & 1 \end{vmatrix},$$

the inraduis, r, of the tetrahedron can be computed as

$$r = \frac{|\alpha|}{\|\boldsymbol{N}_{ABC}\| + \|\boldsymbol{N}_{ABD}\| + \|\boldsymbol{N}_{ACD}\| + \|\boldsymbol{N}_{BCD}\|}, \tag{B.9}$$

while the circumradius, R, reads

$$R = \frac{\sqrt{F_x^2 + F_y^2 + F_z^2 + 4\alpha\gamma}}{2\,|\alpha|}. \tag{B.10}$$

Therefore, by replacing from (B.9) and (B.10) the ratio $\frac{r}{R}$ which measures the flatness of the tetrahedron is given by

$$\frac{r}{R} = \frac{2\,|\alpha|^2}{(\|\boldsymbol{N}_{ABC}\| + \|\boldsymbol{N}_{ABD}\| + \|\boldsymbol{N}_{ACD}\| + \|\boldsymbol{N}_{BCD}\|)\sqrt{F_x^2 + F_y^2 + F_z^2 + 4\alpha\gamma}}. \tag{B.11}$$

Appendix C

Proof of uniqueness of active length tensor $\mathbf{L}^i$

We will here prove that the solution of the system of equations in (2.8) at a given node i is unique if the vectors $\boldsymbol{n}^j$ that define the cell–cell connectivities at node i and that form matrix $\mathbf{A}$ span $\mathbb{R}^{n_{sd}}$.

By definition, matrix $\mathbf{A}$ is semi-positive definite (SPD) and symmetric. We will here prove that matrix $\mathbf{A}$ is in fact positive definite (PD) when the vectors $\boldsymbol{n}^j$ span $\mathbb{R}^{n_{sd}}$, and hence gives a unique solution. Matrix $\mathbf{A}$ is PD if the following implication holds:

$$\bar{\mathbf{L}}^{iT}\mathbf{A}\bar{\mathbf{L}}^i = 0 \Rightarrow \bar{\mathbf{L}}^i = 0. \tag{C.1}$$

But, by setting $\boldsymbol{l}^{ij} = \mathbf{L}^i\boldsymbol{n}^j$, we have that,

$$\bar{\mathbf{L}}^{iT}\mathbf{A}\bar{\mathbf{L}}^i = \sum_{j=1}^{S^i} \mathbf{L}^i\boldsymbol{n}^j \cdot \mathbf{L}^i\boldsymbol{n}^j = \sum_{j=1}^{S^i} \left\|\boldsymbol{l}^{ij}\right\|^2.$$

So,

$$\sum_{j=1}^{S^i} \mathbf{L}^i\boldsymbol{n}^j \cdot \mathbf{L}^i\boldsymbol{n}^j = 0 \Rightarrow \boldsymbol{l}^{ij} = \mathbf{0},\ \forall j, \tag{C.2}$$

i.e., implication in (C.1) may be also expressed as,

$$\sum_{j=1}^{S^i} \mathbf{L}^i\boldsymbol{n}^j \cdot \mathbf{L}^i\boldsymbol{n}^j = 0 \Rightarrow \mathbf{L}^i\boldsymbol{n}^j \cdot \mathbf{e}^k = 0,\ \forall j, k.$$

Setting $\boldsymbol{n}^j = \alpha_l^j \mathbf{e}^l$ we have that,

$$\mathbf{L}^i \boldsymbol{n}^j \cdot \mathbf{e}^k = \alpha_l^j \mathbf{L}^i \mathbf{e}^l \cdot \mathbf{e}^k = \sum_l \alpha_l^j L_{kl}^i,$$

with $L_{kl}^i = \mathbf{L}^i \mathbf{e}^l \cdot \mathbf{e}^k$ the component kl of tensor $\mathbf{L}^i$. Therefore, (C.2) is equivalent to,

$$\sum_l \alpha_l^j L_{kl}^i = 0, \ \forall k, j.$$

By denoting by $\mathbf{L}_k^i$ the k-th row of the tensor L^i, this condition may be also expressed as,

$$\boldsymbol{n}^j \cdot \mathbf{L}_k^i = 0, \ \forall k, j,$$

that is, the vector $\boldsymbol{n}^j$ are orthogonal to each one of the rows of $\mathbf{L}^i$. If the vectors $\boldsymbol{n}^j$ span the whole space $\mathbb{R}^{n_{sd}}$, this is only possible when $\mathbf{L}_k^i = 0$, as we wanted to prove. If the tensor $\bar{\mathbf{L}}^i$ is not assumed symmetric, the uniqueness of the solution can be also proved by considering an alternative matrix $\mathbf{N}^j$ in the definition of matrix $\mathbf{A}$, but following very similar steps.

Appendix D

Voronoi diagram

Consider $\triangle ABC$ with vertices at $\boldsymbol{X}_A$, $\boldsymbol{X}_B$, $\boldsymbol{X}_C$ and the intersection of the perpendicular bisectors P at $\boldsymbol{X}_P$. Bisectors of $\triangle ABC$ intersect with the sides of the triangle at L, M and N. $\boldsymbol{X}_P$ can be interpolated in terms of $\boldsymbol{X}_A$, $\boldsymbol{X}_B$ and $\boldsymbol{X}_C$

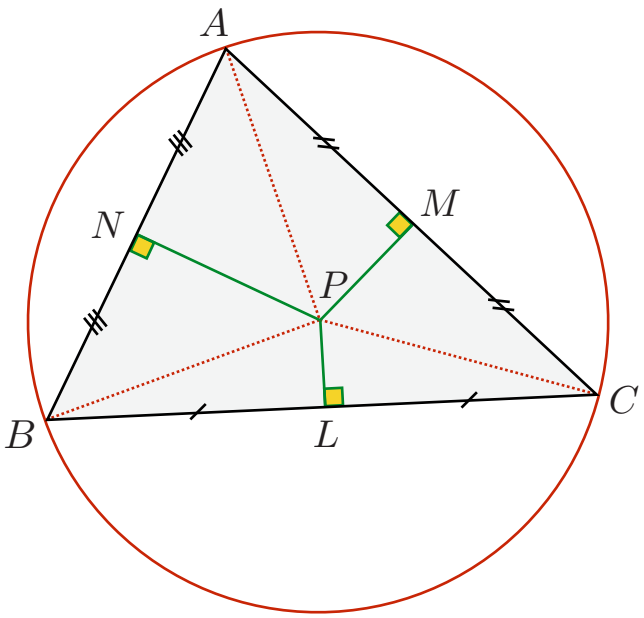

Figure D.1: $\triangle ABC$ and its perpendicular bisectors

so that,

$$\boldsymbol{X}_P = \alpha \boldsymbol{X}_A + \beta \boldsymbol{X}_B + \gamma \boldsymbol{X}_C,$$

where based on barycentric coordinates,

$$\alpha = \frac{S_{\triangle PBC}}{S_{\triangle ABC}}, \quad \beta = \frac{S_{\triangle APC}}{S_{\triangle ABC}}, \quad \gamma = \frac{S_{\triangle ABP}}{S_{\triangle ABC}}. \tag{D.1}$$

For the surface of $\triangle PBC$ with respect to the definition of cross product we have,

$$S_{\triangle PBC} = \frac{1}{2} \left\| (\boldsymbol{X}_C - \boldsymbol{X}_P) \times (\boldsymbol{X}_B - \boldsymbol{X}_P) \right\|. \tag{D.2}$$

By the definition of perpendicular bisector, PC and PB are radii of circumcircle of $\triangle ABC$, thus $\overline{PC} = \overline{PB}$ and $\overline{PC} = \frac{\overline{BC}}{2\cos(\angle PCL)}$. Also by the definition of central and inscribed angles $\angle BPC = 2\angle BAC$ and with respect to the total internal angles of a triangle, it can be shown that $\cos(\angle PCL) = \sin(\angle BAC)$. Therefore, with respect to the definition of inner product (D.2) can be written as

$$S_{\triangle PBC} = \frac{\left\| \boldsymbol{X}_C - \boldsymbol{X}_B \right\|^2 (\boldsymbol{X}_B - \boldsymbol{X}_A) \cdot (\boldsymbol{X}_C - \boldsymbol{X}_A)}{4 \left\| (\boldsymbol{X}_C - \boldsymbol{X}_A) \times (\boldsymbol{X}_B - \boldsymbol{X}_A) \right\|},$$

and by replacing $S_{\triangle ABC} = \frac{1}{2} \left\| (\boldsymbol{X}_B - \boldsymbol{X}_A) \times (\boldsymbol{X}_C - \boldsymbol{X}_A) \right\|$ to (D.1) for α we have,

$$\alpha = \frac{\left\| \boldsymbol{X}_C - \boldsymbol{X}_B \right\|^2 (\boldsymbol{X}_B - \boldsymbol{X}_A) \cdot (\boldsymbol{X}_C - \boldsymbol{X}_A)}{2 \left\| (\boldsymbol{X}_B - \boldsymbol{X}_A) \times (\boldsymbol{X}_C - \boldsymbol{X}_A) \right\|^2}. \tag{D.3}$$

By the same approach for $S_{\triangle APC}$ and $S_{\triangle ABP}$, we obtain β and γ in (D.1) as,

$$\begin{aligned} \beta &= \frac{\left\| \boldsymbol{X}_C - \boldsymbol{X}_A \right\|^2 (\boldsymbol{X}_A - \boldsymbol{X}_B) \cdot (\boldsymbol{X}_C - \boldsymbol{X}_B)}{2 \left\| (\boldsymbol{X}_A - \boldsymbol{X}_B) \times (\boldsymbol{X}_C - \boldsymbol{X}_B) \right\|^2} \\ \gamma &= \frac{\left\| \boldsymbol{X}_B - \boldsymbol{X}_A \right\|^2 (\boldsymbol{X}_B - \boldsymbol{X}_C) \cdot (\boldsymbol{X}_A - \boldsymbol{X}_C)}{2 \left\| (\boldsymbol{X}_B - \boldsymbol{X}_C) \times (\boldsymbol{X}_A - \boldsymbol{X}_C) \right\|^2}. \end{aligned} \tag{D.4}$$

Appendix E

Linearisation

E.1 General linearisation steps with ξ-relaxation

When ξ-relaxation is included, the total residual vector $\boldsymbol{g} = \{\boldsymbol{g}_x^T \ \boldsymbol{g}_y^T\}^T$ is split in a nodal $\boldsymbol{g}_x$ and ξ contributions $\boldsymbol{g}_y$ (see equation (2.34)). Each nodoal and vertex constribution is given by,

$$\begin{aligned} \boldsymbol{g}_x^i &= \boldsymbol{g}_D^i + \boldsymbol{g}_V^i + \boldsymbol{g}_A^i, \\ \boldsymbol{g}_y^I &= \boldsymbol{g}_V^I + \boldsymbol{g}_A^i + \boldsymbol{g}_\xi^I. \end{aligned}$$

Vectors $\boldsymbol{g}_D^i$, $\boldsymbol{g}_V^i$ and $\boldsymbol{g}_A^i$ are written in equations (2.2), (2.21) and (2.30), and the vertex contributions $\boldsymbol{g}_V^I$, $\boldsymbol{g}_A^I$ and $\boldsymbol{g}_\xi^I$ given in equations (2.37). The non-linear equations $\boldsymbol{g} = \boldsymbol{0}$ are solved with a Newton-Raphson process that at each iteration k reads:

$$\left\{ \begin{array}{c} \delta\boldsymbol{x} \\ \delta\boldsymbol{\xi} \end{array} \right\} = - \left[\begin{array}{cc} \mathbf{K}_{xx} & \mathbf{K}_{xy} \\ \mathbf{K}_{yx} & \mathbf{K}_{yy} \end{array} \right]_k^{-1} \left\{ \begin{array}{c} \boldsymbol{g}_x \\ \boldsymbol{g}_y \end{array} \right\}_k , \tag{E.1}$$

and is updated as

$$\left\{ \begin{array}{c} \boldsymbol{x} \\ \boldsymbol{\xi} \end{array} \right\}_{k+1} = \left\{ \begin{array}{c} \boldsymbol{x} \\ \boldsymbol{\xi} \end{array} \right\}_k + \left\{ \begin{array}{c} \delta\boldsymbol{x} \\ \delta\boldsymbol{\xi} \end{array} \right\},$$

as long as the two following conditions are met,

$$\left\{ \begin{array}{rl} \sqrt{\|\delta\boldsymbol{x}\|^2 + \|\delta\boldsymbol{\xi}\|^2} & > tol \\ \|\boldsymbol{g}\| & > tol \end{array} \right. ,$$

with tol a sufficiently small tolerance. In our numerical examples we used $tol = 10^{-10}$.

The block matrices in (E.1) correspond to the following linearisation terms,

$$\mathbf{K}_{xx}^{ij} = \frac{\partial \boldsymbol{g}_D^i}{\partial \boldsymbol{x}^j} + \frac{\partial \boldsymbol{g}_V^i}{\partial \boldsymbol{x}^j} + \frac{\partial \boldsymbol{g}_A^i}{\partial \boldsymbol{x}^j} \tag{E.2}$$

$$\mathbf{K}_{xy}^{iJ} = \frac{\partial \boldsymbol{g}_V^i}{\partial \boldsymbol{\xi}^J} + \frac{\partial \boldsymbol{g}_A^i}{\partial \boldsymbol{\xi}^J} \tag{E.3}$$

$$\mathbf{K}_{yx}^{Ij} = \frac{\partial \boldsymbol{g}_V^I}{\partial \boldsymbol{x}^j} + \frac{\partial \boldsymbol{g}_A^I}{\partial \boldsymbol{x}^j}$$

$$\mathbf{K}_{yy}^{IJ} = \frac{\partial \boldsymbol{g}_V^I}{\partial \boldsymbol{\xi}^J} + \frac{\partial \boldsymbol{g}_A^I}{\partial \boldsymbol{\xi}^J} + \frac{\partial \boldsymbol{g}_\xi^I}{\partial \boldsymbol{\xi}^J}, \tag{E.4}$$

where due to the expressions of $\boldsymbol{g}_D^i$ and $\boldsymbol{g}_\xi^I$, we have used the fact that $\frac{\partial \boldsymbol{g}_D^i}{\partial \boldsymbol{y}^J}$ and $\frac{\partial \boldsymbol{g}_\xi^I}{\partial \boldsymbol{x}^j}$ vanish. Also note that since our equlibrium equations stem from the linearisation of an energy function $W(\boldsymbol{x}, \boldsymbol{\xi})$, we have that,

$$\mathbf{K}_{xy}^{iJ} = \frac{\partial^2 (W_V + W_A)}{\partial \boldsymbol{x}^i \partial \boldsymbol{\xi}^J} = \left[\frac{\partial^2 (W_V + W_A)}{\partial \boldsymbol{\xi}^I \partial \boldsymbol{x}^j}\right]^T = \mathbf{K}_{yx}^{Ij\,T}.$$

In the next sections we will give the linearisation of the terms in (E.2)-(E.4).

E.2 Linearisation of nodal and vertex tractions $\boldsymbol{t}_D^{ij}$ and $\boldsymbol{t}_V^{IJ}$

Many of the derivations detailed below will involve the linearisation of the traction vectors given in equations (3.14),

$$\boldsymbol{t}_D^{ij} = \frac{\partial W_D^{ij}}{\partial \boldsymbol{x}^i} = \frac{\varepsilon^{ij}}{L^{ij}} \left(1 - \frac{l^{ij}}{L^{ij}} \frac{\partial L^{ij}}{\partial l^{ij}}\right) \mathbf{e}^{ij}$$

$$\boldsymbol{t}_V^{IJ} = \frac{\partial W_V^{IJ}}{\partial \boldsymbol{y}^I} = \frac{\varepsilon^{IJ}}{L^{IJ}} \left(1 - \frac{l^{IJ}}{L^{IJ}} \frac{\partial L^{IJ}}{\partial l^{IJ}}\right) \mathbf{e}^{IJ}.$$

The factor $\frac{\partial L}{\partial l}$ is zero when the resting length is constant, but for the rheological law presented in Chapter 3 , this factor is given in equations (3.11) and (3.17). In the subsequent expressions we will need the derivatives of the traction vectors above. We define matrix

$$\mathbf{K}_t^{ii} := \frac{\partial \boldsymbol{t}_D^{ij}}{\partial \boldsymbol{x}^i} = -\frac{\partial \boldsymbol{t}_D^{ji}}{\partial \boldsymbol{x}^i} = -\mathbf{K}_t^{ji} = -\mathbf{K}_t^{ij} = \mathbf{K}_t^{jj}, \tag{E.5a}$$

which after making use of equation (3.12), it can be deduced that,

$$\begin{aligned}
\mathbf{K}_t^{ij} &= (-1)^{\delta_{ij}+1}\left(\left(a^{ij}a^{ij} - \frac{\varepsilon^{ij}}{l^{ij}}a^{ij} + \varepsilon^{ij}b^{ij}\right)\mathbf{e}^{ij}\otimes\mathbf{e}^{ij} + \frac{\varepsilon^{ij}a^{ij}}{l^{ij}}\mathbf{I}\right)\\
a^{ij} &= \frac{1}{L^{ij}}\left(1 - \frac{l^{ij}}{L^{ij}}\frac{\partial L}{\partial l}\right)\\
b^{ij} &= \frac{1}{L^{ij}}\frac{\partial L}{\partial l}\left(-a^{ij} + \frac{1}{L^{ij}}\left(\frac{l^{ij}}{{L^{ij}}^2} - 1\right)\right).
\end{aligned} \tag{E.5b}$$

A similar derivation is obtained for $\frac{\partial \boldsymbol{t}_V^{IJ}}{\partial \boldsymbol{y}^I}$, but replacing ij by IJ. In this case, we also note that from the interpolation in (2.16) we have,

$$\begin{aligned}
\frac{\partial \boldsymbol{t}_V^{IJ}}{\partial \boldsymbol{x}^j} &= \mathbf{K}_t^{IJ}\left(\frac{\partial \boldsymbol{y}^J}{\partial \boldsymbol{x}^j} - \frac{\partial \boldsymbol{y}^I}{\partial \boldsymbol{x}^j}\right) = \mathbf{K}_t^{IJ}\left(p^j(\boldsymbol{\xi}^J) - p^j(\boldsymbol{\xi}^I)\right)\\
\frac{\partial \boldsymbol{t}_V^{IJ}}{\partial \boldsymbol{\xi}^J} &= \frac{\partial \boldsymbol{t}_V^{IJ}}{\partial \boldsymbol{y}^I}\frac{\partial \boldsymbol{y}^I}{\partial \boldsymbol{\xi}^J} + \frac{\partial \boldsymbol{t}_V^{IJ}}{\partial \boldsymbol{y}^J}\frac{\partial \boldsymbol{y}^J}{\partial \boldsymbol{\xi}^J} = \mathbf{K}_t^{IJ}\sum_{\boldsymbol{x}^j\in\mathcal{T}^J}\boldsymbol{x}^j\otimes\nabla p^j(\boldsymbol{\xi}^J),
\end{aligned}$$

where $p^i(\boldsymbol{\xi}^I) = 0$ if $i \notin \mathcal{T}^I$.

E.3 Linearisation terms in $\mathbf{K}_{xx}^{ij}$

By using the expressions of $\boldsymbol{g}_D^i$, $\boldsymbol{g}_V^i$ and $\boldsymbol{g}_A^i$ in (2.2), (2.21) and (2.30), and the definition of $\mathbf{K}_t^{ij}$ in (E.5), it can be deduced that

$$\begin{aligned}
\frac{\partial \boldsymbol{g}_D^i}{\partial \boldsymbol{x}^j} &= \sum_{j\in S^i}\mathbf{K}_t^{ij}\\
\frac{\partial \boldsymbol{g}_V^i}{\partial \boldsymbol{x}^j} &= \sum_{I\in B^i}\sum_{J\in S^I}\mathbf{K}_t^{IJ}\left(p^j(\boldsymbol{\xi}^J) - p^j(\boldsymbol{\xi}^I)\right)\\
\frac{\partial \boldsymbol{g}_A^i}{\partial \boldsymbol{x}^j} &= \frac{\lambda_A}{2}\mathbf{J}\sum_{m\in\bar{S}^i}(A^m - A_0^m)\sum_{IJ\in P^m}\left(p^i(\boldsymbol{\xi}^I)p^j(\boldsymbol{\xi}^J) - p^i(\boldsymbol{\xi}^J)p^j(\boldsymbol{\xi}^I)\right)\\
&\quad + \frac{\lambda_A}{4}\sum_{m\in\bar{S}^i}\sum_{IJ\in P^m}\mathbf{J}\left(p^i(\boldsymbol{\xi}^I)\boldsymbol{y}^J - p^i(\boldsymbol{\xi}^J)\boldsymbol{y}^I\right)\otimes\sum_{KL\in P^m}\mathbf{J}\left(p^j(\boldsymbol{\xi}^K)\boldsymbol{y}^L - p^j(\boldsymbol{\xi}^L)\boldsymbol{y}^K\right).
\end{aligned}$$

E.4 Linearisation terms in $\mathbf{K}_{xy}^{iJ}$

From the expressions of $\boldsymbol{g}_V^i$ and $\boldsymbol{g}_A^i$ in (2.21) and (2.30), and from equation (2.36), it can be also deduced that,

$$\frac{\partial \boldsymbol{g}_V^i}{\partial \boldsymbol{\xi}^J} = \left(\sum_{K \in S^J} \boldsymbol{t}_V^{JK} \right) \otimes \nabla p^i(\boldsymbol{\xi}^J) + \sum_{I \in B^i} p^i(\boldsymbol{\xi}^I) \sum_{J \in S^I} \mathbf{K}_t^{IJ} \frac{\partial \boldsymbol{y}^J}{\partial \boldsymbol{\xi}^J}$$

$$\frac{\partial \boldsymbol{g}_A^i}{\partial \boldsymbol{\xi}^J} = \frac{\lambda_A}{2} \mathbf{J} \sum_{m \in \bar{S}^i} (A^m - A_0^m) \sum_{IJ \in P^m}^{N_m} \left(p^i(\boldsymbol{\xi}^I) \frac{\partial \boldsymbol{y}^J}{\partial \boldsymbol{\xi}^J} - \boldsymbol{y}^I \otimes \nabla p^i(\boldsymbol{\xi}^J) \right)$$
$$+ \frac{\lambda_A}{2} \mathbf{J} \sum_{m \in \bar{S}^i} \sum_{IJ \in P^m}^{N_m} \left(p^i(\boldsymbol{\xi}^I) \boldsymbol{y}^J - p^i(\boldsymbol{\xi}^J) \boldsymbol{y}^I \right) \otimes \frac{\partial A^m}{\partial \boldsymbol{\xi}^J},$$

with $\frac{\partial A^m}{\partial \boldsymbol{\xi}^J}$ given in (2.38).

E.5 Linearisation terms in $\mathbf{K}_{yy}^{IJ}$

The linearisation of $\boldsymbol{g}_V^I$, $\boldsymbol{g}_A^I$ and $\boldsymbol{g}_\xi^I$ in (2.37) yields,

$$\frac{\partial \boldsymbol{g}_V^I}{\partial \boldsymbol{\xi}^J} = \sum_{K \in S^I} \sum_{i \in \mathcal{T}^I} \left(\nabla p^i(\boldsymbol{\xi}^I) \otimes \boldsymbol{x}^i \right) \left(\mathbf{K}_t^{II} \delta_{IJ} \frac{\partial \boldsymbol{y}^I}{\partial \boldsymbol{\xi}^J} + \mathbf{K}_t^{IK} \delta_{KJ} \frac{\partial \boldsymbol{y}^K}{\partial \boldsymbol{\xi}^J} \right)$$

$$\frac{\partial \boldsymbol{g}_A^I}{\partial \boldsymbol{\xi}^J} = \lambda_A \sum_{m=1}^{\bar{N}_{nodes}} \frac{\partial A^m}{\partial \boldsymbol{\xi}^I} \otimes \frac{\partial A^m}{\partial \boldsymbol{\xi}^J} + \lambda_A \sum_{m=1}^{\bar{N}_{nodes}} (A^m - A_0^m) \frac{\partial^2 A^m}{\partial \boldsymbol{\xi}^I \partial \boldsymbol{\xi}^J}$$

$$\frac{\partial \boldsymbol{g}_\xi^I}{\partial \boldsymbol{\xi}^J} = \lambda_\xi \delta_{IJ} \mathbf{I},$$

where the expressions of $\frac{\partial \boldsymbol{y}^I}{\partial \boldsymbol{\xi}^I}$ and $\frac{\partial A^m}{\partial \boldsymbol{\xi}^I}$ are given in (2.36) and in (2.38), respectively, and

$$\frac{\partial^2 A^m}{\partial \boldsymbol{\xi}^I \partial \boldsymbol{\xi}^J} = \sum_{KL \in P^m} \left(\delta_{KI} \delta_{LJ} \left(\frac{\partial \boldsymbol{y}^K}{\partial \boldsymbol{\xi}^I} \right)^T \mathbf{J} \frac{\partial \boldsymbol{y}^L}{\partial \boldsymbol{\xi}^J} - \delta_{LI} \delta_{KJ} \left(\frac{\partial \boldsymbol{y}^L}{\partial \boldsymbol{\xi}^I} \right)^T \mathbf{J} \frac{\partial \boldsymbol{y}^K}{\partial \boldsymbol{\xi}^J} \right).$$

Bibliography

Alt S, Ganguly P, and Salbreux G. Vertex models: from cell mechanics to tissue morphogenesis. *Philos. Trans. R. Soc. London B. Biol. Sci.*, 372(1720), 2017. http://dx.doi.org/10.1098/rstb.2015.0520.

Antunes M, Pereira T, Cordeiro JV, Almeida L, and Jacinto A. Coordinated waves of actomyosin flow and apical cell constriction immediately after wounding. *J. Cell Biol.*, 202(2):365–379, 2013.

Arroyo M and DeSimone A. Shape control of active surfaces inspired by the movement of euglenids. *J. Mech. Phys. Solids*, 62:99–12, 2014.

Asadipour N, Trepat X, and Muñoz JJ. Porous-based rheological model for tissue fluidisation. *J. Mech. Phys. Solids*, 96:535–549, 2016.

Babuška I and Aziz A. On the angle condition in the finite element method. *SIAM J. Numer. Analysis*, 13:214–227, 1976.

Barber C, Dobkin D, and Huhdanpaa HT. The quickhull algorithm for convex hulls. *ACM Trans. Math. Softw.*, 22(4):469–483, 1996. http://www.qhull.org

Beret C, Sulak L, and Lecuit T. Myosin-dependent junction remodelling controls planar cell intercalation and axis elongation. *Lett. Nat.*, 429:667–671, 2004.

Bergdorf M, Milde F, and Koumoutsakos P. *Multiscale Cancer Modeling*, Chapter 11, pages 213–237. Chapman and Hall/CRC mathematical and Computational Biology, 2010.

Besser A, Colombelli J, Stelzer EHK, and Schwarz US. Viscoelastic response of contractile filament bundles. *Phys. Rev. E*, 83(051902), 2011.

Bi D, Yang X, Marchetti MC, and Manning ML. Motility-Driven Glass and Jamming Transitions in Biological Tissues. *Phys. Rev. X.*, 6:021011, 2016.

Bittig T, Wartlick O, Kicheva A, González-Gaitán M, and Jülicher F. Dynamics of anisotropic tissue growth. *New J. Phys.*, 10(063001), 2008.

Brodland GW. Computational modeling of cell sorting, tissue engulfment, and related phenomena: a review. *Appl. Mech. Rev.*, 57:1–30, 2004.

Brugués A, Anon E, Conte V, Veldhuis J, Gupta M, Collombelli J, Moñuz JJ, Brodland GW, Landoux B, and Trepat X. Forces driving epithelial wound healing. *Nature Phys.*, 10:683–690, 2014.

Carreira-Perpiñán MÁ. A review of dimension reduction techniques. *Tech. Rep.*, CS-96-09, Department of Computer Science, University of Shefflield, UK, 1997.

Casey J. *A Sequel to the First Six Books of the Elements of Euclid, Containing an Easy Introduction to Modern Geometry with Numerous Examples.* Hodges, Figgis & Co., Dublin, 5th edition, 1988.

Chaudhuri O, Parekh S, and Fletcher D. Reversible stress softening of actin networks. *Nature*, 445:295–298, 2007.

Clément R, Collinet C, Dehapiot B, Lecuit T, and Lenne PF. Viscoelastic dissipation stabilizes cell shape changes during tissue morphogenesis. *BioRxiv.*, 2017. doi.org/10.1101/107557

Costa M, Sweeton D, and Wieschaus E. *The development of* Drosophila melanogaster. Chapter 8: Gastrulation in *Drosophila*: cellular mechanisms of morphogenetic movements. Cold Spring Laboratory Press, New York, 1993.

Cueto E, Calvo B, and Doblaré M. Modelling three-dimensional piece-wise homogeneous domains using the α-shape-based natural element method. *Int. J. Num. Meth. Engng.*, 54(6):871–897,2002. doi:10.1002/nme.452.

Davidson LA, Joshi SD, Kim HY, von Dassow M, Zhang L, and Zhou J. Emergent morphogenesis: Elastic mechanics of a self-deforming tissue. *J. Biomech.*, 43:63–70, 2010.

Doubrovinski K, Swan M, Polyakov O, and Wieschaus E. Measurement of cortical elasticity in *Drosophila melanogaster* embryos using ferrofluids. *Proc. Nat. Acad. Sci. USA*, 114 (5):1051–1056, 2017.

Edelsbrunner H and Mücke EP. Three-dimensional alpha shapes. *ACM Trans. Graph.*, 13(1):43–72, 1994.

Fernández-Sánchez M, Barbier S, Whitehead J, Bealle G, Michel A, Latorre-Ossa H, Rey C, Fouassier L, Claperon A, Brulle L, Girard E, Servant N, Rio-Frio T, Marie H, Lesieur S, Housset C, Gennisson J, Tanter M, Menager C, Fre S, Robine S, and Farge E. Mechanical induction of the tumorigenic β-catenin pathway by tumour growth pressure. *Nature*, 523(7558):92–95, 2015.

Findley WN, Lai JS, and Onaran K. *Creep and Relaxation of Nonlinear Viscoelastic Materials: With an Introduction to Linear Viscoelasticity.* Dover,New York, 1989.

Fletcher AG, Mirams GR, Murray PJ, Walter A, Kang JW, Cho KH, Maini PK, and Byrne HM. *Multiscale Cancer Modeling*, Chapter 6, pages 111–134. Chapman and Hall/CRC Mathematical and Computational Biology, 2010.

Fletcher AG, Osborne J, Maini P, and Gavaghan D. Implementing vertex dynamics models of cell polulations in biology within a consistent computational framework. *Prog. Byoph. Mol. Biol.*, 113(2):299–326, 2013. doi:http://dx.doi.org/10.1016/j.pbiomolbio.2013.09.003.

Forgacs G, Foty RA, Shafrir Y, and Steinberg MS. Viscoelastic properties of living embryonic tissues: a quantitative study. *Bioph. J.*, 74(2227), 1998.

Frieboes H, Lowengrub J, Wise S, Zheng X, Macklin P, Bearer E, and Cristini V. Computer simulation of glioma growth and morphology. *Neuroimage*, 37:59–70, 2007.

Fu L, Hu XY, and Adams NA. A physics-motivated centroidal Voronoi particle domain decomposition method. *J. Comp. Phys.*, 335:718–735 , 2017.

Fung YC. *Biomechanics: Mechanical Properties of Living Tissues.* Springer, New York, 2nd edition, 1993.

Galle J, Loeffler M, and Drasdo D. Modeling the effect of deregulated proliferation and apoptosis on the growth dynamics of epithelial cell populations in vitro. *Bioph. J.*, 88:62–75, 2005.

Gatsonis A and Spirkin A. A three-dimensional electrostatic particle-in cell methodology on unstructured Delaunay-Voronoi grids. *J. Comp. Phys.*, 228(10):3742–3761, 2009.

Ghosh S and Moorthy S. Three-dimensional Voronoi cell finite element model for microstructures with ellipsoidal heterogeneities. *Comput. Mech.*, 10(34):510–531, 2004.

Gittes F and MacKintosh FC. Dynamic shear modulus of a semiflexible polymer network. *Phys. Rev. E*, 58(R1241),1998.

González D, Cueto E, Chinesta F, and Doblaré M. A natural element updated lagrangian strategy for free-surface fluid dynamics. *J. Comp. Phys.*, 223(1):127–150, 2007.

González-Valverde I and García-Aznar JM. A hybrid computational model to explore the topological characteristics of epithelial tissues. *Int. J. Num. Meth. Biomed. Engng.*, 2017. doi: 10.1002/cnm.2877.

Gregor T, Bialek W, de Ruyter van Steveninck RR, Tank DW, and Wieschaus EF. Diffusion and scaling during early embryonic pattern formation. *Proc. Nat. Acad. Sci. USA*, 102(18403), 2005.

Guittet A, Lepilliez M, Tanguy S, and Gibou F. Solving elliptic problems with discontinuities on irregular domains - the Voronoi Interface Method. *J. Comp. Phys.*, 298:747–765, 2015.

Hardin J and Keller R. The behaviour and function of bottle cells during gastrulation of *Xenopus laevis*. *Development*, 103: 211–230, 1988.

Hardin J and Walston T. Models of morphogenesis: the mechanisms and mechanics of cell rearrangement. *Curr. Opin. Genet. & Dev.*, 14 (4):399–406, 2004.

Harris AR, Bellis J, Khalilgharibi N, Wyatt T, Baum B, Kabla AJ, and Charras GT. Generating suspended cell monolayers for mechanobiological studies. *Nat. Protoc.*, 8 (12):2516–2530, 2013.

Harris AR, Peter L, Bellis J, Baum B, Kabla AJ, and Charras GT. Characterizing the mechnics of cultured cell monolayers. *Proc. Nat. Acad. Sci. USA*, 109 (41):16, 449–16, 454, 2012.

Holpzafel GA. *Nonlinear Solid Mechanics: A continuum Approach for Engineering.* John Wiley and & Sons, Chichester, 5th edition, 2007.

Honda H, Motosugi N, Nagai T, Tanemura M, and Hiiragi T. Computer simulation of emerging asymmetry in the mouse blastocyte. *Development*, 135(8):1407–1414, 2008.

Honda H, Ogita Y, Higuchi S, and Kani K. Cell movements in a living mammalian tissue: long-term observation of individual cells in wounded corneal endothelia of cats. *J. Morphol.*, 174, 25–39, 1982.

Honda H, Tanemura M, and Nagai T. Geometrical models for cells in tissues. *Int. Rev. Cytol.*, 1983(81):191–248, 1983.

Honda H, Tanemura M, and Nagai T. A three-dimensional vertex dynamics cell model of space-filling polyhedra simulating cell behaviour in a cell aggregate. *J. Theor. Biol.*, 226:439–453, 2004.

Jacobs CR, Huang H, and Kwon RY. *Introduction to cell mechanics and mechanobiology*, chapter 1, pages 1–15. Garland Science, 1st edition, 2012.

Janmey PS, Hivdt S, Käs J, Lerche D, Maggs A, Sackmann E, Schliwa M, and Stossel TP. Softness, strength and self-repair in intermediate filament networks. *J. Biol. Chem.*, 269(32503), 1994.

Keller R, Davidson LA, and Shook DR. How we are shaped: The biomechanics of gastrulation. *Differentiation*, 71: 171–205, 2003.

Khalilgharibi N, Fouchard J, Asadipour N, Yonis A, Harris A, Mosaffa P, Fujita Y, Kabla A, Baum B, Muñoz JJ and Charras GT. Stress relaxation in epithelial monolayers arises from length change controlled by actomyosin. Manuscript submitted for publication.

Krul T, Kaandorp J, and Blom JG. Modeling developmental regulatory networks. *Lect. Notes. Comput. Sc.*, 2660:688–697, 2003.

Lambert T. The Delaunay triangulation maximizes the mean inradius. *Proceedings of the 6th Canadian Conference on Computational Geometry (CCCG94)*, 201–206, 1994.

Lecuit T and Lenne PF. Cell surface mechanics and the control of cell shape, tissue patterns and morphogenesis. *Nat. Rev.*, 8:633–644, 2007.

Lee JA and Verleysen M. *Nonlinear Dimensionality Reduction.* Information science and statistics, Springer, New York, 2007.

Leptin M and Grunewald B. Cell shape changes during gastrulation in *Drosophila*. *Development*, 110:72–84, 1990.

Lewis H. Mechanics of invagination. *Anat. Rec.*, 97: 139–156, 1947.

Lin IE and Taber LA. Mechanical effects of looping in the embryonic chick heart morphogenesis. *J. Biomech.*, 27:311–321, 1994.

Ma X, Lynch HE, Skully PC, and Hutson MS. Probing embryonic tissue mechanics with laser hole drilling. *Phys. Biol.*, 6(3):036004, 2009.

der Maaten LJPV, Postma EO, and den Herik HJV. Dimensionality Reduction: A comprehensive review. *TiCC TR*, 2009–5, Tilburg University, The Netherlands, 2009.

MacKintosh FC, Käs J, and Janmey PA. Elasticity of semiflexible biopolymer networks. *Phys. Rev. Letters*, 75(4425), 1995.

MacKintosh FC and Levine AJ. Nonequilibrium mechanics and dynamics of motor-activated gels. *Phys. Rev. Letters*, 100(018104), 2008.

Macklin P, Edgerton ME, Lowengrub JS, and Cristini V. *Multiscale Modelling of Cancer*, Chapter 6, pages 88–122. Cambridge University Press, Cambridge, UK, 2010.

Macklin P and Lowengrub JS. Nonlinear simulation of the effect of microenvironment on tumor growth. *J. Theor. Biol.*, 245:677–704, 2007.

Millán D, Rosolen A, and Arroyo M. Non-linear manifold learning for mesh-free finite deformations thin shell analysis. *Int. J. Num. Methods Eng.*, 93 (7): 685–713, 2013.

Mizuno D, Tardin C, Schmidt CF, and MacKintosh FC. Nonequilibrium mechanics of active cytoskeletal networks. *Science*, 315(5810):370–373, 2007.

Moeendarbary E, Valon L, Fritzsche M, Harris A, Moulding D, Thrasher A, Stride E, Mahadevan L, and Charras GT. The Cytoplasm of living cells behaves as a poroelastic material. *Numer. Math.*, 12:253–261, 2013.

Moorthy S and Ghosh S. A model for analysis of arbitrary composite and porous microstructures with Voronoi cell finite elements. *Int. J. Num. Meth. Engng.*, 39(14):2363–2398, 1996.

Morozof KI and Pismen LM. Motor-driven effective temperature and viscoelastic response of active matter. *Phys. Rev. E*, 81(061922),2010.

Mosaffa P, Asadipour N, Millán D, Rodríguez-Ferran A, and Muñoz JJ. Cell-centred model for the simulation of curved cellular monolayers. *Comp. Part. Mech.*, 2(4):359–370, 2015.

Mosaffa P, Rodríguez-Ferran A, and Muñoz JJ. Hybrid cell-centred/vertex model for multicellular systems with equilibrium-preserving remodelling. *Int. J. Num. Meth. Biomed. Engng.*, 2017 (in press).

Munjal A, Philippe J, Munro E, and Lecuit T. A self-organised biomechanical network drives shape changes during tissue morphogenesis. *Nature*, 524(7565):351–355, letter, 2015.

Muñoz JJ and Albo S. Physiology-based model of cell viscoelasticity. *Phys. Rev. E*, 88(012708), 2013.

Muñoz JJ, Barrett K, and Miodownik M. A deformation gradient decomposition method for the analysis of the mechanics of morphogenesis. *J. Biomech.*, 40:1372–1380, 2007.

Muñoz JJ, Conte V, Asadipour N, and Miodownik M. A truss element for modelling reversible softening in living tissues. *Mech. Res. Commun.*, 49:44–49, 2013.

Neumann JV and Burks AW. *Theory of Self-Reproducing Automata.* University of Illinois Press, 1966.

Odell GM, Oster G, Alberch P, and Burnside B. The mechanical basis of morphogenesis: I. Epithelial folding and invagination. *Dev. Biology*, 84:446–462, 1981.

Okabe A, Boots B, and Sugihara K. *Spatial Tessellations: Concepts and Applications of Voronoi Diagrams.* Wiley, New York, 1992.

Okuda S, Inoue Y, Eiraku M, Adachi T, and Sasai Y. Vertex dynamics simulations of viscosity-dependent deformation during tissue morphogenesis. *Biomech. Model. Mechanobiol.*,14(2):413–425, 2015.

Okuda S, Inoue Y, Eiraku M, Sasai Y, and Adachi T. Modeling cell proliferation for simulating three-dimensional tissue morphogenesis based on a reversible network reconnection framework. *Biomech. Model. Mechanobiol.*, 12:987–996, 2013.

Osborne JM, Walter A, Kershaw SK, Mirams GR, Fletcher AG, Pathmanathan P, Gavaghan D, Jensen OE, Maini PK, and Byrne HM. A hybrid approach to multiscale modeling of cancer. *Phil. Trans. Royal Soc. London A*, 368:5013–5028, 2010.

Pare AC, Vichas A, Fincher CT, Mirman Z, Farell DL, Mainieri A, and Zallen JA. A positional toll receptor code directs convergent extension in *Drosophila* Egg. *Nature*, 515:526–527, 2014.

Perrone M, Veldhuis J, and Brodland G. Dynamic analysis of spatial flexible multibody systems using joint co-ordinates, *Biomech. Model. Mechanobiol.*, 15(2):405–418, 2016.

Pitt-Francis J, Pathmanathan P, Bernabeu MO, Bordas R, Cooper J, Fletcher AG, Mirams GR, Murray P, Osborne JM, Walter A, Chapman SJ, Garny A, van Leeuwen IMM, Maini PK, Rodríguez B, Waters SL, Whiteley JP, Byrne HM, and Gavaghan DJ. Chaste: A test-driven approach to software development for biological modelling. *Comput. Phys. Commun.*, 180:2452–2471, 2009.

Ramis-Conde I, Drasdo D, Anderson ARA, and Chaplain MAJ. Modelling the influence of the E-cadherin-β-catenin pathway in cancer cell invasion: a multiscale approach. *Bioph. J.*, 95:155–165, 2008.

Razzell W, Wood W, and Martin P. Recapitulation of morphogenetic cell shape changes enables wound re-epithelialisation. *Development*, 141(1814–1820), 2014.

Rejniak K. An immersed boundary framework for modelling the growth of individual cells: An application to early tumour development. *J. Theor. Biol.*, 247(1):186–204, 2007.

Rodriguez EK, Hoger A, and McCulloch AD. Stress-dependent finite growth in soft elastic tissues. *J. Biomech.*, 27:455–467, 1994.

Roeland RMH and Glazier JA. A cell-centred approach to developmental biology. *Physica A*, 352:113–130, 2005.

Roweis ST and Saul LK. Think Globally, Fit Locally: Unsupervised learning of low-dimensional manifolds. *J. Mach. Learn. Res.*, 4:119–155, 2003.

Roweis ST and Saul LK. Nonlinear dimensionality reduction by locally linear embedding. *Science*, 290: 2323–2326, 2000.

Salbreux G, Charras GT, and Paluch E. Actin cortex mechanics and cellular morphogenesis. *Trends Cell Biol.*, 22 (10): 536–545, 2012.

Sandersius S and Newman T. Modelling cell rheology with the Subcellular Element Model. *Phys. Biol.*, 5(1)045008, 2008.

Sandersius S, Weijer C, and Newman T. Emergent cell and tissue dynamics for subcellular modelling of active biomechanical processes. *Phys. Biol.*, 8 (045007), 2011.

Schaller G and Meyer-Hermann M. Multicellular tumor spheroid in an off-lattice Voronoi-Delaunay cell model. *Phys. Rev. E*, 71(51910), 2005.

Sibson R. A vector Identity for the Dirichlet tessellation. *Math. Proc. Cambr. Phil. Soc.*, 87(1):151–155, 1980. doi:10.1017/S0305004100056589.

Slepchenko BM, Shaff JC, Macara I, and Loew LM. Quantitative cell biology with the virtual cell model. *Trends Cell Biol.*, 13:570–576, 2003.

Spahn P and Reuter R. Avertex model of *Drosophila* ventral furrow formation. *PLOS ONE*, 8(9):e75051, 2013.

Sukumar N. Voronoi cell finite difference method for the diffusion operator on arbitrary unstructured grids. *Int. J. Num. Meth. Engng.*, 57(1):1–34, 2003.

Sunyer R, Conte V, Escribano J, Elosegui-Artola A, Labernadie A, Valon L, Navajas D, García-Aznar JM, Muñoz JJ, Roca-Cusachs P, and Trepat X. Collective cell durotaxis emerges from long-range intercellular force transmission. *Science*, 353(6304):1157–1161, 2016. doi:10.1126/science.aaf7119.

Trepat X, Wasserman M, Angelini T, Millet E, Weitz D, Butler J, and Fredberg J. Physical forces during collective cell migration. *Nat. Phys.*, 5(3):426–430, 2009.

Tomita M, Hashimoto K, Takahashi K, Shimizu T, Matsuzaki Y, Miyoshi F, Saito K, Tanida S, Yugi K, Venter J, and Hatchison C. E-CELL: Software Environment for Whole-Cell Simulation. *Bioinformatics*, 15:72–84, 1999.

Walker DC, Southgate J, Hill G, Holcombe M, Hose DR, Wood SM, MacNail S, and Smallwood RH. The epitheliome: agent-based modelling of the social behaviour of cells. *Biosystems*, 76:89–100, 2004.

Wilson EL. *A computer program for the dynamic stress analysis of underground structures.* UCB/SESM Report No. 68/01, University of California, Berkley, 1968.

Zhang Z and Wang J. MLLE: Modified locally linear embedding using multiple weights. In: Schölkopf B, Platt J and Hoffman T (eds). *Advances in Neural Information Processing Systems.* 19, MIT Press, Cambridge, 1593–1600, 2007.